SUBCRITICAL TRANSITION IN SHEAR FLOWS

Dissertation submitted for the Degree of

Doctor of Philosophy

DEPARTAMENT DE FÍSICA APLICADA

UNIVERSITAT POLITÈCNICA DE CATALUNYA

by

Fernando Mellibovsky

June 2008

SUBCRITICAL TRANSITION IN SHEAR FLOWS

Fernando Mellibovsky, Ph.D.
Universitat Politècnica de Catalunya 2008

Understanding transition to turbulence in shear flows, even for rather simple fluid systems, is a major challenge that has attracted the attention of the scientific community for over a century. Its technological implications are far-reaching, very especially in the case of aeronautics, for which shear flows are of outstanding importance. The focus has been set here on subcritical transition of wall-bounded shear flows and, in particular, of pipe flow (pressure-driven flow along a circular pipe).

This work has aimed at providing a deeper understanding of the mechanisms that are responsible for transition bypassing linear instability of the pipe basic flow. To this end, two complementary research approaches have been undertaken.

The first approach has consisted in a direct characterisation of the basin of attraction of the stable basic flow. The critical threshold beyond which finite amplitude perturbations are capable of bringing about transition has been investigated and scaling laws describing how the basin of attraction of the laminar profile shrinks with increasing flow speed have been provided for different types of perturbations. Very good agreement with recent accurate pipe flow experiments has been obtained.

However, simple characterisation of the critical threshold does not provide, on its own, much insight on what the mechanisms behind transition are. A second approach, consisting in a direct exploration of the phase map from a dynamical systems point of view, has acquired great momentum in the very recent past. As a result, new states disconnected from the basic flow have been identified. These solutions, which take the form of periodic travelling waves in pipe flow, have been computed and their implications in transition and in developed turbulence assessed. Some of them arise from a purely theoretical course of action. Their relevance in developed turbulence has been positively established both experimentally and numerically in the literature, but their alleged role in transition has not been clarified. In the present work, new solutions have been found within a chaotic state that resides within the critical threshold and seems to govern transition. Because they naturally dwell in this chaotic saddle, their relevance to transition seems to be beyond any doubt.

The chaotic state and the solutions found, however, correspond to short pipe global transition, where no intermittency phenomena is ever observed. Transition to localised structures typical of long pipes, such as puffs or slugs, seems instead to be governed by a localised chaotic state of about the same characteristic length of the turbulent structures the basin of attraction of which it bounds. No simple travelling-wave-type solutions have been identified within the chaotic localised state. The relationship between the short wavelength periodic states and experimental transition to localised long structures remains an open problem that should be the object of future work.

To my family, to my girlfriend, to dorita.

ACKNOWLEDGEMENTS

I would like to thank my advisers, Álvaro Meseguer and Francisco Marqués, for their priceless help and advice in the course of this thesis over the past four years.

Financial support from the Universitat Politècnica de Catalunya through a *UPC-recerca* grant is fully acknowledged. In this respect I am sincerely and deeply obliged to Pr. Juan Jesús Pérez.

I would also like to take the opportunity to thank the whole bunch of the Applied Physics department staff for their invaluable support.

I should also thank Pr. Bruno Eckhardt and Dr. Tobias Schneider for very enlightening and inspiring discussions on the pipe problem as well as for their hospitality upon my visit to Marburg. Also Dr. Yohann Duguet deserves my most deep gratefulness for the long and stimulating chats during his visit to Barcelona.

Finally, I would also like to thank Dr. José Leal, without whom I would most certainly have gone nuts ;-).

TABLE OF CONTENTS

LIST OF TABLES

LIST OF FIGURES

CHAPTER 1

INTRODUCTION

1.1 Relevance of transition in Aerospace Science

Understanding transition to turbulence in shear flows, even for rather simple fluid systems, is a major challenge that has attracted the attention of the scientific community for over a century. Its technological implications are far-reaching, very specially in the case of aeronautics, for which shear flows are of outstanding importance. Computational fluid mechanics, dynamical systems analysis and bifurcation theory are combined together in the present work to try and shed some light on the unsolved problem of subcritical transition in wall-bounded shear flows.

Most technological problems involving fluids in motion have, at some point, to deal with turbulence. In some applications, such as those requiring mixing, turbulence is a very useful phenomenon, but, more often than not, it is a nuisance. A clear example of this would be the boundary layer developing on an aircraft wing. Because of the mixing, a turbulent boundary layer induces greater friction on the walls on which it develops than a laminar boundary layer would, thus resulting in higher aircraft drag. For this reason alone, many efforts are devoted to maintaining the boundary layer laminar for as long a distance on the wing chord as possible, trying to push transition further and further downstream. Could the boundary layer be kept laminar over the full chord of wings, tail and nacelles of an Airbus-type aircraft, drag would be reduced by up to a 10-15%, with the ensuing benefit in terms of fuel consumption and a huge impact on direct operating costs. Also the flow through a pipe, present in many technical applications not limited to the aeronautical domain, can be driven with much lower energy consumption if it is forced to remain laminar.

Many technical solutions have been investigated in order to maintain laminarity (Fig. 1.1). Here we will focus on the more theoretical approach of trying to comprehend the intimate mechanisms of transition as a first step towards gaining full control of laminarity.

A variety of flows exists exhibiting instabilities that eventually lead to turbulence. The focus will be set here on shear instabilities appearing in wall-bounded shear flows. Shear flows are those for which the velocity gradients have a strong component in a direction normal (or quasi normal) to the main orientation of the flow. Some examples are pipe and channel flows, boundary layers, jets and wakes. These flows often experience transition to turbulence for values of the *Reynolds number* (Re) well below that for which they become

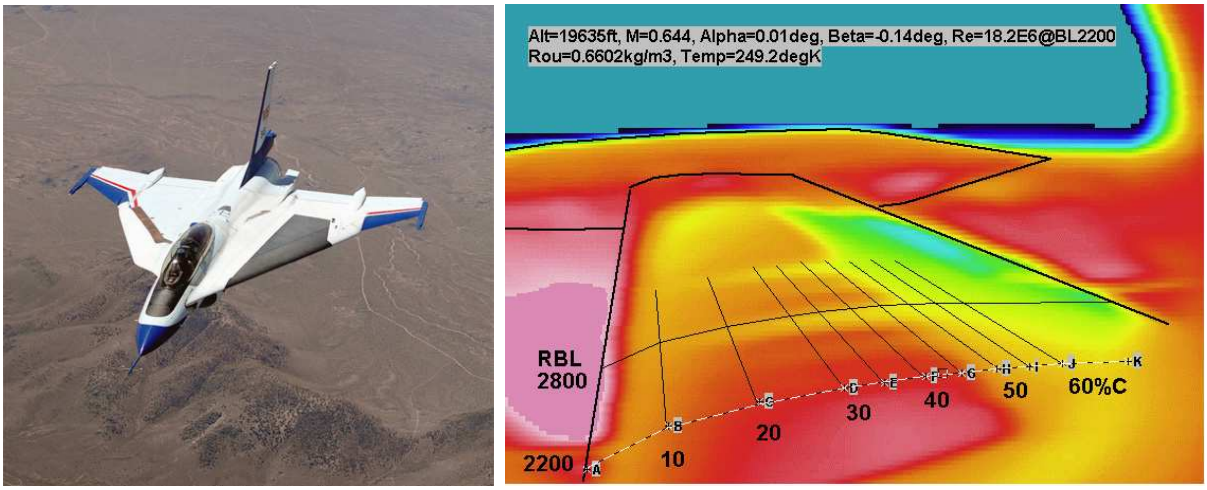

Figure 1.1: On the left, NASA test on laminar flow control at supersonic speeds. On the right, CFD analysis of the honda-jet laminar wing.

linearly unstable, some of them being even believed to remain linearly stable for all values of Re. This transition not stemming from linear instability is usually called *bypass* (or *subcritical*) transition.

Many factors of all sorts influence transition. Compressibility, wall rugosity, heat transfer or preturbulence levels are some examples of accessory parameters, certainly having an impact on transition, but playing a nonessential role. To explore the underlying physical mechanisms, it is therefore crucial to get rid of all these secondary factors and aim at a minimal description carrying the essential elements involved. Thus, we are left with the bare incompressible Navier-Stokes equations governing fluid flow, which are alone capable of describing transition. The simplest geometry exemplifying the transition scenario investigated (i.e. subcritical shear instability) has been presently chosen to exclude as far as possible problem-dependent effects on transition. With such premises, the analysis of transition in a pressure-driven flow along a circular infinite pipe is undertaken, since we consider it to be the simplest problem containing all the ingredients that are needed for subcritical transition in wall-bounded flows, which is a chief interest of the aeronautical community.

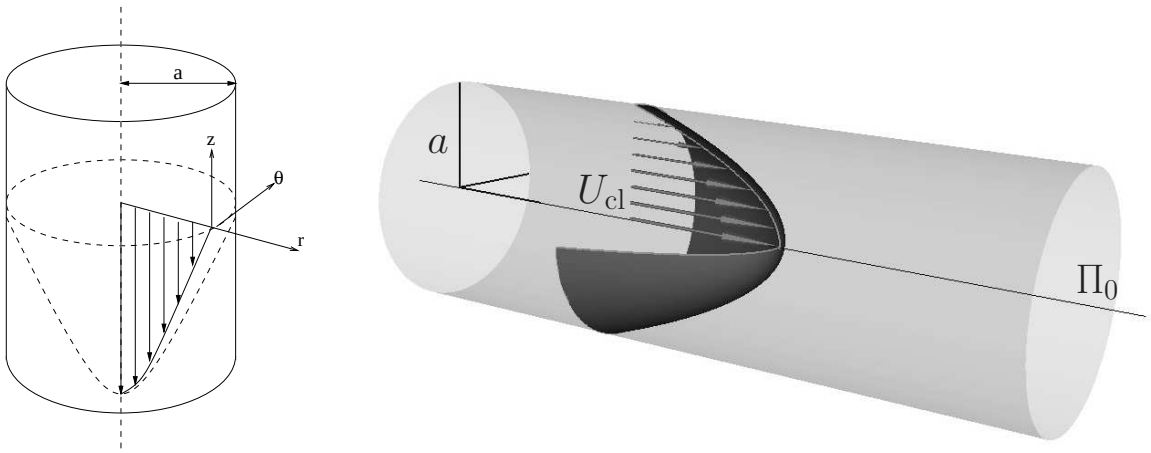

Figure 1.2: Sketch of the Pipe Poiseuille parabolic basic solution.

1.2 The pipe problem

In pipe or *Hagen-Poiseuille* flow, a fluid of kinematic viscosity ν is axially driven through a circular pipe of radius a by means of a uniform axial pressure gradient. The basic solution of the Navier-Stokes equations is a parabolic, streamwise-independent, axisymmetric and steady purely axial flow (Fig. 1.2). The basic flow Reynolds number is defined as $Re = U_{\rm CL}a/\nu$, where $U_{\rm CL}$ is the maximum axial speed of the flow at the centre-line of the pipe. A more common definition of the Reynolds number in pipe flow, which we will call *a*ctual Reynolds number, is $Re_a = \bar{U}D/\nu$, where $\bar{U} = Q/\pi a^2$ is the mean axial velocity (Q being the massflux) and $D = 2a$ is the pipe diameter.

The parabolic basic solution is believed to be linearly stable for all values of the governing parameter Re, as seem to indicate both experimental [54] and numerical studies [14, 35, 62, 56, 45]. Notwithstanding its linear stability, beyond a certain critical value of $Re \simeq 2000$ pipe flow undergoes transition to turbulence in the presence of large enough finite amplitude perturbations [14]. The parabolic profile ceases to be a global attractor and its basin of attraction is no longer the full phase space. Furthermore, experimental evidence shows that pipe flow becomes more sensitive to perturbations when increasing the Reynolds number. Since the flow is linearly stable, finite (yet small) amplitude perturbations must be responsible for the transition to turbulence.

1.3 Subcritical transition in shear flows

Transition to turbulence in Hagen-Poiseuille flow has been object of analysis for over a century. Since the seminal work of Osborne Reynolds [58] published in 1883, many physicists and applied mathematicians have devoted enormous efforts to provide a theoretical explanation of the phenomenon of subcritical transition to turbulence in shear flows such as plane Couette or pipe flow.

Thus, many theoretical [3, 6, 19, 20], numerical [62, 81, 78, 38, 45, 40, 22] and experimental [80, 11, 13, 27] studies have tried to produce an explanation to pipe flow transition in the past three decades.

As we have already pointed out, transition to turbulence in shear flows still remains an open problem of hydrodynamic stability theory. For instance, plane Couette flow (fluid contained between inertially sliding infinite parallel plates) is always linearly stable, i.e., any infinitesimal perturbation of the flow decays for long times, yet it exhibits transition to turbulence in the laboratory and in numerical simulations for moderate flow speeds [59, 12, 65, 1]. Hagen-Poiseuille or pipe flow (pressure driven flow through an infinite circular pipe) is believed to be linearly stable as well but also becomes turbulent in practise [14, 45, 63, 11, 27]. Plane Couette and pipe flow, because of their apparent simplicity, are the most fundamental examples of *subcritical* transition to turbulence in fluid dynamics, i.e., transition to turbulence bypassing linear stability.

1.4 Research approaches to subcritical transition

Typical transition scenarios in shear flows are the secondary instability of *Tollmien-Schlichting waves*, the *streak breakdown* mechanism and *oblique* transition [63]; the former emanating from a local bifurcation, the other two correspond to bypass transition.

Streak breakdown has been proved a universal and very effective transition mechanism in shear flows. It relies on the nonmodal transient growth exhibited by streamwise vortical finite-amplitude disturbances. The perturbation develops into two-dimensional transient structures called *streaks* that modulate the basic flow so that it exhibits an inflectional velocity profile. The presence of saddle points inviscidly destabilises certain optimal three-dimensional infinitesimal perturbations that grow exponentially [81]. Whenever these waves attain sufficient energy before the onset of the streaks' viscous decay, nonlinear interaction triggers transition.

A first approach towards comprehending transition to turbulence aims at characterising the basin of attraction of the basic flow. Subcritical turbulence can be viewed as a flow state taking the form of a chaotic attractor coexisting with the laminar basic flow. This first step consists in measuring the *critical amplitude threshold*, $A_c(Re)$, of the basic regime (minimal amplitude of perturbations inducing turbulence), being plausible to assume that its asymptotic behaviour scales with Re according to

$$A_c \sim Re^{\gamma}, \tag{1.1}$$

with γ necessarily negative. Theoretical exponents for plane channel flows have been obtained by means of asymptotic methods within the framework of some particular transition scenarios [8], of which streak breakdown is among the most effective. Lab experiments do not have access to arbitrary initial disturbances, but some renormalisations [71] have recently been suggested in order to cast different pipe experimental results in terms of a single definition of the amplitude appearing in (1.1). The exponent for these experiments is found to lie within the interval $\gamma \in [-9/5, -6/5]$.

The most accurate experimental explorations, based on an injection system perturbing a constant massflow pipe [27], have concluded that $\gamma \sim 1$. Figure 1.3 shows a schematic representation of the experimental device used together with a picture of a transitional run.

A direct exploration of the phase map of the corresponding dynamical system representing the fluid problem constitutes another approach to unfold the nature of the chaotic attractor as a step towards comprehending transition. Numerical studies have recently revealed the existence of travelling wave solutions, presumably constituting a fundamental ingredient of the chaotic dynamics observed [19]. The limit cycles associated with these travelling waves have been proved to be linearly unstable and their associated friction factor

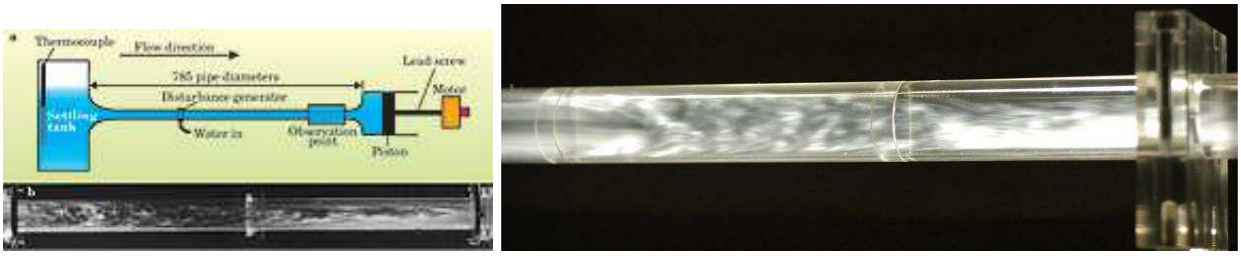

Figure 1.3: On the left, drawing of the Manchester experimental constant-massflow pipe. On the right, picture exhibiting a turbulent run. (Courtesy of J. Peixinho and T. Mullin)

agrees reasonably well with the empirical laws describing turbulent flows in smooth pipes, as a clear sign of the relevance of these solutions in the turbulent regime. Postprocessed experimental results have recently suggested the presence of the aforementioned travelling waves as inherent components of the turbulent flow [26]. Clearer traces of travelling wave transients, regarding the underlying dynamical mechanism and their wavelength, have since been identified in turbulence regeneration studies at moderate Re [25].

1.5 Outline

This work is structured as follows. The numerical scheme devised to solve the Navier-Stokes equations in a cylindrical domain is presented in chapter 1, together with a convergence analysis and some test examples. The contents of this chapter were published in Meseguer & Mellibovsky [42]. Chapters 3 and 4 are devoted to the characterisation of the basin of attraction of the basic flow through the critical exponent presented above as one of the current research approaches aiming at explaining transition. Chapter 3, published in Mellibovsky & Meseguer [38], concentrates on transition following global perturbations based on the streak breakdown mechanism. Transition due to localised impulsive perturbations like those inflicted in experiments are investigated in chapter 4, the contents of which appeared published in Mellibovsky & Meseguer [39]. The other research approach mentioned, based on direct exploration of phase space, is undertaken within chapters 5 and 6. A method to track unstable travelling wave solutions that seem to play a role in turbulence and transition is presented in chapter 5 together with the states found. An outline of the method to track travelling wave solutions has been published in Meseguer, Avila, Mellibovsky & Marques [41] in conjunction with the several research lines of the Barcelona fluid dynamics group to which I belong. In chapter 6, a method to compute trajectories in the critical boundary between laminarity and turbulence is implemented and the travelling wave search method is applied to identify solutions that are embedded in the chaotic attractor governing the critical dynamics. Finally, the main conclusions regarding pipe flow transition to turbulence are summarised in chapter 7.

CHAPTER 2
MATHEMATICAL FORMULATION & NUMERICAL APPROACH

Spectral methods have been extensively applied for the approximation of solutions of the Navier-Stokes equations [4, 7, 21]. So far, collocation or pseudospectral methods have been more popular than Galerkin spectral because they are easier to formulate and implement. One of the arguments that have been frequently given to encourage the use of Galerkin instead of collocation methods is that sometimes the former provide banded matrices in the spatial discretisation of linear operators, which improves the efficiency of the linear solvers in the time integrations. The difficulty of Galerkin methods lies on their mathematical formulation. In particular, the Navier-Stokes equations in non-cartesian geometries make the Galerkin formulation very complex and tedious.

The numerical approximation of pipe flows via spectral or pseudospectral methods is not a new matter. There has been a long list of contributions regarding this issue in the recent past. Among other works, should be mentioned the methods proposed in Boberg & Brosa [3], Komminaho [32], Leonard & Reynolds [34], Leonard & Wray [35], O'Sullivan & Breuer [50], Priymak & Miyazaki [56], Shan *et al.* [67], for example. In Leonard & Wray [35], a solenoidal Fourier-Jacobi spectral method was proposed, elegantly solving the problem of the apparent singularity at the origin since the Jacobi polynomials used in the radial coordinate automatically satisfied the suitable analyticity conditions at the pole. Besides, the pressure terms were eliminated from the formulation via projection over a solenoidal space of test functions. The only weakness of the method proposed in Leonard & Wray [35] was the lack of a fast transform for the Jacobi polynomials and the clustering of radial points near the axis, thus considerably reducing the time step size in the time integrations. In a recent work [56], a Fourier-Chebyshev collocation method was formulated in primitive velocity-pressure variables, where Chebyshev polynomials of selected parity combined with half radial Gauss-Lobatto grid were used, thus avoiding clustering near the origin and allowing the use of a fast cosine transform. As far as I know, this is the first time where the combination proposed in Priymak & Miyazaki [56] has been used in Navier-Stokes equations in cylindrical coordinates.

In Meseguer & Trefethen [45], a spectral solenoidal Petrov-Galerkin scheme was used for the accurate computation of eigenvalues arising from the linearisation of the Navier-Stokes operator of the Hagen-Poiseuille flow. The analysis presented was focused on the asymptotic behaviour of the leading eigenvalues but the technical details of the spatial discretisation and its efficiency for nonlinear time dependent integrations had to wait until a complete nonlinear formulation of the scheme was provided and tested.

Here, a Galerkin method capable of simultaneously dealing with several difficulties arising from the Navier-Stokes equations in cylindrical unbounded geometries is presented. First, the construction of a solenoidal basis of trial functions for the velocity field in order to satisfy the incompressibility condition identically. In addition, this basis has to satisfy suitable physical boundary conditions at the pipe wall and also be analytic in a neighbourhood of the apparent singularity located at the origin in order to provide spectral accuracy. Second, the obtention of a dual basis of solenoidal test functions so that the pressure terms cancel out in the scheme once the projection has been carried out. The result of the projection should lead to inner products involving orthogonal or almost-orthogonal functions so that the resulting discretised operators are banded matrices. Third, devising an optimal quadrature rule in the radial variable capable of avoiding clustering of points near the center axis and allowing a fast transform in that variable if possible. Avoiding clustering near the pole should also improve the time step restrictions due to the CFL conditions. Fourth, developing a pseudospectral algorithm for the efficient computation of the nonlinear terms via partial summation techniques. Finally, the implementation of the described discretisation within a robust time marching scheme capable of overcoming the difficulties arising from the stiffness of the resulting systems of ODE.

This chapter is structured as follows. In section §2.1, the nonlinear initial-boundary stability problem is formulated mathematically. Section §2.2 is devoted to the detailed formulation of the trial and test solenoidal functions, focusing on their analyticity and radial symmetry properties. Section §2.3 describes the projection procedure that leads to the weak formulation of the problem as a dynamical system of amplitudes. In section §2.4, an analysis of the linear stability of the basic Hagen-Poiseuille flow is presented, mainly focused on detailed explorations regarding the structure of the eigenmodes, providing accurate numerical tables of eigenvalues to be compared with other spectral schemes. The time marching algorithm and the efficient computation of the nonlinear terms via pseudospectral collocation and partial summation techniques are explained in section §2.5. The validation of the numerical algorithm for unsteady computations is provided in section §2.6 based on a comparison with previous works and on a comparative performance analysis between two linearly implicit methods. Finally, section §2.7 is devoted to the numerical simulation of a particular transition to turbulence scenario in pipe flow. The main conclusions are summarised in section §2.8.

2.1 Formulation of the problem

We consider the motion of an incompressible viscous fluid of kinematic viscosity ν and density ρ. The fluid is driven through a circular pipe of radius a and infinite length by a uniform pressure gradient, Π_0, parallel to the axis of the pipe. We formulate the problem in cylindrical coordinates. The velocity of the fluid is prescribed by its radial ($\hat{\mathbf{r}}$), azimuthal ($\hat{\theta}$) and axial ($\hat{\mathbf{z}}$) components

$$\mathbf{v} = u\,\hat{\mathbf{r}} + v\,\hat{\theta} + w\,\hat{\mathbf{z}} = (u\ ,\ v\ ,\ w), \tag{2.1}$$

where u, v and w depend on the three spatial coordinates (r, θ, z) and time t. The motion of the fluid is governed by the incompressible Navier-Stokes equations

$$\partial_t \mathbf{v} + (\mathbf{v}\cdot\nabla)\mathbf{v} = -\frac{\Pi_0}{\rho}\hat{\mathbf{z}} - \nabla p + \nu\Delta\mathbf{v} \tag{2.2}$$

$$\nabla\cdot\mathbf{v} = 0, \tag{2.3}$$

where $\mathbf{v}$ is the velocity vector field, satisfying the no-slip boundary condition at the wall,

$$\mathbf{v}_{\text{pipe wall}} = \mathbf{0}, \tag{2.4}$$

and p is the reduced pressure. A basic steady solution of (2.2), (2.3) and (2.4) is the so-called *Hagen-Poiseuille flow*

$$\mathbf{v}_{\mathrm{B}} = (u_{\mathrm{B}}\ ,\ v_{\mathrm{B}}\ ,\ w_{\mathrm{B}}) = \left(0\ ,\ 0\ ,\ -\frac{\Pi_0 a^2}{4\rho\nu}\left[1-\left(\frac{r}{a}\right)^2\right]\right), \quad p_{\mathrm{B}} = \mathrm{C}, \tag{2.5}$$

where C is an arbitrary constant. This basic flow is a parabolic axial velocity profile which only depends on the radial coordinate [2]. The velocity of the fluid attains a maximum value $U_{\mathrm{CL}} = -\Pi_0 a^2/4\rho\nu$ at the center-line or axis of the cylinder.

Henceforth, all variables will be rendered dimensionless using a and U_{CL} as space and velocity units, respectively. The axial coordinate z is unbounded since the length of the pipe is infinite. In what follows, we assume that the flow is axially periodic with period b. In the dimensionless system, the spatial domain Ω of the problem is

$$\Omega = \{\ (r,\theta,z)\ |\ 0 \le r \le 1,\ \ 0 \le \theta < 2\pi,\ \ 0 \le z < \Lambda\} \tag{2.6}$$

where $\Lambda = b/a$ is the dimensionless length of the pipe, in radii units. In the new variables, the basic flow takes the form

$$\mathbf{v}_{\mathrm{B}} = (u_{\mathrm{B}}, v_{\mathrm{B}}, w_{\mathrm{B}}) = (0\ ,\ 0\ ,\ 1-r^2). \tag{2.7}$$

Finally, the parameter which governs the dynamics of the problem is the *Reynolds number*

$$Re = \frac{aU_{\mathrm{CL}}}{\nu}. \tag{2.8}$$

For the stability analysis, we suppose that the basic flow is perturbed by a solenoidal velocity field vanishing at the pipe wall

$$\mathbf{v}(r,\theta,z,t) = \mathbf{v}_{\mathrm{B}}(r) + \mathbf{u}(r,\theta,z,t), \quad \nabla\cdot\mathbf{u} = 0, \quad \mathbf{u}(r=1) = \mathbf{0}, \tag{2.9}$$

and a perturbation pressure field

$$p(r,\theta,z,t) = p_{\mathrm{B}}(z) + q(r,\theta,z,t). \tag{2.10}$$

On introducing the perturbed fields in the Navier-Stokes equations, we obtain a nonlinear initial-boundary problem for the perturbations $\mathbf{u}$ and q:

$$\begin{aligned}
\partial_t\mathbf{u} &= -\nabla q + \frac{1}{Re}\Delta\mathbf{u} - (\mathbf{v}_{\mathrm{B}}\cdot\nabla)\mathbf{u} - (\mathbf{u}\cdot\nabla)\mathbf{v}_{\mathrm{B}} - (\mathbf{u}\cdot\nabla)\mathbf{u}, && (2.11)\\
\nabla\cdot\mathbf{u} &= 0, && (2.12)\\
\mathbf{u}(1,\theta,z,t) &= 0, && (2.13)\\
\mathbf{u}(r,\theta+2\pi n,z,t) &= \mathbf{u}(r,\theta,z,t), && (2.14)\\
\mathbf{u}(r,\theta,z+l\Lambda,t) &= \mathbf{u}(r,\theta,z,t), && (2.15)\\
\mathbf{u}(r,\theta,z,0) &= \mathbf{u}_0, \quad \nabla\cdot\mathbf{u}_0 = 0, && (2.16)
\end{aligned}$$

for $(n,l)\in\mathbb{Z}^2$, $(r,\theta,z)\in[0,1]\times[0,2\pi)\times[0,\Lambda)$ and $t>0$. Equation (2.11) describes the nonlinear space-time evolution of the perturbation of the velocity field. Equation (2.12) is the solenoidal condition for the perturbation, and equations (2.13)–(2.15) describe the homogeneous boundary condition for the radial coordinate and the periodic boundary conditions for the azimuthal and axial coordinates respectively. Finally, equation (2.16) is the initial solenoidal condition for the perturbation field at $t=0$.

2.2 Trial and test solenoidal bases

This section will deal with the generation of solenoidal bases for our approximation of the vector field $\mathbf{u}$ appearing in (2.9). We discretise the perturbation $\mathbf{u}$ by a spectral approximation $\mathbf{u}_{\mathrm{S}}$ of order L in z, order N in θ, and order M in r,

$$\mathbf{u}_{\mathrm{S}}(r,\theta,z,t) = \sum_{l=-L}^{L}\sum_{n=-N}^{N}\sum_{m=0}^{M} a_{lnm}(t)\mathbf{\Phi}_{lnm}(r,\theta,z), \tag{2.17}$$

where $\mathbf{\Phi}_{lnm}$ are *trial* bases of solenoidal vector fields of the form

$$\mathbf{\Phi}_{lnm}(r,\theta,z) = \mathrm{e}^{\mathrm{i}(2\pi lz/\Lambda + n\theta)}\mathbf{v}_{lnm}(r), \tag{2.18}$$

satisfying

$$\nabla \cdot \mathbf{\Phi}_{lnm} = 0 \tag{2.19}$$

for $l = -L, \ldots, L$, $n = -N, \ldots, N$ and $m = 0, \ldots, M$. The trial bases (2.18) must satisfy certain regularity conditions at the origin, be periodic in the axial and azimuthal directions, and satisfy homogeneous boundary conditions at the wall,

$$\mathbf{\Phi}_{lnm}(1,\theta,z) = \mathbf{0}, \tag{2.20}$$

according to equations (2.12)–(2.15).

There are many different ways of obtaining divergence-free fields in polar coordinates [35, 43, 46]. The solenoidal condition (2.19) can be written as

$$(\partial_r + \frac{1}{r})u_{lnm} + \frac{\mathrm{i}n}{r}v_{lnm} + \mathrm{i}l\frac{2\pi}{\Lambda}w_{lnm} = 0, \tag{2.21}$$

where

$$\mathbf{v}_{lnm} = u_{lnm}\,\hat{\mathbf{r}} + v_{lnm}\,\hat{\theta} + w_{lnm}\,\hat{\mathbf{z}} = (\ u_{lnm}\ ,\ v_{lnm}\ ,\ w_{lnm}\ )\,. \tag{2.22}$$

Equation (2.21) introduces a linear dependence between the three components of $\mathbf{v}_{lnm}$, leading to two degrees of freedom. In what follows, we define

$$\mathrm{h}_m(r) = (1-r^2)\mathrm{T}_{2m}(r), \quad \mathrm{g}_m(r) = (1-r^2)\mathrm{h}_m(r), \quad \mathrm{D} = \frac{\mathrm{d}}{\mathrm{d}r}, \quad \mathrm{D}_+ = \mathrm{D} + \frac{1}{r}, \quad \mathrm{k}_0 = \frac{2\pi}{\Lambda} \tag{2.23}$$

where $\mathrm{T}_{2m}(r)$ is the Chebyshev polynomial of degree $2m$ and $r \in [0,1]$, and k_0 stands for the fundamental axial wavenumber in the axial coordinate. Following the regularisation rules proposed in Priymak & Miyazaki [56], we distinguish two cases:

I. Axisymmetric fields ($n = 0$): The basis is spanned by the elements

$$\mathbf{\Phi}^{(1)}_{l0m} = \mathrm{e}^{\mathrm{i}\mathrm{k}_o lz}\mathbf{v}^{(1)}_{l0m} = \mathrm{e}^{\mathrm{i}\mathrm{k}_o lz}\,(\ 0\ ,\ r\mathrm{h}_m\ ,\ 0\ )\,, \tag{2.24}$$

$$\mathbf{\Phi}^{(2)}_{l0m} = \mathrm{e}^{\mathrm{i}\,\mathrm{k}_o l\,z}\mathbf{v}^{(2)}_{l0m} = \mathrm{e}^{\mathrm{i}\,\mathrm{k}_o l\,z}\,(\ -\mathrm{i}\mathrm{k}_o\ l\ r\mathrm{g}_m\ ,\ 0\ ,\ \mathrm{D}_+[r\mathrm{g}_m]\ )\,, \tag{2.25}$$

except that if $l = 0$, the third component of $\mathbf{\Phi}^{(2)}_{lnm}$ is replaced by $\mathrm{h}_m(r)$.

II. Non-axisymmetric fields ($n \neq 0$): In this case, the basis is spanned by the elements

$$\mathbf{\Phi}^{(1)}_{lnm} = \mathrm{e}^{\mathrm{i}(n\,\theta + \mathrm{k}_o l\,z)}\mathbf{v}^{(1)}_{lnm} = \mathrm{e}^{\mathrm{i}(n\,\theta + \mathrm{k}_o l\,z)}\,\big(\ -\mathrm{i}\ n\ r^{\sigma-1}\ \mathrm{g}_m\ ,\ \mathrm{D}[r^\sigma\ \mathrm{g}_m]\ ,\ 0\ \big)\,, \tag{2.26}$$

$$\mathbf{\Phi}^{(2)}_{lnm} = \mathrm{e}^{\mathrm{i}(n\,\theta+\mathrm{k}_o l\,z)}\mathbf{v}^{(2)}_{lnm} = \mathrm{e}^{\mathrm{i}(n\,\theta+\mathrm{k}_o l\,z)}\left(\,0\,,\;-\mathrm{i}\mathrm{k}_o\,l\,r^{\sigma+1}\,\mathrm{h}_m\,,\;\mathrm{i}\,n\,r^{\sigma}\mathrm{h}_m\,\right), \tag{2.27}$$

where

$$\sigma = \begin{cases} 2 & (n \text{ even}) \\ 1 & (n \text{ odd}). \end{cases} \tag{2.28}$$

The binomial factors $(1-r^2)$ and $(1-r^2)^2$ appearing in $\mathrm{h}_m(r)$ and $\mathrm{g}_m(r)$ are responsible for the boundary conditions (2.20) at the pipe wall to be satisfied. Factors of the form $1-r$ or $(1-r)^2$ would also solve the boundary problem, but they would violate the parity conditions established by Theorem 1 of Priymak & Miyazaki [56]. The monomials r, r^σ and $r^{\sigma\pm1}$ appearing in equations (2.24 - 2.27) enforce the conditions of regularity and parity at the pole. The pure imaginary factors in $\mathbf{\Phi}^{(2)}_{lnm}$ could be dispensed with, but we leave them in so that the basis functions have a desirable symmetry property: if l and n are negated, each basis function is replaced by its complex conjugate, i.e.,

$$\left[\mathbf{\Phi}^{(1,2)}_{lnm}\right]^* = \mathbf{\Phi}^{(1,2)}_{-l,\,-n,\;m} \quad . \tag{2.29}$$

The Galerkin scheme is accomplished when projecting the trial functions above described over a suitable dual or test space of vector fields. We consider the inner product $(\cdot,\cdot)$ as the volume integral over the domain of the pipe:

$$(\mathbf{a},\mathbf{b}) = \int_0^{\Lambda}\int_0^{2\pi}\int_0^1 \mathbf{a}^*\cdot\mathbf{b}\;r\mathrm{d}r\;\mathrm{d}\theta\;\mathrm{d}z, \tag{2.30}$$

where $*$ stands for complex conjugate, $\mathbf{b}$ belongs to the physical or trial space and $\mathbf{a}$ is a solenoidal vector field belonging to the test or projection space still to be determined. We focus our attention on the radial integration involved in (2.30). Since the variable of the Chebyshev polynomials considered in the trial functions is the radius r, we need to relate that integral to an orthogonal product in the extended domain $r\in[-1,1]$. A straightforward solution is to assume that

$$\int_0^1 \mathbf{a}^*\cdot\mathbf{b}\quad r\mathrm{d}r = \frac{1}{2}\int_{-1}^1 \mathbf{a}^*\cdot\mathbf{b}\quad r\mathrm{d}r. \tag{2.31}$$

The previous equation is only true if the integrand $\mathbf{a}^*\cdot\mathbf{b}\quad r$ is an *even* function of the radius. This is the *crucial* point of the spectral projection in the radial variable. In order to satisfy equation (2.31), the test functions will consist of even Chebyshev polynomials $\mathrm{T}_{2m}(r)$, previously factorised with the Chebyshev weight $(1-r^2)^{-1/2}$ and suitable monomials r^β so that the integrand becomes symmetric with respect to the center axis and the integrals can be computed exactly by using quadrature formulas.

For the test functions $\mathbf{\Psi}_{lnm}(r,\theta,z)$, we distinguish again two different situations:

I. Axisymmetric fields ($n = 0$): In this case, the basis is spanned by the elements

$$\mathbf{\Psi}^{(1)}_{l0m} = \mathrm{e}^{\mathrm{i}\,\mathrm{k}_o l\,z}\tilde{\mathbf{v}}^{(1)}_{l0m}(r) = \frac{\mathrm{e}^{\mathrm{i}\,\mathrm{k}_o l\,z}}{\sqrt{1-r^2}}\,(\,0\,,\,\mathrm{h}_m\,,\,0\,)\,, \tag{2.32}$$

$$\mathbf{\Psi}^{(2)}_{l0m} = \mathrm{e}^{\mathrm{i}\,\mathrm{k}_o l\,z}\tilde{\mathbf{v}}^{(2)}_{l0m} = \frac{\mathrm{e}^{\mathrm{i}\,\mathrm{k}_o l\,z}}{\sqrt{1-r^2}}\,\left(\,-\mathrm{k}_o \mathrm{i}\,l\,r^2\mathrm{g}_m\,,\,0\,,\,\mathrm{D}_+[r^2\mathrm{g}_m] + r^3\,\mathrm{h}_m\,\right), \tag{2.33}$$

except that the third component of the vector in $\mathbf{\Psi}^{(2)}_{l0m}$ is replaced by $r\mathrm{h}_m(r)$ if $l = 0$.

II. Non-axisymmetric fields ($n \neq 0$): In this case, the basis is spanned by the elements

$$\mathbf{\Psi}^{(1)}_{lnm} = \mathrm{e}^{\mathrm{i}(n\,\theta+\mathrm{k}_o l\,z)}\tilde{\mathbf{v}}^{(1)}_{lnm} = \frac{\mathrm{e}^{\mathrm{i}(n\,\theta+\mathrm{k}_o l\,z)}}{\sqrt{1-r^2}}\,\left(\,\mathrm{i}\,n\,r^{\beta}\mathrm{g}_m\,,\,\mathrm{D}[r^{\beta+1}\,\mathrm{g}_m] + r^{\beta+2}\mathrm{h}_m\,,\,0\,\right), \tag{2.34}$$

$$\mathbf{\Psi}^{(2)}_{lnm} = \mathrm{e}^{\mathrm{i}(n\,\theta+\mathrm{k}_o l\,z)}\tilde{\mathbf{v}}^{(2)}_{lnm} = \frac{\mathrm{e}^{\mathrm{i}(n\,\theta+\mathrm{k}_o l\,z)}}{\sqrt{1-r^2}}\,\left(\,0\,,\,-\mathrm{k}_o \mathrm{i}\,l\,r^{\beta+2}\mathrm{h}_m\,,\,\mathrm{i}\,n\,r^{\beta+1}\,\mathrm{h}_m\,\right), \tag{2.35}$$

except that the third component of the vector in $\mathbf{\Psi}^{(2)}_{lnm}$ is replaced by $r^{1-\beta}\mathrm{h}_m(r)$ if $l = 0$, where

$$\beta = \begin{cases} 0 & (n \text{ even}) \\ 1 & (n \text{ odd}). \end{cases} \tag{2.36}$$

These vector fields include the Chebyshev factor $(1-r^2)^{-1/2}$ and suitable monomials so that the symmetrisation rule (2.31) holds. Therefore, the products between the test and trial functions can be exactly calculated via *Gauss-Lobatto* quadrature, leading to banded matrices. Since the test and trial functions are not the same, this projection procedure is usually known as *Petrov-Galerkin* scheme.

In the radial coordinate, we consider the Gauss-Lobatto points

$$r_k = -\cos\left(\frac{\pi k}{M_r}\right), \quad k = 0, \ldots, M_r, \tag{2.37}$$

where we will assume that M_r is *odd* and of suitable order so that the quadratures are exact. The spectral differentiation matrix is given by

$$(\mathbb{D}_r)_{ij} = \begin{cases} (1+2M_r^2)/6 & i = j = M_r \\ -(1+2M_r^2)/6 & i = j = 0 \\ -\dfrac{r_i}{2(1-r_i^2)} & i = j\ ;\ 0 < i < M_r \\ (-1)^{i+j}\ \dfrac{c_j}{c_i(r_j - r_i)} & i \neq j \end{cases}, \tag{2.38}$$

where $c_j = 1$ for $0 < j < M_r$ and $c_0 = c_{M_r} = 2$ [4, 70]. The radial, azimuthal and axial components of the trial functions $\mathbf{\Phi}^{(1,2)}_{lnm}$ are either *even* or *odd* functions of r. Therefore, we only need to consider the positive part of the grid

$$r_k^+ = -\cos\left(\frac{\pi k}{M_r}\right), \quad k = \frac{M_r+1}{2}, \ldots, M_r. \tag{2.39}$$

For arbitrary even, $\mathrm{f_e}(r)$, or odd, $\mathrm{f_o}(r)$, functions satisfying

$$\mathrm{f_e}(r_k) = \mathrm{f_e}(r_{M_r-k}), \quad \mathrm{f_o}(r_k) = -\mathrm{f_o}(r_{M_r-k}), \qquad k = 0, \ldots, \frac{M_r-1}{2}, \tag{2.40}$$

the differentiation matrices which provide the first derivatives

$$\left(\frac{\mathrm{df_e}}{\mathrm{d}r}\right)_{r=r_i^+} = (\mathbb{D}_r^{\mathrm{e}})_{ij}\ \mathrm{f_e}(r_j^+), \quad \left(\frac{\mathrm{df_o}}{\mathrm{d}r}\right)_{r=r_i^+} = (\mathbb{D}_r^{\mathrm{o}})_{ij}\ \mathrm{f_o}(r_j^+), \tag{2.41}$$

are obtained from the Chebyshev matrix (2.38):

$$(\mathbb{D}_r^{\mathrm{e}})_{ij} = (\mathbb{D}_r)_{ij} + (\mathbb{D}_r)_{i\ M_r-j}, \quad i,j = \frac{M_r+1}{2}, \ldots, M_r, \tag{2.42}$$

and

$$(\mathbb{D}_r^{\mathrm{o}})_{ij} = (\mathbb{D}_r)_{ij} - (\mathbb{D}_r)_{i\ M_r-j}, \quad i,j = \frac{M_r+1}{2}, \ldots, M_r. \tag{2.43}$$

For the periodic azimuthal and axial coordinates, we use standard equispaced grids

$$(z_i, \theta_j) = (\frac{\Lambda}{L_z} i, \frac{2\pi}{N_\theta} j), \quad (i,j) = [0, L_z - 1] \times [0, N_\theta - 1], \tag{2.44}$$

where we assume that N_θ and L_z are odd, and we make use of the standard Fourier matrix [21] for the differentiation of fields with respect to those variables.

2.3 Dynamical system of amplitudes

The spectral Petrov-Galerkin scheme is accomplished by substituting expansion (2.17) in (2.11) and projecting over the set of test vector fields (2.32-2.33) and (2.34-2.35)

$$(\mathbf{\Psi}_{lnm}\ ,\ \partial_t \mathbf{u}_{\mathrm{S}}) = \left(\mathbf{\Psi}_{lnm}\ ,\ \frac{1}{Re}\Delta\mathbf{u}_{\mathrm{S}} - (\mathbf{v}_{\mathrm{B}}\cdot\nabla)\mathbf{u}_{\mathrm{S}} - (\mathbf{u}_{\mathrm{S}}\cdot\nabla)\mathbf{v}_{\mathrm{B}} - (\mathbf{u}_{\mathrm{S}}\cdot\nabla)\mathbf{u}_{\mathrm{S}}\right), \tag{2.45}$$

for $l = -L, \ldots, L$, $n = -N, \ldots, N$ and $m = 0, \ldots, M$. We have not included the pressure term ∇q of (2.11) in the projection scheme (2.45). One of the advantages of our method is that the pressure term is cancelled in the projection, i.e.,

$$(\mathbf{\Psi}_{lnm}\ ,\ \nabla q) = 0; \tag{2.46}$$

see Canuto *et al.* [7] or Leonard & Wray [35], as an example.

Once the projection has been carried out, the spatial dependence has been eliminated from the problem and a nonlinear dynamical system for the amplitudes a_{lnm} is obtained. Symbolically, this system reads

$$\mathbb{A}^{lnm}_{pqr}\ \dot{a}_{pqr} = \mathbb{B}^{lnm}_{pqr}\ a_{pqr} - b_{lnm}(a,a), \tag{2.47}$$

where we have used the convention of summation with respect to repeated subscripts. The discretised operator $\mathbb{A}$ appearing in (2.47) is the projection

$$\mathbb{A}^{lnm}_{pqr} = (\boldsymbol{\Psi}_{lnm}\ ,\ \boldsymbol{\Phi}_{pqr}) = 2\pi\Lambda\delta^l_p\delta^n_q \int_0^1 \tilde{\mathbf{v}}^*_{lnm}\cdot\mathbf{v}_{pqr} r\mathrm{d}r, \tag{2.48}$$

where δ^i_j is the Kronecker symbol. The inner product (2.48) reveals another advantage of the Galerkin scheme. Due to the linearity of the time diferentiation operator ∂_t and the Fourier orthogonality in the periodic variables, the axial and azimuthal modes decouple. The operator $\mathbb{B}$ in (2.47),

$$\mathbb{B}^{lnm}_{pqr} = \left(\boldsymbol{\Psi}_{lnm}\ ,\ \frac{1}{Re}\Delta\boldsymbol{\Phi}_{pqr} - (\mathbf{v}_{\mathrm{B}}\cdot\nabla)\boldsymbol{\Phi}_{pqr} - (\boldsymbol{\Phi}_{pqr}\cdot\nabla)\mathbf{v}_{\mathrm{B}}\right), \tag{2.49}$$

satisfies the same orthogonality properties in the periodic variables. As a result, those operators $\mathbb{A}^{lnm}_{pqr}$ and $\mathbb{B}^{lnm}_{pqr}$ with different axial indices ($l \neq p$) or different azimuthal ones ($n \neq q$) are identically zero. The remaining operators with $l = p$ and $n = q$ have a banded structure due to the orthogonality properties of the shifted Chebyshev basis used in the radial variable. In Fig. 2.1 we have represented the sparse structure of both operators for the particular case $l = p = 1$ and $n = q = 1$. A clever reordering of the vector of coefficients makes $\mathbb{A}$ and $\mathbb{B}$ collapse into a single band structure. The quadratic form $b_{lnm}(a,a)$ appearing in (2.47) corresponds to the projection of the nonlinear convective term

$$(\boldsymbol{\Psi}_{lnm}\ ,\ (\mathbf{u}_{\mathrm{S}}\cdot\nabla)\mathbf{u}_{\mathrm{S}})\,. \tag{2.50}$$

For computational efficiency, this term has to be calculated via a pseudospectral method. The details of this computation will be analysed later. Finally, the initial value problem is prescribed by the coefficients $a_{lnm}(0)$ representing the initial vector field $\mathbf{u}^0_{\mathrm{S}}$ given by

$$a_{lnm}(t=0) = \left(\boldsymbol{\Psi}_{lnm}\ ,\ \mathbf{u}^0_{\mathrm{S}}\right). \tag{2.51}$$

2.4 Linear stability

The stability of very small perturbations added to the basic flow is dictated by the linearised equation

$$\mathbb{A}^{lnm}_{pqr}\ \dot{a}_{pqr} = \mathbb{B}^{lnm}_{pqr}\ a_{pqr}, \tag{2.52}$$

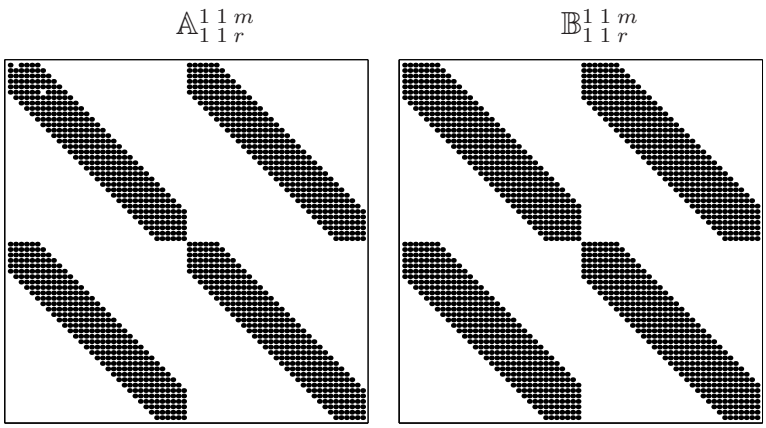

Figure 2.1: Sparse structure of operators $\mathbb{A}^{lnm}_{pqr}$ and $\mathbb{B}^{lnm}_{pqr}$ for $l = p = 1$ and $n = q = 1$, with $M = 32$ radial modes

obtained from (2.47), where we have neglected the nonlinear advective term. Therefore, since the problem is linear, we can decouple the eigenvalue analysis for each independent azimuthal-n and axial-l wavenumbers associated with the $\mathrm{e}^{\mathrm{i}(n\theta+kz)}$ *normal mode*, where $k = l\mathrm{k}_o$. For a fixed axial and azimuthal periodicity, the spectrum is given by the eigenvalues of the operator $\mathbb{L} = \mathbb{A}^{-1}\mathbb{B}$,

$$\mathbb{L}\,\mathbf{a} = \lambda\,\mathbf{a}, \tag{2.53}$$

where the operators $\mathbb{A}$ and $\mathbb{B}$ are the matrices (2.48) and (2.49) corresponding to the axial-azimuthal mode (n, l) under study, λ is an eigenvalue of the spectrum of $\mathbb{L}$, and $\mathbf{a}$ is its associated *eigenvector*

$$\mathbf{a} = (a_1^{(1)}, \ldots, a_M^{(1)}, a_1^{(2)}, \ldots, a_M^{(2)})^{\mathrm{T}}, \tag{2.54}$$

where we have omitted the axial and azimuthal subscripts for simplicity.

The convergence and reliability of the spectral method have been checked. For this purpose, some of the results reported here have been compared with previous works. For example, in Table 2.1, the convergence of the least stable eigenvalue has been tested for $Re = 9600$, $n = 1$ and $k = 1$, a case previously studied by other authors [35, 56]. For $Re = 3000$, the spectra for different values of k and n have been computed in order to make comparisons with a first comprehensive linear stability analysis carried out in Schmid & Henningson [62]. Our code provided spectral accuracy in all the computed cases. In Tables 2.2 and 2.3, the spectra of the 10 rightmost eigenvalues have been listed for $(k = 1,\ n = 0, 1)$ and $(k = 1,\ n = 2, 3)$, respectively, following Schmid and Henningson's former study.

The same computation has been done for *streamwise-independent* perturbations ($k = 0$) and for different values of the azimuthal mode n (see Table 2.4). To the author's knowl-

M	*size*	λ_1		
20	42×42	−0.0229	+	i 0.950
30	62×62	−0.0231707	+	i 0.9504813
40	82×82	−0.02317079576	+	i 0.950481396669
50	102×102	−0.023170795764	+	i 0.950481396670

Leonard & Wray (1982)	$\lambda_1 = -0.023170795764 + \mathrm{i}\, 0.950481396668$
Priymak & Miyazaki (1998)	$\lambda_1 = -0.023170795765 + \mathrm{i}\, 0.950481396670$

Table 2.1: Convergence test for $Re = 9600$, $k = 1$ and $n = 1$, following Leonard & Wray [35] and Priymak & Miyazaki [56]. M is the number of Chebyshev polynomials used in our spectral approximation, *size* is the dimension of the discretisation matrices appearing in Fig. 2.1 and λ_1 stands for the rightmost eigenvalue. The reported figures are those which apparently converged at M=60.

$n = 0$			$n = 1$		
−0.0519731112828	+	i 0.9483602220505	−0.041275644693	+	i 0.91146556762
−0.0519731232053	+	i 0.948360198487	−0.0616190180049	+	i 0.370935092697
−0.103612364039	+	i 0.896719200867	−0.088346025188	+	i 0.958205542989
−0.103612889227	+	i 0.8967204441	−0.0888701566	+	i 0.8547888174
−0.112217160388	+	i 0.4123963342099	−0.1168771535871	+	i 0.216803862997
−0.121310028246	+	i 0.2184358147279	−0.137490337	+	i 0.7996994696
−0.155220165293	+	i 0.8450717997117	−0.14434614486	+	i 0.91003730954
−0.155252667198	+	i 0.845080668126	−0.1864329862	+	i 0.7453043578
−0.2004630477669	+	i 0.3762423600255	−0.195839466	+	i 0.5493115826
−0.20647681141	+	i 0.79378412983	−0.198646109	+	i 0.8607494634

Table 2.2: Rightmost eigenvalues for $Re = 3000$, $k = 1$ and $n = 0, 1$, following Schmid & Henningson [62]. The reported figures are apparently converged at $M = 54$.

$n = 2$			$n = 3$		
−0.060285689559	+	i 0.88829765875	−0.08325397694	+	i 0.86436392104
−0.08789898037	+	i 0.352554927087	−0.105708407362	+	i 0.346401953386
−0.1088383407	+	i 0.8328933609	−0.116877921343	+	i 0.2149198697617
−0.112001616152	+	i 0.939497219531	−0.1323924331	+	i 0.8097468023
−0.1155143802215	+	i 0.215491816529	−0.136035459528	+	i 0.91671917468
−0.15810861	+	i 0.778584987	−0.182036372	+	i 0.7558793156
−0.167294045951	+	i 0.8906185726	−0.190639836903	+	i 0.8674136555
−0.20759146658	+	i 0.725077139	−0.2127794121	+	i 0.37123649827
−0.20931432998	+	i 0.37502653759	−0.23181786	+	i 0.70300722
−0.2214747313	+	i 0.8409753749	−0.244111241	+	i 0.551731632

Table 2.3: Same as Table 2.2 for $n = 2, 3$.

$n=0$	$n=1$	$n=2$	$n=3$
−0.0019277286542	−0.00489399021	−0.0087915387	−0.0135688219
−0.004893990214	−0.0087915388	−0.01356882195	−0.01919431362
−0.0101570874478	−0.0164061521	−0.0236166663	−0.03175919084
−0.01640615210723	−0.0236166663	−0.03175919085	−0.040809265355
−0.0249623355969	−0.03449981796	−0.04500690295	−0.0564651499
−0.034499817965	−0.045006902955	−0.05646514994	−0.06885660345
−0.0463467614754	−0.059173588937	−0.0729733963	−0.087733618
−0.0591735889378	−0.072973396381	−0.08773361808	−0.103440753288
−0.07431076787255	−0.090427218091	−0.1075183721	−0.1255751331
−0.0904272180909	−0.107518372097	−0.12557513314	−0.14458704546

Table 2.4: Same as Tables 2.2, 2.3 for $k=0$, $n=0,1,2,3$.

edge, numerical tables of streamwise-independent modes have not been reported previously. Mathematically, the case $k=0$ needs a special treatment. In fact, the limit $k\to 0$ does not coincide with this case. In our formulation, this phenomenon can be understood looking at the boundary conditions which must be satisfied by the radial velocity over the wall. For $k\neq 0$, the radial velocity, as well as its first derivative, must vanish over the wall. For $k=0$ the boundary conditions change abruptly.

Our formulation in solenoidal primitive vector fields allows to obtain the explicit expression of a *first integral* of the perturbation field, i.e., a manifold over which the fluid particles lie on for all t. The obtention of a closed form of these stream functions is possible because of the (θ,z) invariance transformation induced by the normal mode analysis. The normal mode $\mathrm{e}^{\mathrm{i}(n\theta+kz)}$ is invariant under *spiral* transformations of the form:

$$\frac{\mathrm{d}z}{\mathrm{d}\theta}=-\frac{n}{k}. \tag{2.55}$$

We define a *spiral variable* $\zeta\doteq n\theta+kz$, so that the solenoidal condition

$$\nabla\cdot\mathbf{v}=\frac{1}{r}\partial_r(rv_r)+\frac{1}{r}\partial_\theta v_\theta+\partial_z v_z=0$$

can be expressed as

$$\partial_r(rv_r)+\partial_\zeta[nv_\theta+rkv_z]=0, \tag{2.56}$$

where we have used the differentiation rules

$$\partial_\theta=(\partial_\theta\zeta)\partial_\zeta=n\partial_\zeta,\quad \partial_z=(\partial_z\zeta)\partial_\zeta=k\partial_\zeta.$$

Equation (2.56) defines implicitly a first integral $\Theta(r,\zeta)$ satisfying

$$\partial_\zeta\Theta=-rv_r, \tag{2.57}$$

and

$$\partial_r \Theta = n v_\theta + r k v_z. \tag{2.58}$$

A straightforward integration of (2.58) leads to the explicit expression of Θ for cases **I** and **II** described in §2.2. The physical vector field is a real object obtained from solving the eigenvalue problem (2.53) associated with the normal mode $\mathrm{e}^{\mathrm{i}(n\theta+kz)}$ and its conjugated:

$$\mathbf{u} = 2\Re\{\mathrm{e}^{\mathrm{i}(kz+n\theta)} \sum_{m=0}^{M} a_m^{(1)} \mathbf{v}_m^{(1)} + a_m^{(2)} \mathbf{v}_m^{(2)}\}, \tag{2.59}$$

where the subscripts l and n have been omitted for simplicity. From equations (2.24-2.27) and (2.58) we can obtain explicit expressions for the first integral Θ:

I. Axisymmetric fields ($n = 0$):

$$\Theta(r,\theta,z) = 2kr^2 \, \Re\left\{ \mathrm{e}^{\mathrm{i}kz} \sum_{m=0}^{M} a_m^{(2)} \mathrm{g}_m(r) \right\}, \tag{2.60}$$

except that Θ is a constant if $k = 0$.

II. Non-axisymmetric fields ($n \neq 0$):

$$\Theta(r,\theta,z) = 2nr^\sigma \, \Re\left\{ \mathrm{e}^{\mathrm{i}(kz+n\theta)} \sum_{m=0}^{M} a_m^{(1)} \mathrm{g}_m(r) \right\}, \tag{2.61}$$

for all k.

In Fig. 2.2 we have represented the spectrum of eigenvalues computed for $Re = 3000$, $n = 1$ and $k = 1$. Three different branches are clearly identified; wall modes branch (WM), center modes branch (CM) and mean modes branch (MM) [15, 14]. In order to have a qualitative idea of the dynamics associated with each one of the three branches, we have plotted the velocity field $\mathbf{v}$ computed from (2.59) and the first integral obtained from (2.61) in Fig. 2.3, for the three selected eigenvalues in Fig. 2.2. In particular, we have represented the eigenfunctions corresponding to the *wall*, *center* and *mean* eigenvalues previously shown in Fig. 2.2. The pictures corresponding to the center and wall modes shown in Fig. 2.3 have recently appeared in Drazin [14].

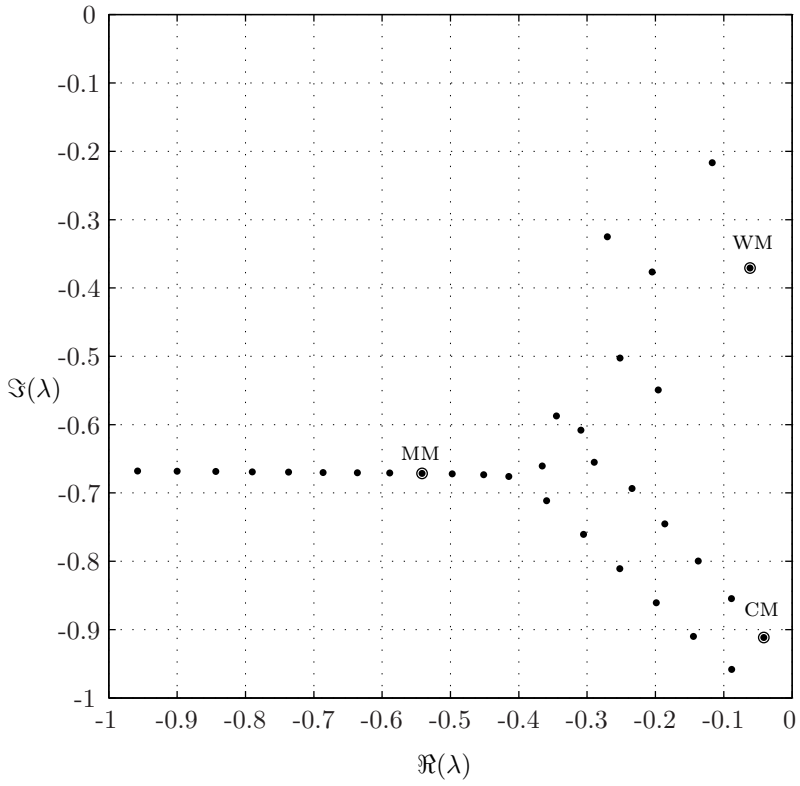

Figure 2.2: Spectrum of eigenvalues for $Re = 3000$, $n = 1$, $k = 1$. The labelled dots WM (wall mode), CM (center mode) and MM (mean mode) are the eigenvalues whose associated eigenfunctions have been plotted in Fig. 2.3.

2.5 Nonlinear unsteady computations

2.5.1 Overview

The numerical approach to the resolution of the fully nonlinear problem described in this section was first devised in Meseguer & Trefethen [44]. The spectral spatial discretisation of the Navier-Stokes equations leads to a *stiff* system of ODEs [4, 23, 29], characterised by the presence of modes with vastly different time-scales. This pathology leads to stability problems in the time discretisation, in particular when explicit time integration schemes are used. The development of numerical algorithms for the solution of stiff systems is an active research area where new methodologies appear frequently. In spectral discretisation of nonlinear PDEs, the more standard procedures are based on *semi-implicit*, also called *linearly implicit* methods, where the linear part is integrated implicitly and the nonlinear terms are treated explicitly. In a recent work, by Cox & Matthews [10], *Exponential*

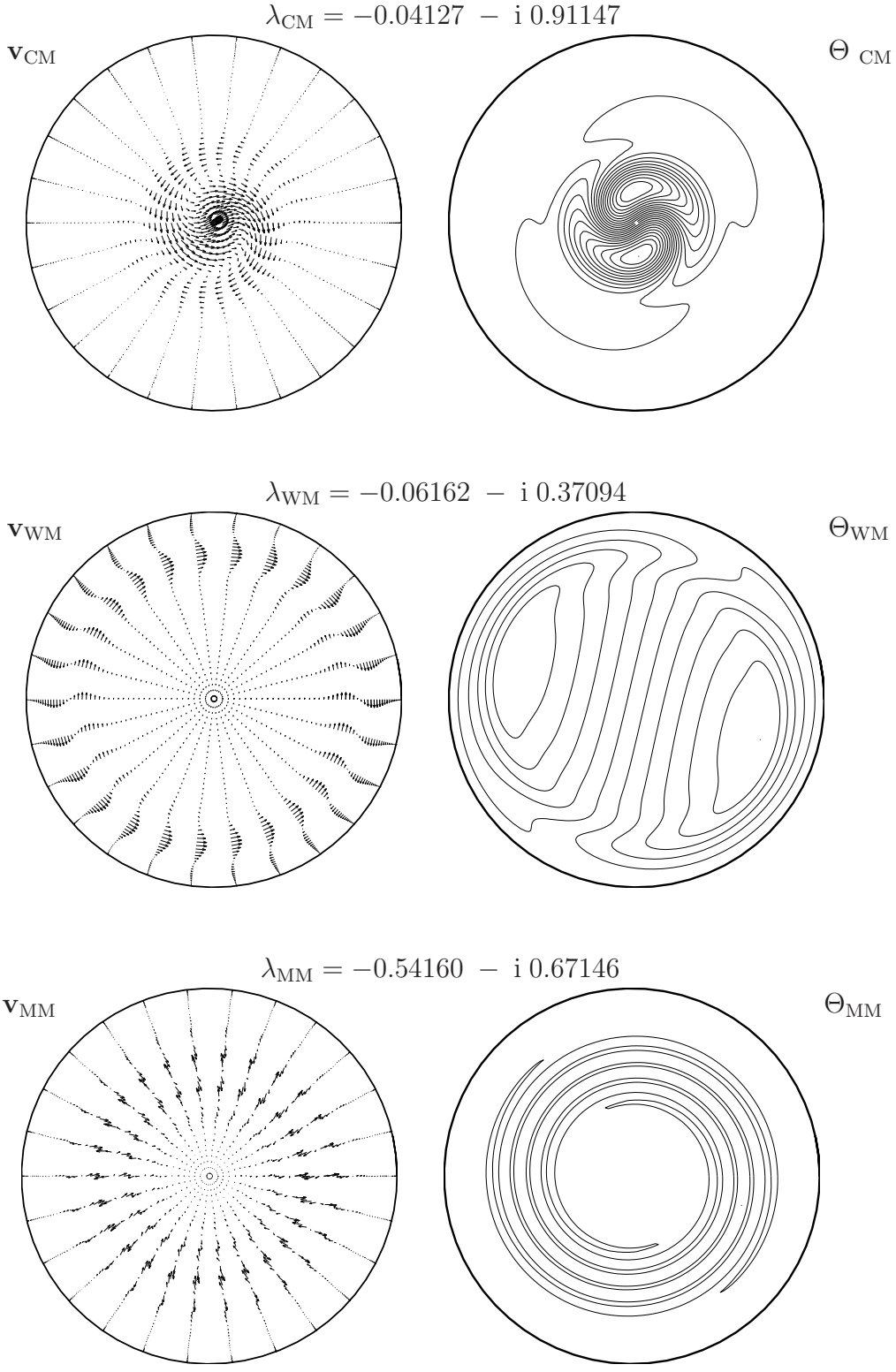

Figure 2.3: Eigenmodes corresponding to the three selected eigenvalues of Fig. 2.2.

Time Differencing (ETD) schemes were proved to be more efficient for some stiff PDEs, in comparison with standard linearly implicit, integrating factor or splitting methods. Nevertheless, ETD methods lead to technical complications when the domain of the problem has no periodicity or when the linearised operator $\mathbb{L}$ appearing in equation (2.53) is (or is close to be) singular. For moderately high Reynolds numbers, the ill-conditioning of the linearised Navier-Stokes operator and the radial-Chebyshev spectral interpolation make the ETD scheme not feasible for practical purposes.

Second and fourth order linearly implicit time integration schemes have been tested for unsteady computations of transitional regimes in pipe flow. In particular, implicit *Backward Differences*, combined with modified *Adams-Bashforth* polynomial extrapolation (also termed AB_2BD_2 and AB_4BD_4 in Cox & Matthews [10]), have been used. It is well known that BD_4 method may lead to stability problems [23]. Nevertheless, we found AB_4BD_4 as the best scheme for this particular problem.

2.5.2 Linearly implicit time integration

Let Δt be the time step and $t^{(k)} = k\ \Delta t, \quad k = 0, 1, 2, \ldots$ the time array where we approximate our amplitudes $a(t)$ [1] from the original system (2.47). In our notation, $a^{(k)} = a(t^{(k)})$ is the approximation of $a(t)$ at $t = t^{(k)}$ and $b^{(k)}$ is the nonlinear quadratic form appearing in (2.47) evaluated at $t^{(k)}$, i.e., $b^{(k)} = b(a^{(k)}, a^{(k)})$. The second order AB_2BD_2 method is given by the iteration

$$(3\ \mathbb{A} - 2\ \Delta t\ \mathbb{B})a^{(k+1)} = \mathbb{A}(4a^{(k)} - a^{(k-1)}) - 2\Delta t\ (2b^{(k)} - b^{(k-1)}), \tag{2.62}$$

for $k \geq 1$, see Cox & Matthews [10], whereas the fourth-order AB_4BD_4 scheme is

$$\begin{array}{rcl} (25\ \mathbb{A} - 12\ \Delta t\ \mathbb{B})\, a^{(k+1)} & = & \mathbb{A}\left(48a^{(k)} - 36a^{(k-1)} + 16a^{(k-2)} - 3a^{(k-3)}\right) \\ & & -\Delta t\ \left(48b^{(k)} - 72b^{(k-1)} + 48b^{(k-2)} - 12b^{(k-3)}\right)\ , \end{array} \tag{2.63}$$

for $k \geq 3$. In both schemes, the initial value $a^{(0)}$ is prescribed by the initial condition (2.51), and the first unknown amplitudes, $a^{(1)}$ for (2.62) or $a^{(1,2,3)}$ for (2.63), are obtained by means of a fourth-order *Runge-Kutta* explicit method.

The nonlinear explicit contributions $b^{(k)}$ appearing in (2.62) and (2.63) must be efficiently computed in advance by means of a *de-aliased* pseudospectral or collocation method.

[1] To avoid cumbersome notation, we temporarily suppress the subscripts corresponding to the spatial discretisation.

The main goal is to compute the term

$$b_{lnm} = (\mathbf{\Psi}_{lnm}, (\mathbf{u}_{\rm S} \cdot \nabla)\mathbf{u}_{\rm S}) = \int_0^{\Lambda} \int_0^{2\pi} \int_0^1 \mathbf{\Psi}^*_{lnm} \cdot (\mathbf{u}_{\rm S} \cdot \nabla)\mathbf{u}_{\rm S} \; r \mathrm{d}r \; \mathrm{d}\theta \; \mathrm{d}z, \tag{2.64}$$

where $\mathbf{u}_{\rm S}$ is given by the known coefficients $a^{(k)}$ appearing in expansion (2.17), at a previous stage in time. The standard procedure for the computation of the nonlinear advective term is summarised in the diagram of Fig. 2.4. Basically, once the coefficients a_{lnm} (top left of

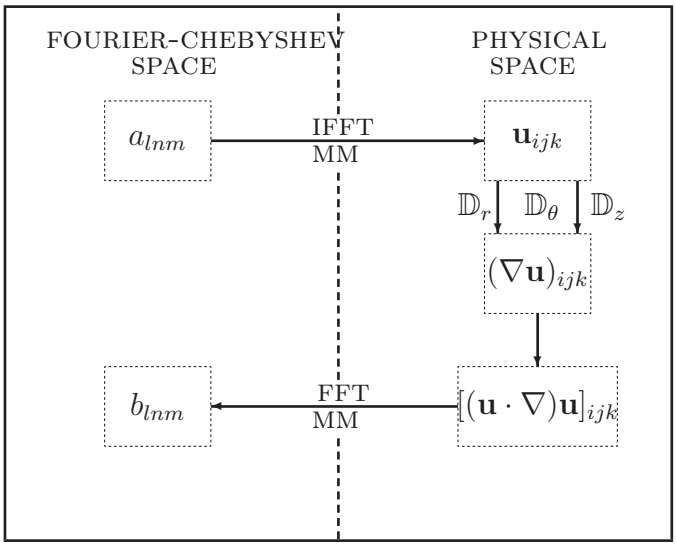

Figure 2.4: Pseudospectral computation of the nonlinear term. The abbreviations FFT, IFFT and MM stand for *Fast Fourier Transform*, *Inverse Fast Fourier Transform* and *Matrix Multiplication*, respectively.

the diagram) of $\mathbf{u}_{\rm S}$ are known, we evaluate $\mathbf{u}_{\rm S}$ in the physical space (top arrow going from left to right in the diagram). The gradient of the vector field, $\nabla \mathbf{u}_{\rm S}$, and the convective product, $(\mathbf{u}_{\rm S} \cdot \nabla)\mathbf{u}_{\rm S}$, are also computed in the physical space (vertical arrows downwards, on the right). Finally, the physical product is projected onto the dual Fourier-Chebyshev space (bottom arrow, from right to left). The first stage of the algorithm is to evaluate the sum (2.17)

$$\mathbf{u}_{\rm S} = \sum_{l=-L}^{L} \sum_{n=-N}^{N} \sum_{m=0}^{M} a_{lnm}(t) \mathbf{\Phi}_{lnm}(r, \theta, z) = \sum_{l=-L}^{L} \sum_{n=-N}^{N} \sum_{m=0}^{M} a_{lnm} \; \mathrm{e}^{\mathrm{i}(n\theta + \mathrm{k}_o l z)} \mathbf{v}_{lnm}(r) \tag{2.65}$$

over the three-dimensional grid

$$(r_k, \theta_j, z_i) = \left(\cos(\frac{\pi k}{2M_d}) \; , \; \frac{2\pi}{N_d} j \; , \; \frac{\Lambda}{L_d} i \right), \tag{2.66}$$

for $k = 0, \ldots, M_d - 1$, $j = 0, \ldots, N_d - 1$ and $i = 0, \ldots, L_d - 1$. The values M_d, N_d and L_d are the numbers of radial, azimuthal and axial points, respectively, needed to *de-alias* the computation up to the spectral order of $\mathbf{u}_{\mathrm{S}}$. For coarse grid computations, the convolution sums which appear when evaluating the non-linear terms may generate low *aliased* modes [7]. A similar problem arises in the non-periodic (radial) direction, although in this case it is related to a poorly resolved quadrature. In this method, aliasing is removed by means of Orszag's $\frac{3}{2}-$rule, imposing

$$L_d \geq \frac{3}{2}(2L+1)\ , \quad N_d \geq \frac{3}{2}(2N+1)\ , \quad M_d \geq 3M, \tag{2.67}$$

in order to eliminate aliased modes up to order (L, N, M). Direct evaluation of (2.65) over each point of the grid (2.66) would require $O(LMN)$ operations. Overall, the total computation of $\mathbf{u}_{\mathrm{S}}$ would imply a total number of operations of order $O(L^2N^2M^2)$. Nevertheless, we can substantially reduce the number of operations by means of *Partial Summation* technique [4], where $\mathbf{u}_{\mathrm{S}}$ ($\mathbf{u}$ for simplicity) is evaluated over the radial grid r_k:

$$\mathbf{u}_k(\theta, z) = \mathbf{u}(r_k, \theta, z) = \sum_{l=-L}^{L} \sum_{n=-N}^{N} \mathrm{e}^{\mathrm{i}(n\theta + \mathrm{k}_o l z)} \underbrace{\sum_{m=0}^{M} a_{lnm} \mathbf{v}_{lnm}(r_k)}_{\alpha_{ln}^{(k)}}, \quad k \in [0, M_d - 1]. \tag{2.68}$$

The sum for the radial modes in (2.68) has been underbraced and identified by the coefficients $\alpha_{ln}^{(k)}$, that require $O(M^2LN)$ operations to be computed. The second step is the evaluation of $\mathbf{u}_k(\theta, z)$ over the azimuthal grid

$$\mathbf{u}_{jk}(z) = \mathbf{u}(r_k, \theta_j, z) = \sum_{l=-L}^{L} \mathrm{e}^{\mathrm{i}l\mathrm{k}_o z} \underbrace{\sum_{n=-N}^{N} \sum_{m=0}^{M} a_{lnm} \mathrm{e}^{\mathrm{i}n\theta_j} \mathbf{v}_{lnm}(r_k)}_{\beta_l^{(jk)}}, \quad (j,k) \in [0, N_d - 1] \times [0, M_d - 1], \tag{2.69}$$

taking advantage of the the pre-computed $\alpha_{ln}^{(k)}$ coefficients,

$$\beta_l^{(jk)} = \sum_{n=-N}^{N} \mathrm{e}^{\mathrm{i}n\theta_j} \sum_{m=0}^{M} a_{lnm} \mathbf{v}_{lnm}(r_k) = \sum_{n=-N}^{N} \mathrm{e}^{\mathrm{i}n\theta_j} \alpha_{ln}^{(k)}, \tag{2.70}$$

that requires $O(N^2ML)$ operations. Finally, $\mathbf{u}_{jk}(z)$ over the axial grid z_i is computed using the same procedure, i.e.,

$$\mathbf{u}_{ijk} = \mathbf{u}(r_k, \theta_j, z_i) = \sum_{l=-L}^{L} \mathrm{e}^{\mathrm{i}\mathrm{k}_o l z_i} \beta_l^{(jk)}, \quad (i,j,k) \in [0, L_d - 1] \times [0, N_d - 1] \times [0, M_d - 1]. \tag{2.71}$$

Overall, the computational cost needed for the previous three stages is $O\big(LNM(L + N + M)\big)$, and it can be further improved by using the FFT in z and FCT (*Fast Cosine Transform*) in r, leading to an optimal cost of $O\big(LNM \ln(LNM)\big)$ operations per time step.

Computation of $(\mathbf{u}_S \cdot \nabla)\mathbf{u}_S$ in the physical space is carried out by using standard Fourier Differentiation matrices [21] in the axial and azimuthal coordinates, whereas differentiation matrices $\mathbb{D}_r^{e;o}$ defined in (2.43-2.42) are used in the radial direction. Finally, partial summation techniques are used again to efficiently inverse-transform of $[(\mathbf{u}_S \cdot \nabla)\mathbf{u}_S]_{ijk}$ leading to the nonlinear term b_{lnm} appearing in (2.47).

2.6 Validation of the numerical scheme

2.6.1 Convergence analysis

The spatial convergence of the spectral Petrov-Galerkin method has already been tested in section §2.4 and also in Meseguer & Trefethen [43] via a linear asymptotic eigenvalue analysis, providing spectral accuracy in all cases studied. For the nonlinear unsteady computations, the same initial value problem has been solved by means of the two different linearly implicit schemes AB_2BD_2 and AB_4BD_4 . In both cases, the same spectral resolution in space, the same initial condition for the amplitudes and the same total integration time have been considered for consistency. In particular, the initial perturbation that we considered for our convergence tests is a two-dimensional streamwise independent field of the form

$$\mathbf{u}_S^0 = \mathbf{u}_{2D}^0 = \text{A}_{2D}\ \text{e}^{\text{i}\theta}\ \ (-\text{i}f_1(r), f_2(r), 0) + \text{c.c.}, \tag{2.72}$$

where $f_1(r) = 1-2r^2+r^4$, $f_2(r) = 1-6r^2+5r^4$, c.c. stands for complex conjugate and A_{2D} is a real constant such that $\varepsilon(\mathbf{u}_S^0) = \varepsilon_0$, where $\varepsilon(\mathbf{u})$ is the *normalised energy* of an arbitrary perturbation,

$$\varepsilon(\mathbf{u}) = \frac{1}{2\text{E}_{HP}} \int_0^\Lambda \text{d}z \int_0^{2\pi} \text{d}\theta \int_0^1 r\text{d}r\ \mathbf{u}^* \cdot \mathbf{u}, \tag{2.73}$$

with respect to the energy of the basic Hagen-Poiseuille flow, $\text{E}_{HP} = \pi\Lambda/6$. The initial condition (2.72) consists of a pair of streamwise vortices of azimuthal number $n = 1$ that only perturb the radial and the azimuthal components of the basic regime. This perturbation has streamwise invariance in time, due to its orthogonality with respect to the axial base flow. Thus, the initial condition ensures that $\mathbf{u}_S(t)$ preserves its streamwise symmetry for all t. In Fig. 2.5(a) we have plotted a $z-$cnst. cross section of the perturbation field $\mathbf{u}_S^0$, and the basic parabolic profile of the Hagen-Poiseuille flow has been represented in Fig. 2.5(b). Finite amplitude perturbations of the form (2.72) are of special interest in the nonlinear stability analysis of shear flows. Streamwise vortices are particularly efficient in triggering transition due to the usually termed *lift-up* effect, advecting slow axial

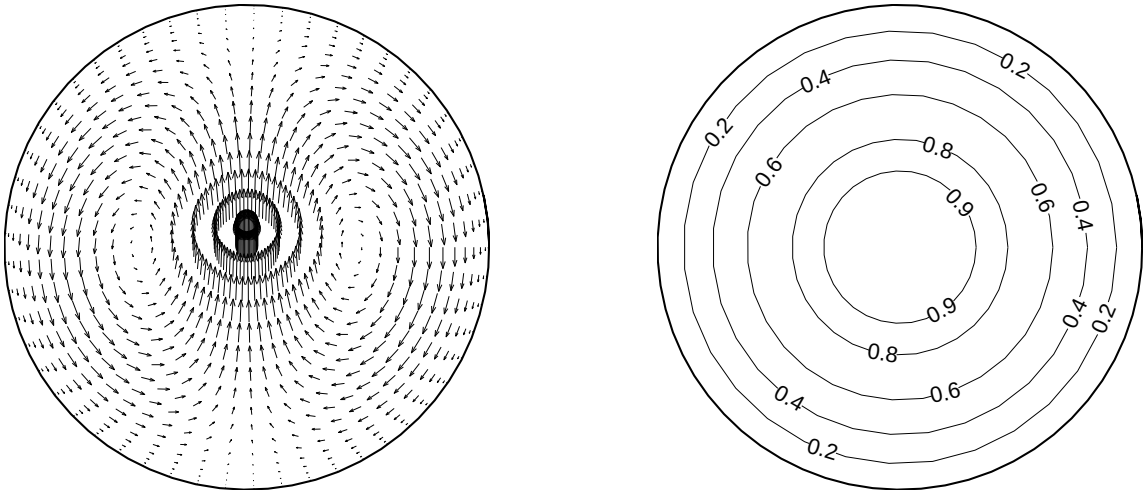

(a) (b)

Figure 2.5: (a) Initial perturbation field $\mathbf{u}_S^0$ prescribed by amplitudes given in (2.72). (b) Contour level curves of the axial speed corresponding to the parabolic Hagen-Poiseuille flow.

flow to high speed regions and viceversa [33, 57, 63, 81]. This mechanism modulates the axial parabolic flow in a new transient profile, usually termed *streak*, which contains saddle points, thus being potentially unstable with respect to three-dimensional infinitesimal disturbances [14, 15, 63].

As an example, Fig. 2.6 shows the evolution of the energy $\varepsilon(t)$ associated with the two-dimensional perturbation prescribed in equation (2.72) for $\mathrm{Re} = 3000$ and with initial energy $\varepsilon(\mathbf{u}_S^0) = \varepsilon_0 = \varepsilon(0) = 10^{-2}$. The structure of the modulated axial flow has been represented in Fig. 2.7 at some selected instants of time, labeled with white circles in Fig. 2.6. This run was carried out using $\mathrm{AB_4BD_4}$ with $M \times N = 25 \times 15$ radial×azimuthal modes (equivalent to $M_r \times N_\theta = 26 \times 31$ collocation points), with $\Delta t = 0.01$ and a total integration time $T = 200$. The evolution of this kind of perturbations was originally considered in Zikanov [81], where hybrid 2nd order finite differences scheme in r combined with a spectral Fourier method in θ was used. Low spatial resolution simulations based on the present spectral method were also provided in Meseguer [40]. In both cases the agreement with former computations is very good. In Fig. 2.7 it is clearly observed the formation of streaks. The first important feature of this transient flow is the presence of saddle points in its profile. The second is that this transient regime is almost steady, as we observe more clearly from the curve in Fig. 2.6.

A time-convergence test has been carried out by comparing the accuracy of the solution for the $\mathrm{AB_2BD_2}$ and $\mathrm{AB_4BD_4}$ schemes, always based on the same kind of perturbations

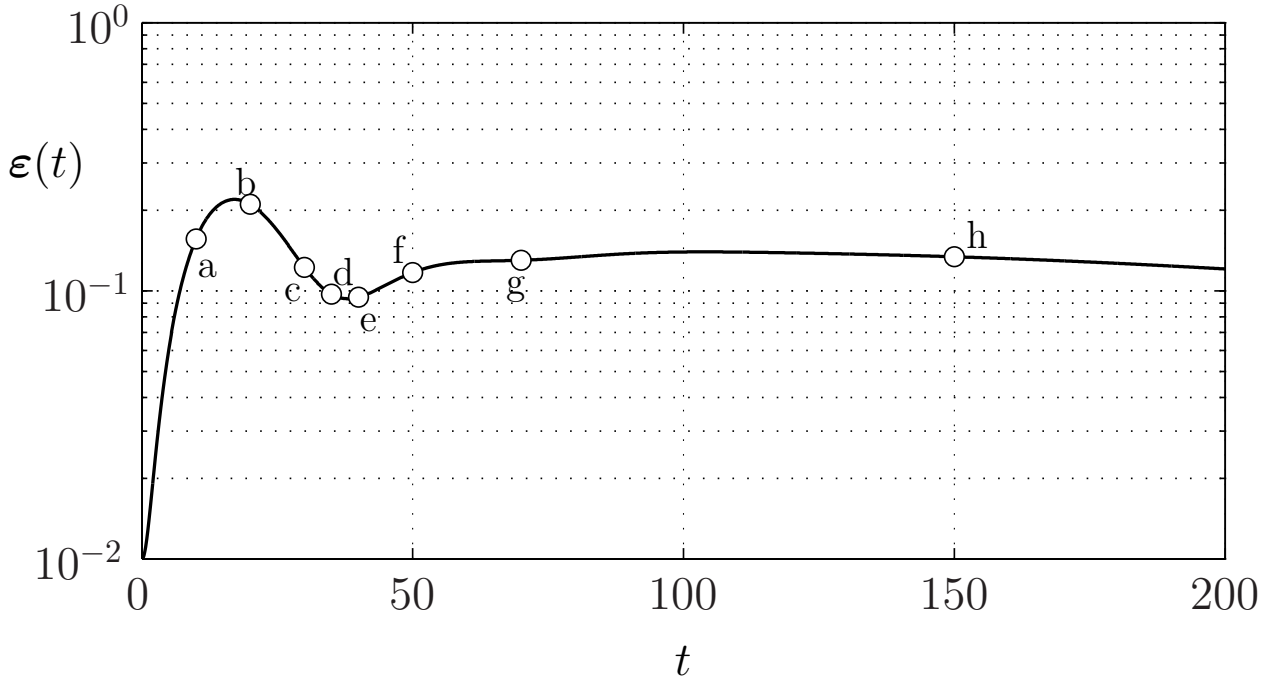

Figure 2.6: Typical evolution of the energy of a two-dimensional streamwise perturbation.

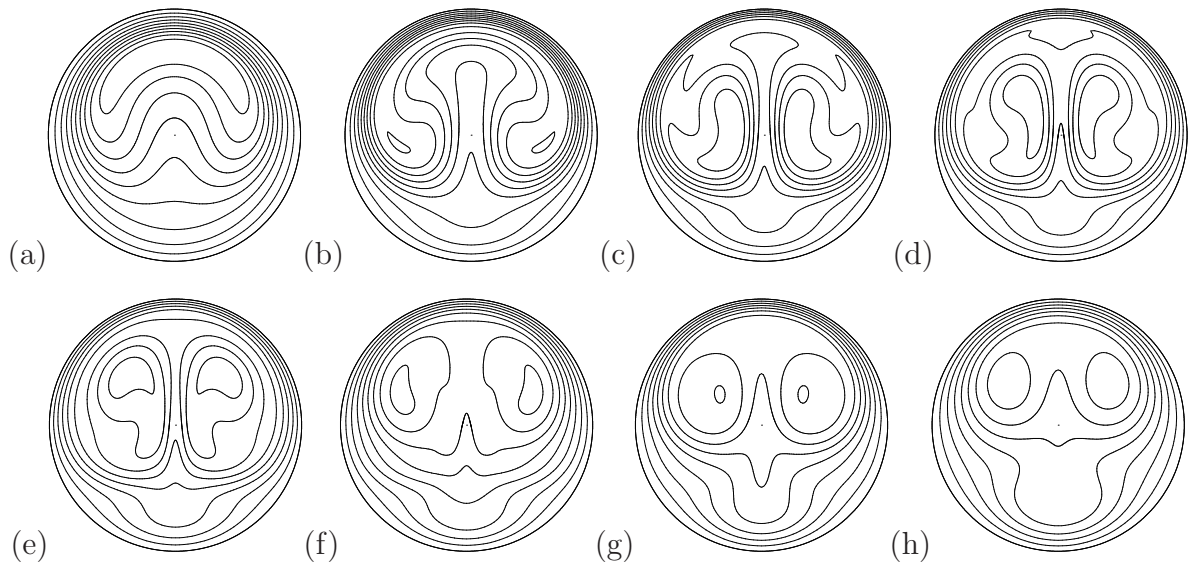

Figure 2.7: Modulated axial speed $(\mathbf{u}_\mathrm{S} + \mathbf{v}_\mathrm{B})_z$ contours corresponding to the time integration plotted in Fig. 2.6.

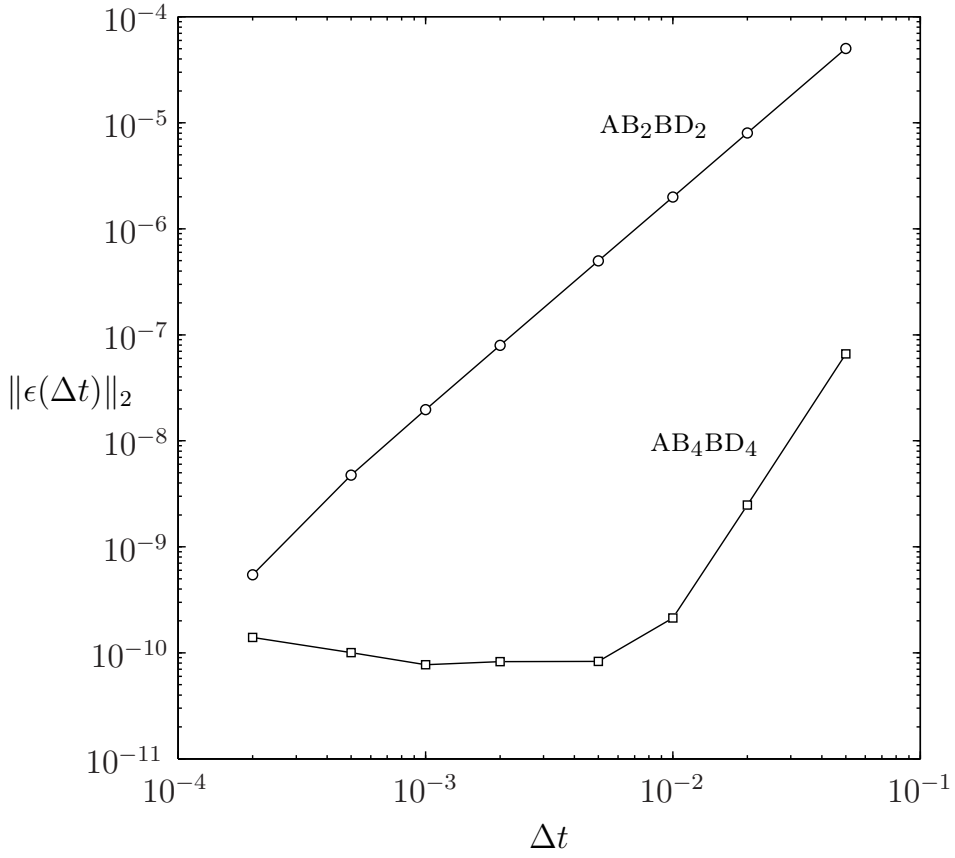

Figure 2.8: Absolute error (2.74) for the two different time marching schemes. The two curves represent the error obtained for the same initial value problem and with the same spatial resolution.

described before. All the runs have been based on the same initial condition (2.72), for Re = 2500, $M = 10$, $N = 10$ and a total time $T = 50$. Figure 2.8 captures the essential features of the convergence of the two different time marching schemes, representing the absolute L_2-norm error of the Fourier coefficients $a_{lnm}^{\Delta t}(T)$ obtained at the end of the run with respect to the *"exact"* ones, $a_{lnm}^{\Delta t_0}(T)$, obtained with a much smaller reference time step $\Delta t_0 = 10^{-4}$,

$$\|\epsilon(\Delta t)\|_2^2 = \sum_{l,n,m} \mid a_{lnm}^{\Delta t}(T) - a_{lnm}^{\Delta t_0}(T) \mid^2 . \tag{2.74}$$

Figure 2.8 reveals a faster (and better) convergence of the fourth order scheme in front of the second order one. In fact, for $\Delta t < 10^{-2}$, the AB_2BD_2 scheme is still converging with an absolute error of order 10^{-6}, whereas the AB_4BD_4 has already achieved the accuracy dictated by the spatial resolution. When using AB_2BD_2 , Δt should still be decreased nearly by two orders of magnitude to get that precision. The computational time required for every time

step is essentially the same for both schemes and this has been the main motivation to use the fourth order scheme in our computations. Nevertheless, AB_4BD_4 requires a bit more memory storage and this factor must be considered by the user.

As mentioned in the introduction, one of the novelties of the presented method is the use of half Gauss-Lobatto grid in the radial coordinate. The use of standard mappings, $x = 2r - 1$, identifying the radial domain $r \in [0, 1]$ with the cartesian interval $x \in [-1, 1]$ is a common practice in spectral methods in cylindrical coordinates [35, 46, 51, 62]. The clustering of quadrature points near the wall, i.e., $r = 1$ or $x = +1$ is justified by the presence of boundary layers and strong gradients of the physical variables in that region, being necessary to resolve the physical phenomena within those small scales. However, the accumulation of radial points near the center axis has no physical justification unless remarkable variations of the flow speed take place in a neighbourhood of the pole. This is not the case in the Hagen-Poiseuille problem, where the axial profile is smooth and exhibits a maximum at $r = 0$.

Wherever semi-implicit time marching schemes are used, the time step size Δt is conditioned by the *advective time scale*, $\tau_{max} = dh/c_{max}$, where d is a typical length scale of the problem, c_{max} is the advection speed and h is the grid size [4]. A straightforward geometrical analysis of the radial-azimuthal clustering in a standard collocation scheme $x = 2r - 1$ leads to

$$h \sim \frac{1}{M^2 N}, \tag{2.75}$$

where M is the number of radial points, clustered near the origin via the asymptotic behaviour of the Gauss-Lobatto distribution, $1-\cos(\pi/M) \sim \pi^2/2M^2$, and N is the number of azimuthal points, leading to an arclength clustering proportional to N^{-1}. Provided that the order of maximum speed of the flow is $O(c_{max}) \sim 1$ and the typical length of the problem is the nondimensional pipe radius, $O(d) = 1$, the advective restriction (2.75) leads to $\tau_{max} \sim O(N^{-1}M^{-2})$, whereas the asymptotic radial clustering given by (2.39) provides a milder accumulation ratio near the pole

$$r^+_{(M+3)/2} - r^+_{(M+1)/2} = -\cos\left(\frac{\pi(M+1)}{2M}\right) \sim \frac{\pi}{2M}, \tag{2.76}$$

leading to a less restrictive limit $\tau_{max} \sim O(N^{-1}M^{-1})$. The dependence $\Delta t_{max}(N, M)$ has been explored within the range $(N, M) \in [7, 19] \times [12, 28]$, for $Re = 2500$ and a total time of integration $T = 100$, starting with the same initial condition prescribed in (2.72). The maximum time step Δt_{max} has been plotted against M and N in figure 2.9. The behaviour of $\Delta t_{max}(N)$ for fixed M is the same as in other integration schemes (Fig. 2.9, right), whereas a remarkable improvement can be observed in Fig. 2.9, on the left, where

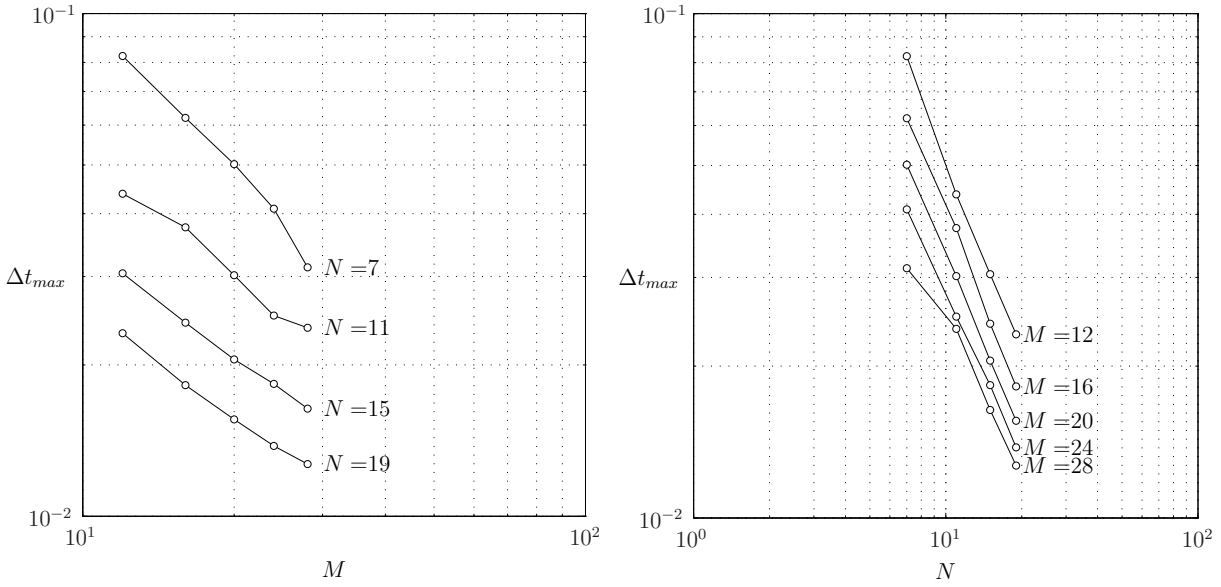

Figure 2.9: Δt_{max} as a function of the number of radial and azimuthal modes.

$\Delta t_{max}(M)$ for fixed N has been represented. Only two-dimensional perturbations have been included at $t = 0$, thus reducing the exploration to streamwise-independent dynamics. Although we have just focused our analysis on the radial-azimuthal clustering effect, the density of points in the axial coordinate will also affect the maximum time step size, the limitations being the same as in any other equispaced spectral scheme.

2.7 Transition to turbulence

This section is devoted to a performace analysis of the presented numerical solver in capturing the essential features of transitional pipe turbulence. The study of fully developed turbulence is out of the scope of the present work.

As mentioned in previous section, two-dimensional streaks might be destabilised by three-dimensional infinitesimal disturbances. This mechanism is just one possible scenario of transition to turbulence in shear flows and it is usually referred to as *streak breakdown* [40, 57, 63, 81]. In order to obtain a *streak breakdown*, three-dimensional disturbances of a suitable axial periodicity must be added to the two-dimensional perturbation. The new initial condition is:

$$\mathbf{u}^0_{\mathrm{S}} = \mathbf{u}^0_{\mathrm{2D}} + \mathbf{u}^0_{\mathrm{3D}}, \tag{2.77}$$

where $\mathbf{u}^0_{\mathrm{2D}}$ is the same perturbation described in (2.72), and $\mathbf{u}^0_{\mathrm{3D}}$ is a three-dimensional

disturbance of the form

$$\mathbf{u}_{3\mathrm{D}}^{0} = \sum_{l=5,6,7} \sum_{n=0,1} \mathrm{A}_{3\mathrm{D}}^{ln} \mathbf{v}_{ln} \; + \; \text{c.c.}, \tag{2.78}$$

where the fields $\mathbf{v}_{ln}$ are

$$\mathbf{v}_{ln} = \begin{cases} \mathrm{e}^{\mathrm{i}\mathrm{k}_o lz} \; (0, f_3(r), 0)\,, & (n=0) \\ \mathrm{e}^{\mathrm{i}(\mathrm{k}_o lz + n\theta)} \; (-\mathrm{i}n f_1(r), f_2(r), 0)\,, & (n=1) \end{cases} \tag{2.79}$$

with $f_3(r) = r(1-r^2)$. In this case, k_o must be suitably chosen so an optimal range of axial wave numbers $\mathrm{k}_l = l\,\mathrm{k}_o$ are initially activated. In previous works [40, 81], it has been proved that the optimal range of axial periodicities depends on the initial amplitude of the two-dimensional perturbation and the Reynolds number. A comprehensive exploration is not the aim of this analysis, so a particular case has been considered to test fully three-dimensional unsteady transitional dynamics. In particular, some axial wave numbers within the range $\mathrm{k} \in [1.5, 2.2]$ have been excited at $t = 0$. As in previous section, the bulk of the initial energy is mainly assigned to the two-dimensional component of the perturbation so that $\varepsilon_0^{2\mathrm{D}} \sim 10^{-3}$, whereas the amplitudes $\mathrm{A}_{3\mathrm{D}}^{ln}$, for $n = 0, \pm 1$ and $\mathrm{k}_{\pm 5,\pm 6,\pm 7} = 1.5625, 1.875, 2.1875$, are uniformly activated leading to a much smaller total three-dimensional energy $\varepsilon_0^{3\mathrm{D}} \sim 1 \cdot 10^{-7}$. This is accomplished by choosing $\mathrm{k}_o = 0.3125$ and $L = 16$, so that medium-long wavelengths dynamics are also captured, leading to a pipe length $\Lambda = 2\pi/\mathrm{k}_o \sim 20$. Overall, the computations reported here have been carried out with $L = 16$, $N = 16$ and $M = 32$, equivalent to a $M_r \times N_\theta \times L_z = 33 \times 33 \times 33$-radial $\times$ azimuthal $\times$ axial grid. The fixed length of the pipe and the number of axial modes fix the maximum axial wavenumber to $\mathrm{k}_{\max} = 5.0$. It is well known that high axial-azimuthal frequencies require a considerable number of radial modes to be resolved [56]. Nevertheless, transitional dynamics are strongly dominated by low or medium axial wavenumbers, the high frequencies being only important once fully developed turbulence has been established.

For $Re = 5012$, Fig. 2.10 shows a typical example of the evolution of the energies $\varepsilon^{2\mathrm{D}}(t)$ and $\varepsilon^{3\mathrm{D}}(t) = \varepsilon\left(\mathbf{u}_{3\mathrm{D}}(t)\right)$ associated with the two-dimensional and three-dimensional perturbations, respectively. The sudden exponential growth of $\varepsilon^{3\mathrm{D}}(t)$ is due to the inviscid instability. The computation shown in figure 2.10 covered $T = 600$ nondimensional time units, with a time step $\Delta t = 10^{-3}$ and using the $\mathrm{AB_4BD_4}$ scheme. The nearly $6 \cdot 10^5$ time steps required about 80 hours on a 3.0 GHz AMD Athlon CPU.

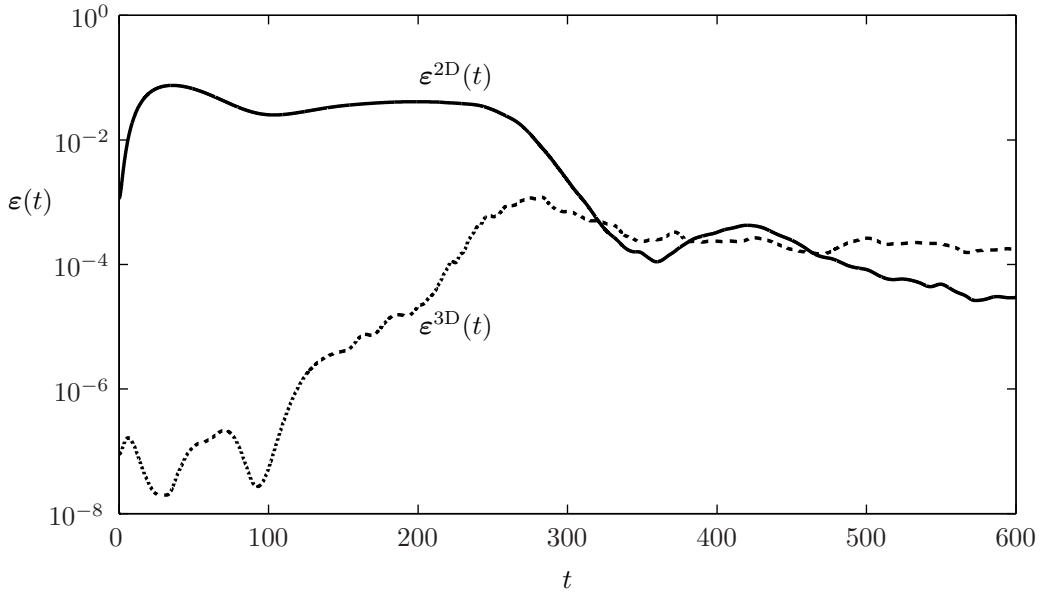

Figure 2.10: Energies $\varepsilon^{2D}(t)$ and $\varepsilon^{3D}(t)$ as a function of time, exhibiting the *streak breakdown* mechanism of transition to turbulence.

2.8 Conclusions

A solenoidal spectral Petrov-Galerkin formulation for the spatial discretisation of incompressible Navier-Stokes equations in unbounded cylindrical geometries has been formulated and implemented within a high order linearly implicit time marching scheme. The spatial discretisation identically satisfies the incompressibility condition and the pressure terms are eliminated in the projection. The solenoidal fields satisfy suitable regularity conditions at the pole and radial clustering is avoided by using half Gauss-Lobatto meshpoints and modified Chebyshev polynomials of selected parity, thus allowing fast transform in the radial coordinate. The resulting radial-azimuthal mesh leads to less restrictive explicit time marching conditions. For the efficient evaluation of the nonlinear term, dealiased partial summation techniques have been formulated. The spatial discretisation has been proven to converge spectrally in all linear cases studied. For unsteady nonlinear computations, modified AB_2BD_2 and AB_4BD_4 linearly implicit schemes have been used, the last proven to be more convenient for this particular problem. Different spatio-temporal convergence analysis have been provided and the time evolution of streamwise vortices has been studied as a test case. Streamwise streaks have been computed and their structure and energy distribution is almost identical to the ones formerly computed by other authors using different discretisation schemes. Transitional dynamics to turbulence has been computed by means of the usually termed streak breakdown scenario, and the streamwise dependent modes

that destabilise the streaks have axial periodicities within the interval predicted by former studies.

CHAPTER 3
TRANSITION FOLLOWING GLOBAL PERTURBATIONS

During the last decade, the pursuit of an answer to pipe flow transition has followed two independent research approaches. The first one has been mainly focused on the study of nonmodal transient growth exhibited by streamwise vortical finite amplitude perturbations, due to the strong nonnormality of the linearised Navier-Stokes operator, i.e., nonorthogonality of its eigenvectors [61, 40, 63, 62, 33]. This transient growth eventually stagnates, leaving an almost steady modulated streamwise flow that contains two-dimensional *streaks*, characterised by the presence of saddle points, potentially unstable with respect to three-dimensional infinitesimal perturbations in the *inviscid* stage, i.e., before the viscous effects take over the dynamics. Almost exponential growth of streamwise-dependent waves is therefore expected under the presence of streaks, eventually inducing transition via a mechanism commonly termed *streak breakdown*, by which the three-dimensional waves break the streamwise structure of the streaks, leading to turbulence. The described instability process has been proved to be a universal mechanism of subcritical transition in other shear flows such as Blasius boundary layer or plane Poiseuille flow, although other scenarios may also be at work in the transition process [57, 8].

The second approach to the problem of subcritical transition, which we will explore later on, has been based on the direct exploration of the phase map of the corresponding dynamical system representing the fluid problem. Subcritical transition in linearly stable open shear flows is directly related to the existence of secondary solutions of the Navier-Stokes equations. Since these flows are linearly stable for all Reynolds numbers, these other solutions must be necessarily disconnected from the basic flow. For example, in plane Couette flow, secondary solutions were found [47, 9] by means of homotopy transformations. More recent numerical studies [64, 1] have also reported new solutions for this particular problem. In pipe flow, recent numerical studies have revealed the existence of travelling wave solutions of selected azimuthal symmetry, supposedly constituting the essential topological feature of the chaotic dynamics [19, 78]. The limit cycles associated with these travelling waves have been proved to be linearly unstable [18]. The computation of the friction factor associated to these time-dependent solutions ostensibly matches the empirical laws describing turbulent flows in smooth pipes [19], which in itself constitutes a clear signature of the relevance of these solutions in the turbulent regime.

One of the main goals of the two previously described approaches to subcritical turbulence has been to provide a characterisation of the *basin of attraction* of the basic laminar flow. We must think of it as a subset in an infinite dimensional space that contains the

basic flow, driving towards this solution any initial perturbation contained in this subset. Numerical simulations confirm that pipe flow is even stable for *all* axisymmetric finite-amplitude disturbances [52]. Therefore, the basin of attraction *is not* a bounded domain and its *size* is a meaningless measure because it is actually infinite. Instead, we must think of the boundary of that basin of attraction that approaches a minimum amplitude A_c from the steady solution. A question still unsolved is the dependence of this amplitude with the Reynolds number, $A_c = A_c(Re)$, that must necessarily decrease when Re is increased, being plausible to assume that its asymptotic behaviour scales with Re according to

$$A_c \sim Re^{\gamma}, \tag{3.1}$$

with γ necessarily negative. In other words, A_c represents the minimum amplitude of a perturbation capable of destabilising the basic profile, leading to a turbulent regime. Theoretical exponents for plane channel flows have been obtained by means of asymptotic methods within the framework of some particular transition scenarios [8]. For pipe flow, recent renormalisations [71] have been suggested in order to cast different experimental results in terms of a single definition of the amplitude appearing in (3.1), providing lower and upper bounds for the value of this critical exponent that presumably lies within the interval $\gamma \in [-9/5, -6/5]$.

The most comprehensive experimental explorations of the threshold amplitude problem (3.1) for pipe flow were provided by Darbyshire & Mullin [11] and more recently by Hof *et al.* [27], henceforth referred as HJM, where the fluid was perturbed by means of localised injections of selected azimuthal symmetry. The experimental results of HJM clearly concluded that the minimum amplitude of a perturbation required to trigger transition scaled as the inverse of the Reynolds number, i.e., $A_c = \mathcal{O}(Re^{-1})$. Postprocessed experimental results have recently confirmed the presence of the aforementioned travelling waves obtained computationally [19, 78] as inherent components of the turbulent flow [26].

As far as we know, the first computational estimation of the threshold exponent problem (3.1) in pipe flow was provided in Meseguer [40], employing a numerical model for time integrations that were too short in time, thus being impossible to distinguish between relaminarised and turbulent flows, particularly for low Re. The resolution was extremely poor, especially in the axial direction, for which a singe mode was considered, not allowing for nonlinear interaction. By contrast, the present study provides a highly resolved comprehensive numerical exploration of the threshold amplitude for $2.5 \times 10^3 < Re < 1.26 \times 10^4$, based on the streak breakdown scenario, for medium length pipe aspect ratio and for extended time-horizons that allow to distinguish between long-lasting turbulence and relaminarisation. Streamwise perturbations consisting of a varying number of pairs of vortices

are used as initial disturbances, optimal streamwise-dependent waves and random noise are alternatively added as the 3D component of the perturbation, the development of the flow is carefully analised for some test cases and the independence of the considered transition scenario with respect to pipe length suitably verified.

This chapter is structured as follows. Section §3.1 is devoted to the mathematical formulation of the initial value problem for the perturbation fields, and the axial and azimuthal structure of disturbances is presented. The criteria that allow to classify laminar, relaminarised and turbulent flows are explained in section §3.2, where the time horizons required to distinguish among those regimes are provided. Section §3.3 yields the main results of the exploration for different types of streamwise disturbances and also investigates the effects of pipe length in this particular transition scenario. Finally, many questions regarding the difficulties of comparing numerics with recent experimental results are addressed. The main conclusions are gathered and presented in section §3.4.

3.1 The initial value problem

Following the formulation in section 2.1, the computational domain considered is $(r, \theta, z) \in \mathfrak{D} = [0, 1] \times [0, 2\pi] \times [0, \Lambda]$, where the dimensionless pipe-length in radii units is fixed to $\Lambda = 6.4\pi \sim 20$ (except for a subset of runs on a much longer pipe, with $\Lambda = 32\pi \sim 100$, carried out for verification purposes). For a vast exploration, the spatial resolution used in the domain $\mathfrak{D}$ is $M_r \times N_\theta \times L_z = 25 \times 33 \times 33$ radial×azimuthal×axial grid points, and $M_r \times N_\theta \times L_z = 33 \times 33 \times 33$ for further refinements, resulting in a dynamical system of nearly 3.5×10^4 degrees of freedom. No substantial differences have been observed when increasing the spatial resolution or decreasing the time step. The spatial convergence has been checked by repeating some test computations on a finer mesh of $M_r \times N_\theta \times L_z = 41 \times 49 \times 49$. Also the energy contents of the highest axial/azimuthal fourier modes has been monitored for every single run to ensure the adequacy of the spatial truncation. For subcritical runs, an energy decay of 6 to 7 orders of magnitude below that of the basic flow has been considered enough. Transitional runs are clearly under-resolved when turbulent motion begins. The computational costs of the resolution that would be required are unaffordable, but it must be bore in mind that it is not the aim of this study to simulate turbulence, but to bound the basin of attraction of the basic flow. Computations on a longer pipe have been carried out in order to check the length effects in the transition mechanisms studied. In particular, computations with $\Lambda = 32\pi \sim 100$ have been done by increasing the grid size to $M_r \times N_\theta \times L_z = 33 \times 33 \times 129$.

The *normalised energy* of a perturbation $\mathbf{u}$ is measured by means of the volume integral or hermitic product

$$\varepsilon(\mathbf{u}) = \frac{1}{2\mathrm{E_{HP}}} \int_{\mathfrak{D}} \mathbf{u}^{\dagger} \cdot \mathbf{u} \, \mathrm{d}\mathfrak{D}, \tag{3.2}$$

with respect to the energy of the basic Hagen-Poiseuille flow, $\mathrm{E_{HP}} = \pi\Lambda/6$, so that the *amplitude* of the perturbation is defined as the square root of its normalised energy,

$$A(\mathbf{u}) = \sqrt{\varepsilon(\mathbf{u})} \, . \tag{3.3}$$

To better understand how the energy is distributed within the flow, it is very convenient to express the perturbed velocity $\mathbf{v}$ as a sum of the basic flow $\mathbf{u}_{\mathrm{b}}$ and the Fourier components of the perturbation field $\mathbf{u}$, satisfying (2.11,2.12) and (2.14,2.15),

$$\mathbf{v}(r,\theta,z,t) = \mathbf{u}_{\mathrm{b}}(r) + \mathbf{u}_{00}(r,t) + \overbrace{\sum_{n\neq 0} \mathrm{e}^{\mathrm{i}n\theta} \mathbf{u}_{0n}(r,t)}^{\mathbf{u}_{2\mathrm{D}}(r,\theta,t)} + \overbrace{\sum_{l\neq 0} \sum_{n} \mathrm{e}^{\mathrm{i}(n\theta + \frac{2\pi}{\Lambda} lz)} \mathbf{u}_{ln}(r,t)}^{\mathbf{u}_{3\mathrm{D}}(r,\theta,z,t)}, \tag{3.4}$$

where $\mathbf{u}_{00}$ contains the azimuthal-axial-averaged perturbation velocity profile, $\mathbf{u}_{2\mathrm{D}}$ represents the non-axisymmetric streamwise component of the velocity field and $\mathbf{u}_{3\mathrm{D}}$ the remaining streamwise-dependent components. For the particular computations presented throughout this study, $\mathbf{u}_{2\mathrm{D}}$ must be interpreted as the streaks modulation of the flow.

Using (3.2) on the decomposed velocity field, the energies corresponding to the bulk flow, to the streamwise component and to the 3D perturbation can be computed independently as $\varepsilon_{00} = \varepsilon(\mathbf{u}_{00})$, $\varepsilon^{2\mathrm{D}} = \varepsilon(\mathbf{u}_{2\mathrm{D}})$ and $\varepsilon^{3\mathrm{D}} = \varepsilon(\mathbf{u}_{3\mathrm{D}})$, respectively.

Subcritical instability in shear flows is efficiently triggered by adding streamwise vortical perturbations to the basic flow [33, 61, 57, 8]. Of all possible initial disturbances, streamwise vortices with azimuthal wave number $n_{\mathrm{v}} = 1$ are the best candidates to trigger transition, as several linear nonmodal stability analyses of pipe flow [62, 45] have repeatedly shown that this sort of disturbances exhibit optimal transient growth. This energy growth leads to the generation of strong nonlinear streaks, in the presence of which streamwise-dependent modes of selected axial periodicity are destabilised. Time-dependent linear stability analysis of the streamwise streaks [81] confirms that only a subset of streamwise-dependent modes are potentially destabilised by the inflectional transitional streaks. Therefore, the perturbation introduced at $t = 0$ must satisfy three requirements to be *optimal*. First, it must have a strong streamwise component to generate inflectional profiles or streaks. Second, it must also contain small streamwise-dependent components of suitable axial periodicity within the range that exhibits optimal inflectional instability [81]. Third, since the streaks are transient modulations of the basic flow, the destabilised streamwise-dependent

components have a limited period of time to grow and non-linearly interact with the modulated flow while it lasts. As a result, although the streamwise-dependent initial amplitudes can be of much smaller magnitude than that of the streamwise component, they still need to be large enough to be able to break the streaks before the onset of their viscous decay.

Even though a single pair of streamwise vortices ($n_{\rm v} = 1$, from here on referred to as N_1) experiences the largest transient growth [62, 45], perturbations consisting of a greater number of pairs of streamwise vortices ($n_{\rm v} = 2, 3...$, which we will call N_2, N_3..., respectively), although exhibiting smaller transient growth, might develop into streaks with a higher potential of destabilising streamwise-dependent waves.

The initial disturbance $\mathbf{u}_0 = \mathbf{u}(r, \theta, z, 0)$ used in a first exploration of the critical threshold consists of a suitable superposition of a single pair of two-dimensional streamwise vortices (N_1), $\mathbf{u}_0^{\rm 2D}$, and a set of three-dimensional waves, $\mathbf{u}_0^{\rm 3D}$, of selected axial periodicities,

$$\mathbf{u}_0 = \overbrace{\mathrm{C}^{\rm 2D}\ \mathrm{e}^{\mathrm{i}\theta}\mathbf{v}_1(r)}^{\mathbf{u}_0^{\rm 2D}} + \overbrace{\sum_{l,n} \mathrm{C}_{ln}^{\rm 3D}\ \mathrm{e}^{\mathrm{i}(n\theta + \mathrm{k}_o l z)}\mathbf{v}_n(r)}^{\mathbf{u}_0^{\rm 3D}} + \text{c.c.}, \tag{3.5}$$

where c.c. stands for complex conjugated terms. The radial structure of $\mathbf{u}_0^{\rm 2D}$ takes the simplest polynomial form compatible with solenoidality and non-slip boundary conditions at the wall, closely resembling a nearly optimal (in its capability of generating strong streaks) pair of streamwise vortices [62, 81]. As to $\mathbf{u}_0^{\rm 3D}$ in (3.5), the sum only excites streamwise dependent modes with $n = \{-1, 0, 1\}$ and $l = \{l_1, l_2, l_3\}$ (i.e. 9 streamwise modes overall) and whose radial structure is also of the lowest polynomial order. The radial fields just described are:

$$\mathbf{v}_j(r) = \begin{cases} r(1-r^2)\ \hat{\boldsymbol{\theta}} & j = 0 \\ -\mathrm{i}\ j\ r^{\sigma-1}(1-r^2)^2\ \hat{\mathbf{r}} + \mathrm{D}[r^\sigma(1-r^2)^2]\ \hat{\boldsymbol{\theta}} & j \neq 0, \end{cases} \tag{3.6}$$

where $\sigma = 1$ (2) for j odd (even) and D denotes a radial derivative. The subscript j alternatively equals 1 for the 2D component or represents n for the 3D component of the perturbation given in (3.5).

The fundamental axial wavenumber $\mathrm{k}_o = 2\pi/\Lambda$ appearing in (3.5) is determined by the aspect ratio of the computational pipe domain. The triad l_i, for $i = 1, 2, 3$, must then be chosen so that the excited axial wave-numbers ($\mathrm{k}_i = \mathrm{k}_o l_i$) lie within the range exhibiting optimal exponential growth of $\mathbf{u}^{\rm 3D}$ in the presence of the streaks developing from $\mathbf{u}_0^{\rm 2D}$. According to former studies [81, 40] and a few preliminary runs within the frame of the present work, the optimal axial wave-number appears to be somewhere in the interval

$\mathrm{k}_{\mathrm{opt}} \in [1.5, 2.2]$. Since the aspect ratio of the pipe has been fixed to $\Lambda \sim 20$ radii, the triad $l_i = \{6, 7, 8\}$, which activates waves with $\mathrm{k}_i = \{1.56, 1.88, 2.19\}$, must be initially excited.

The complex constants C^{2D} and $\mathrm{C}^{\mathrm{3D}}_{ln}$ in (3.5), which modulate the initial amplitude of the two components of the perturbation, are chosen so that the initial energy of the streamwise vortices, $\varepsilon(\mathbf{u}_0^{\mathrm{2D}})$, and of the three-dimensional waves, $\varepsilon(\mathbf{u}_0^{\mathrm{3D}})$, take the desired values $\varepsilon_0^{\mathrm{2D}}$ and $\varepsilon_0^{\mathrm{3D}}$, respectively. $\varepsilon_0^{\mathrm{3D}}$ is evenly distributed among the whole set of excited 3D modes. The complex phases of these constants are generated randomly.

With the aim of testing vortical perturbations of different azimuthal topology, a slightly different type of initial condition has been defined. The 2D component in (3.5) has been adapted in (3.7) to admit varying azimuthal wave-numbers (n_{v}) in order to represent streamwise-independent structures consisting of an arbitrary number of pairs of vortices. The simplest polynomial form, detailed in (3.6), has been retained, with j now representing n_{v}. Thus, vortical structures with $n_{\mathrm{v}} = 2, 3$ (N_2, N_3) can be considered along with the aforementioned single pair of vortices ($n_{\mathrm{v}} = 1$, N_1). No studies exist, to the authors knowledge, on the optimal range of axial-wavenumbers (k) of the waves that are most destabilised in the presence of streaks developing from N_2 and N_3 vortical structures. Consequently, rather than undertaking such a vast task as would be determining the optimal axial wave-numbers, decision has been made of simply adding a random 3D noise, which in fact narrowly mirrors what happens in experiments, thus exciting 3D waves of all axial wave-lengths. The exploration for a single pair of vortices (N_1) has been repeated with this random 3D noise for checking purposes. The general expression of the initial disturbance for this enhanced parameter exploration is

$$\mathbf{u}_0 = \overbrace{\mathrm{C}^{\mathrm{2D}}\, \mathrm{e}^{\mathrm{i}n_v\theta}\mathbf{v}_{n_{\mathrm{v}}}(r)}^{\mathbf{u}_0^{\mathrm{2D}}} + \overbrace{\mathbf{u}_{\mathrm{rand}}(r,\theta,z)}^{\mathbf{u}_0^{\mathrm{3D}}} + \mathrm{c.c.}, \tag{3.7}$$

with $\mathbf{u}_{\mathrm{rand}}$ a random perturbation velocity field of the desired amplitude, containing much lower energy than the streamwise component.

3.2 Criteria for transition

In order to establish criteria to decide whether the perturbations (3.5) and (3.7) lead to turbulence or not, it is crucial to run up to a *time-horizon* at which the streaks have fully developed and the three-dimensional perturbations have had enough time to grow. This time has been found to be at least $T_{\max} = 1000$ advective time units for the lowest $\varepsilon^{\mathrm{2D}}$ at the highest *Re* explored. After this period, either the streak breakdown or the irreversible onset

of viscous decay have taken place. However, for $Re < 7500$, $T_{\min} = 600$ has been found to be enough. Experimentally, considering the perturbation is at worst advected downstream at the basic flow maximum axial speed, this is equivalent to having the observation point at 300 to 500 diameters distance downstream from the perturbation point. The longest constant mass flow rig used in experiments allows to make observations up to 530 diameters downstream from the perturbation location [27], which our time-horizons represent well enough. Checking for turbulence after this time is therefore a reasonable approach, and this is done by a bare eye inspection of the modal energy distribution. In the present study, a simulation run is considered *turbulent* if

$$\varepsilon^{3\mathrm{D}}(T) \geq 10^{-3} \text{ and } \mathcal{O}\left(\varepsilon^{2\mathrm{D}}(T)\right) \sim \mathcal{O}\left(\varepsilon^{3\mathrm{D}}(T)\right), \tag{3.8}$$

otherwise *laminar*. Condition (3.8) is based on the fact that three-dimensionality is a clear signature of turbulent dynamics and therefore it is required for the streamwise-dependent modes to be still active, and much stronger than initially, at the end of the run. For low Re, however, transition for a limited time-window with an eventual relaminarisation has been consistently observed. These *relaminarised* runs would have appeared as turbulent depending on the position of the observation area in an experimental rig. The existence of this phenomenon suggests that some of the runs considered turbulent within a time-horizon of $T = 600$ may have relaminarised if longer runs had been envisaged. It is however important to point out that we do not expect to properly model developed turbulence with our discretisation, as it is too coarse to represent the smallest turbulent scales at which the energy is dissipated. Turbulence and relaminarisation are therefore missrepresented phenomena in the current work, and should be interpreted with extreme care. Figures 3.1a, 3.1b and 3.1c illustrate a laminar, a turbulent and a relaminarised run, respectively. They all depict the evolution of N_1-type disturbances and the selected set of optimal 3D waves. In each plot, the continuous line corresponds to the energy of the mode excited by the streamwise perturbation, which constitutes a reliable signature of the development of the streaks. The dashed lines are the energies associated with some of the streamwise-dependent modes of the axial triads with $n = 0$ or $|n| = 1$. In the laminar case, Fig. 3.1a, the three-dimensional components of the perturbation are only temporarily excited once the streaks have developed, but this tendency is soon reverted and their energy rapidly decays before having been able to perturb the streamwise streaks. The turbulent run, Fig. 3.1b, differs from the laminar one in the growth rate of the streamwise dependent modes in the presence of the streaks, eventually leading to a streak breakdown and setting off chaotic dynamics or turbulent motion. This phenomenon can be spotted by looking at the drastic fall of $\varepsilon^{2\mathrm{D}}(t)$ for $t > 50$. Since the inflectional structure of the modulated flow is streamwise independent, this transition scenario leads to *global* turbulence instead of *intermittency* phenomena ob-

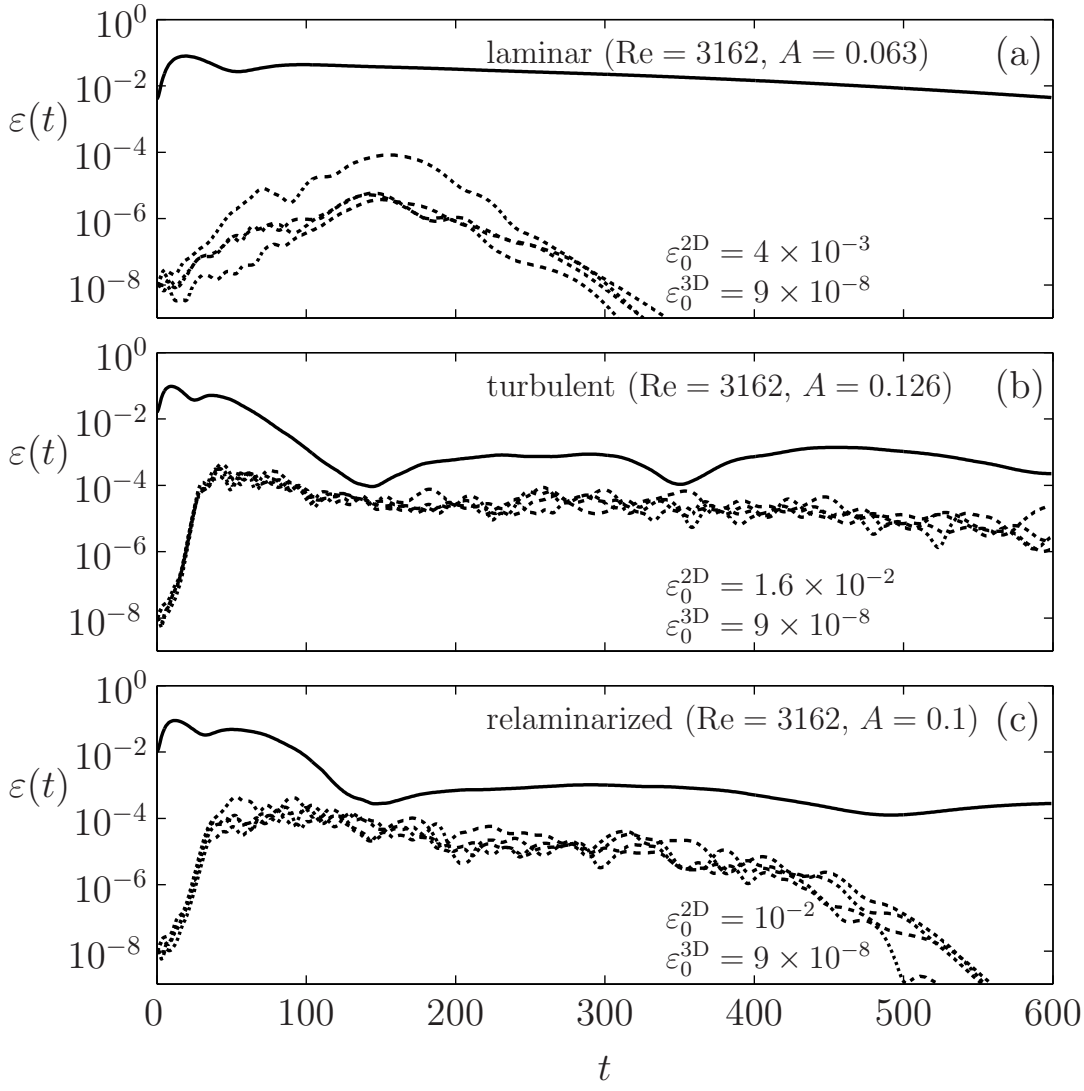

Figure 3.1: From top to bottom, a) laminar, b) turbulent and c) relaminarised runs. In all three plots, the continuous line represents $\varepsilon^{2D}(t)$, and the dotted lines are the energies associated with the streamwise-dependent triads.

served in the experiments, where coexistence of laminar flow with turbulent regions, usually called *puffs* and *slugs*, is observed. Finally, in the relaminarised run, Fig. 3.1c, the turbulent motion is abruptly interrupted and the streamwise-dependent energies start decaying rapidly whilst the streaks recover temporarily to slowly vanish afterwards for $t > 600$.

3.3 Results and discussion

For the present study, we have carried out a comprehensive exploration of the minimum initial amplitude, $A_0 = A(\mathbf{u}_0)$, defined in (3.3) required to trigger transition, according to the criteria established in section §3.2. This has initially been done for disturbances fulfilling all optimality criteria derived from previous studies, i.e., a single pair of streamwise vortices, N_1, plus the 3D waves that are most unstable to the streaks developed from these vortices, detailed in (3.5).

The current exploration has been extended for disturbances consisting of different numbers of pairs of vortices (N_2 and N_3), on top of which random 3D noise has been added according to (3.7), since no available data on the optimal axial periodicity of 3D waves destabilised by streaks developing from these vortices is available in the literature. The critical threshold exploration for N_1 disturbances has been repeated with random 3D noise to allow comparison with the previous exploration only considering activation of the optimal 3D waves, and to indeed assess their optimality. Finally, the critical amplitude threshold for the N_1 type of initial condition exciting the optimal 3D waves has been recomputed on a much longer pipe in order to rule out length scale effects on transition for the particular scenario investigated. An extra run on the long pipe with random 3D noise added on top of an N_1 vortical disturbance has been computed to illustrate the streak breakdown global mechanism of transition by comparing the same case on the short pipe.

3.3.1 N_1 disturbances with optimal 3D waves

The critical amplitude threshold exploration for this particular kind of disturbances covers a wide range of Reynolds numbers, within the interval $Re \in [2.5\times10^3, 1.26\times10^4]$, and initial energies $\varepsilon_0^{2\mathrm{D}}$ within the range $\varepsilon_0^{2\mathrm{D}} \in [2.5\times10^{-5}, 4\times10^{-2}]$, while the energy associated with the streamwise-dependent modes is held constant, with $\varepsilon_0^{3\mathrm{D}} = 9\times10^{-8}$ evenly distributed among the corresponding triads.

Results for the coarse computations ($M_r \times N_\theta \times L_z = 24 \times 33 \times 33$), are shown in

Fig. 3.2a, where white triangles represent laminar runs, black circles denote turbulent runs and empty circles correspond to relaminarised runs. The *critical* amplitudes, obtained from a refined exploration ($M_r \times N_\theta \times L_z = 33 \times 33 \times 33$), have been marked with gray squares. Overall, the over two hundred exploratory runs required nearly 10 CPU months on a 3 GHz Athlon-PC cluster.

For low Reynolds numbers, it is remarkable how relaminarisation is a very common phenomenon, where the basic flow preserves sound stability properties and considerably big perturbations are required to trigger transition. As expected, the critical amplitude A_c is a decreasing function of the Reynolds number. In fact, A_c exhibits a vertical threshold evidenced by the behaviour of the slope, which is very pronounced at low Re (allegedly converging to a vertical asymptote at $Re_{cr} \lesssim 2000$).

As soon as Re is increased, the numerical results shown in Fig. 3.2a clearly suggest that pipe Poiseuille flow follows the same behaviour as other shear flows [8, 57], with a critical amplitude that decreases with Re according to $A_c \sim Re^{-1.47\pm0.02}$, very close to the exponent $\gamma = -3/2$ quoted in previous numerical studies with far less resolution and run on a much shorter domain [40] (dashed straight line in Fig. 3.2), at least within the studied range. This behaviour has been confirmed by increasing the spectral resolution of the numerical scheme. Furthermore, the axial/azimuthal resolutions have been validated as sufficient by assessing the decay of the energy contents of the highest Fourier modes for the subcritical runs, which has been required to be 6 to 7 orders of magnitude below that of the basic flow. The resolution is certainly not sufficient for runs exhibiting transition once turbulence sets in. However, since this work is only concerned with bounding the basin of attraction of the basic flow, properly representing the laminar phases of the transition process is enough. The uncertainty on the exponent γ has been assessed by estimating the evolution of the slope of the critical threshold through linear regressions on subsets of contiguous data points and by assessing the variability of this slope around the average value at which it seems to stabilise at high Reynolds. Fig. 3.2b shows a zoom on the squared out region in Fig. 3.2a, including the higher resolved integrations that have been used to accurately determine the threshold amplitude.

The experimental results recently reported in HJM revealed a clear exponent $\gamma = -1$. The numerical simulations presented here are not necessarily in contradiction with the experiments. In fact, expression (3.1) implicitly involves many physical aspects that require an accurate description before making any comparison between numerics and experiments. First, the mathematical definition of the amplitude A appearing in (3.3) was provided in terms of the kinetic energy of the perturbation, whereas HJM measured the amplitude A as a

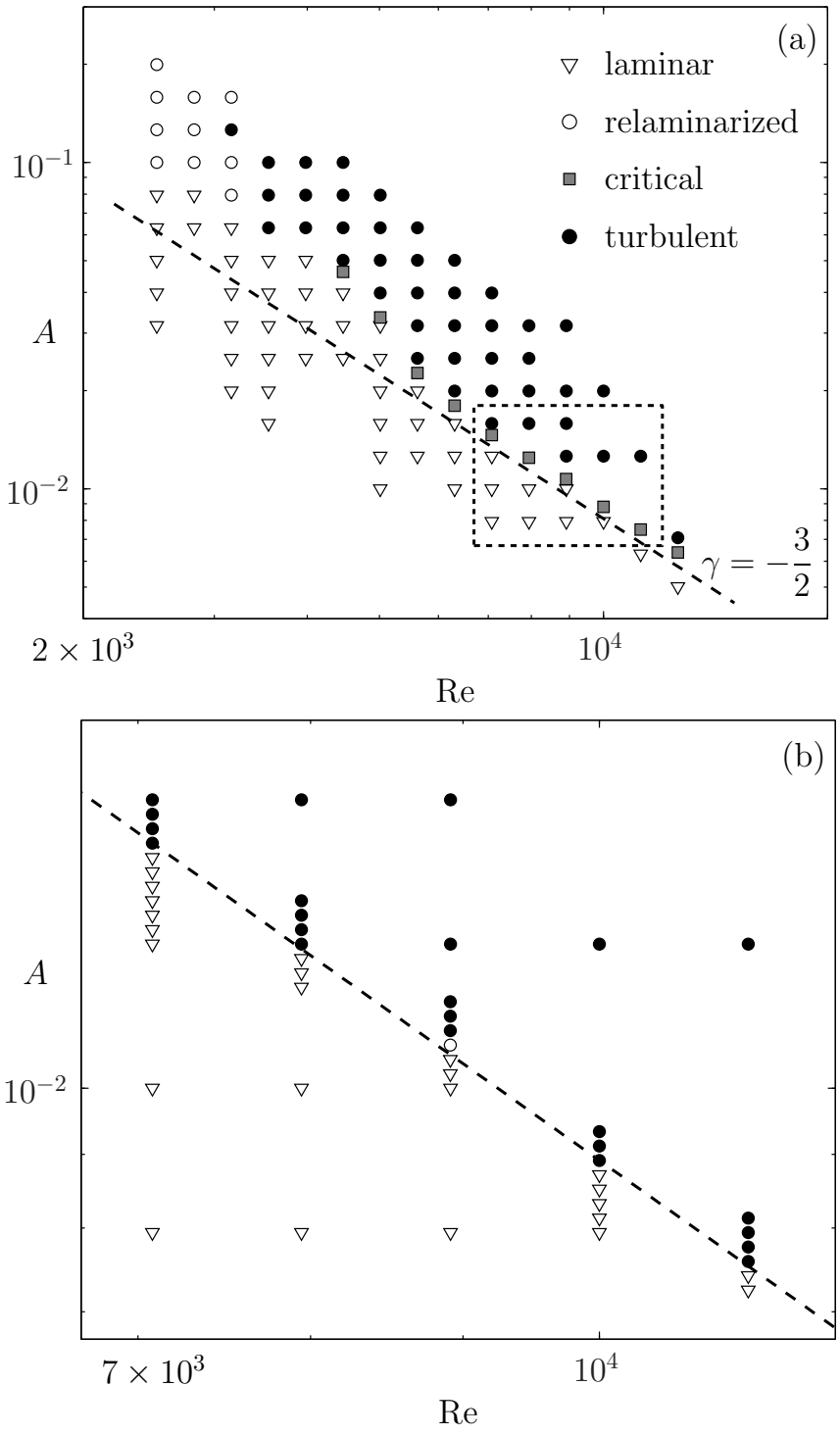

Figure 3.2: Threshold amplitude for N_1-type perturbations with optimal 3D waves. a) Coarse exploration with lower spectral resolution $M_r \times N_\theta \times L_z = 24 \times 33 \times 33$. b) Zoomed region on top, showing the numerical refinements for $M_r \times N_\theta \times L_z = 33 \times 33 \times 33$. Overall, the 200 runs presented here required nearly 10 CPU months on a 3.0 GHz Athlon PC-Cluster.

ratio between the perturbing injected flux and the basic mean flux, i.e., $A \sim \Phi_{\text{inj}}/\Phi_{\text{HPF}}$. Second, the geometrical features of the perturbation will necessarily conditionate the subspace over which we are measuring the amplitude appearing in (3.1). In the present scenario, we have selected streamwise-independent disturbances that optimally trigger inflectional instability, whereas in the experiments, the disturbances are axially localised, thus exciting the full spectrum of streamwise wavenumbers. Besides, the azimuthal symmetry of the numerical perturbation is $n_{\text{v}} = 1$, in contrast with the six-jet device used in HJM that forces an $n_{\text{v}} = 6$ symmetry. Third, our perturbation mechanism is mathematically posed as an *initial value problem*, whereas the injections used in HJM require finite durations, thus transiently modifying the original topological features of the basin of attraction. Finally, expression (3.1) is only valid for high values of *Re*. Thus, over the range studied both in experiments and numerics the exponent obtained must necessarily be *local*. This would also be in line with results obtained for plane Poiseuille flow [8], where full simulations at low *Re* also give different exponents that are ascribed to *finite-Re* effects. Further increase of the Reynolds number would be required to asymptotically confirm the value of γ.

The observed discrepancies with experiments should not be taken as a major hindrance. We are concerned with natural transition due to unknown perturbation sources that are always present in the flow. The aim of this study is to identify the components of this unknown sources that can be held responsible for transition and, to that end, numerical simulation is much more flexible than experiments. We are quite confident, however, that experimental disturbances containing strong components of the numerically used ones are realisable and that they will very much yield the same results as our numerical experiments.

3.3.2 $\text{N}_{1,2,3}$ disturbances with random 3D noise

To gain some understanding on the effect on transition of the azimuthal topology of the initial disturbance, a systematic search for the critical amplitude threshold has been implemented based on initial conditions consisting of $n_{\text{v}} = 1, 2$ and 3 pairs of rolls (N_1, N_2 and N_3 disturbances). As previously stated, the objective is to test their presumed higher capability of destabilising 3D waves despite their lesser transient growth when compared with N_1 perturbations. Ideally, we would have liked to test azimuthal wave-numbers of up to $n_{\text{v}} = 6$ so as to allow direct comparison with the 6-jet experimental injection used in HJM, but the azimuthal resolution this would require renders such an exploration unaffordable.

Lacking insight on the most rapidly growing axial wave-numbers, the 3D component of the perturbation has been introduced as a random velocity field fairly evenly distributing

among all modes an energy four to five orders of magnitude below that of the streamwise vortices. The objective is to make sure the optimal 3D waves are activated, notwithstanding the fact that some spurious energy is being wasted on irrelevant modes. No significant differences on the critical threshold should a priori be expected from using a random 3D perturbation instead of 3D waves within the optimal axial wave-number range. While the approach of adding a random perturbation is of much simpler implementation, the possibility of identifying the optimal waves by comparison with computations exciting exclusively certain (optimal) wave-numbers, can be very valuable, since it may be relevant to understanding transition and can help establish connections with recently found travelling-wave solutions [19, 78], some of which have wavelengths in the vicinity of the optimally destabilised 3D perturbations.

Thus, the critical threshold for N_2 and N_3 has been obtained and the one for N_1 recomputed for disturbances with a random 3D component, using the initial condition presented in (3.7). Over 100 additional runs with a spatial resolution of $(M_r \times N_\theta \times L_z = 33 \times 33 \times 33)$ have been performed to bound the critical threshold for the three different types of initial disturbance. Fig. 3.3 shows the critical amplitude thresholds of N_1, N_2 and N_3 disturbances with a random 3D noise added. The estimated asymptotic exponents, resulting from the analysis through linear regression of the evolution of the slope, are displayed with dashed straight lines.

A first obliged remark is that, for N_1, adding a random noise instead of activating the right axial wavelengths, as was done in the first exploration, does not alter the picture substantially. This seems to confirm that a small packet of waves can be held responsible for transition, the rest of modes playing no role whatsoever until the streaks have been broken and chaotic motion has set in. The exponent, however, seems to have slightly decreased to a value of $\gamma_1 \sim -1.35 \pm 0.02$, less pronounced than the previously found $\gamma = -1.47 \pm 0.02$. Exciting non-optimal wavelengths seems to deteriorate the capability of the 3D disturbance to bring about transition as Re is increased, as though competing waves were disturbing one another through nonlinear interaction, thus deferring transition.

The critical thresholds for N_2 and N_3 appear to be of a similar order of magnitude and both considerably lower than that for N_1, for moderate values of Re. It is therefore clear that, within the studied Re range, initial disturbances consisting of a couple of pairs of streamwise vortices are slightly more effective than those consisting of three pairs and considerably better than a single pair of vortices. However, it is not immediately clear whether this will still be the case at higher Re. Assuming the asymptotic regime of the critical threshold has more or less been established by the time we reach the right end of

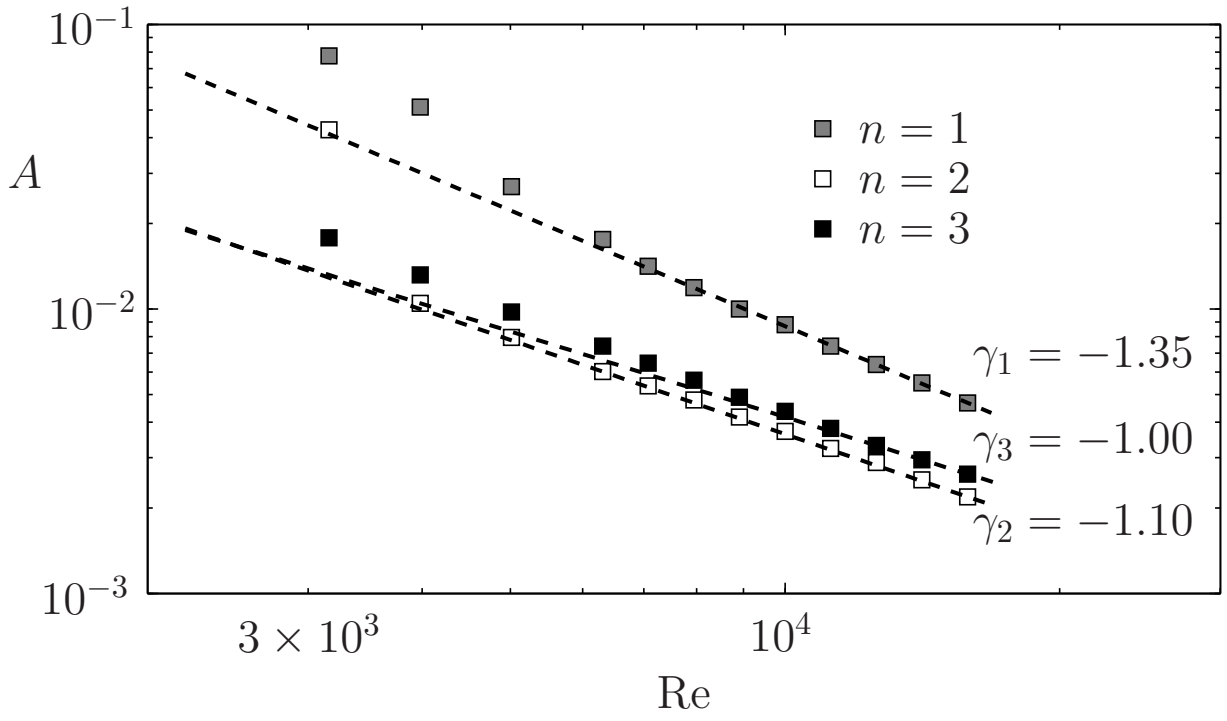

Figure 3.3: Critical amplitude threshold as a function of Re for initial disturbances made up of $n_{\mathrm{v}} = 1, 2, 3$-pairs of vortices and a much lower random 3D noise.

the explored Re range, N_1 disturbances stand a better chance of dominating the transition threshold for Re tending to infinity, as N_2 disturbances produce an exponent $\gamma_2 \sim -1.10 \pm 0.03$ and N_3 disturbances a $\gamma_3 \sim -1.06$, not yet stabilised but apparently tending towards -1. Nevertheless, the possibility that all disturbance thresholds mellow out asymptotically to an exponent $\gamma \sim -1$ cannot be discarded nor proved from the present study, since the exponent stabilisation may be apparent and its evolution could resume at higher Re.

To the difficulty of discussing the current results, we must add a further hindrance, namely that the critical amplitude at a given Re depends on the initial energy of the 3D component of the perturbation, which is assumed very small compared to the 2D component to ensure the streak breakdown mechanism, and not oblique transition, takes place. Chances are that the 3D perturbation energy level has an effect on the critical threshold at moderate Re but a rather weak one on its asymptotic exponent, since as Re increases the streaks lifetime stretches giving longer time for the 3D waves to grow, thus making their initial energy level irrelevant as long as it is finite. Figs. 3.4a, 3.4b and 3.4c exemplify the streak breakdown mechanism for the N_1, N_2 and N_3 types of initial disturbance, respectively. Depicted are the time evolution of the energy of the streaks

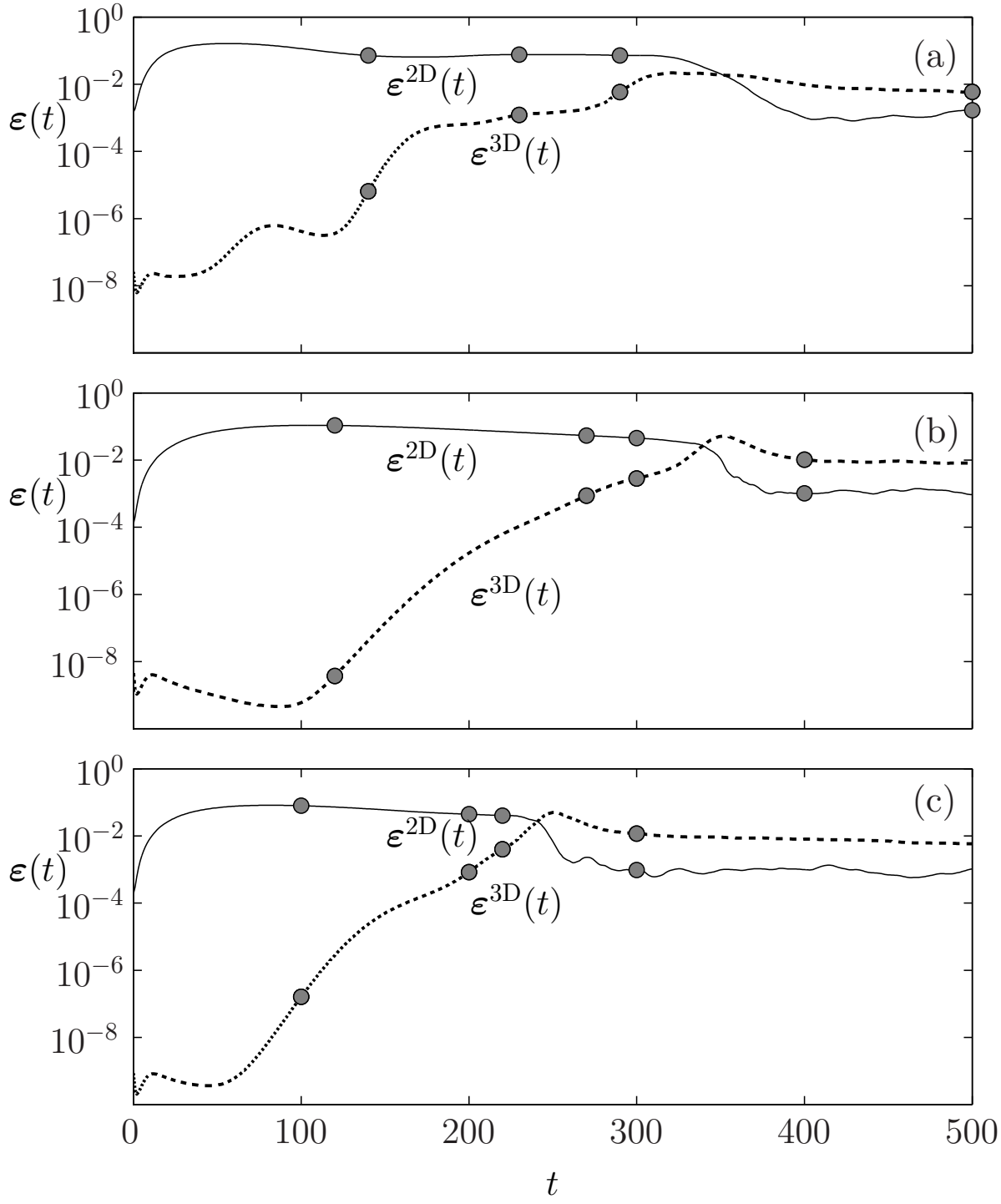

Figure 3.4: From top to bottom, energy-evolution plots of streak breakdown transition examples for vortical perturbations of the a) N_1, b) N_2 and c) N_3 types, for $Re = 5012$. In all three cases, the added 3D component is a random field.

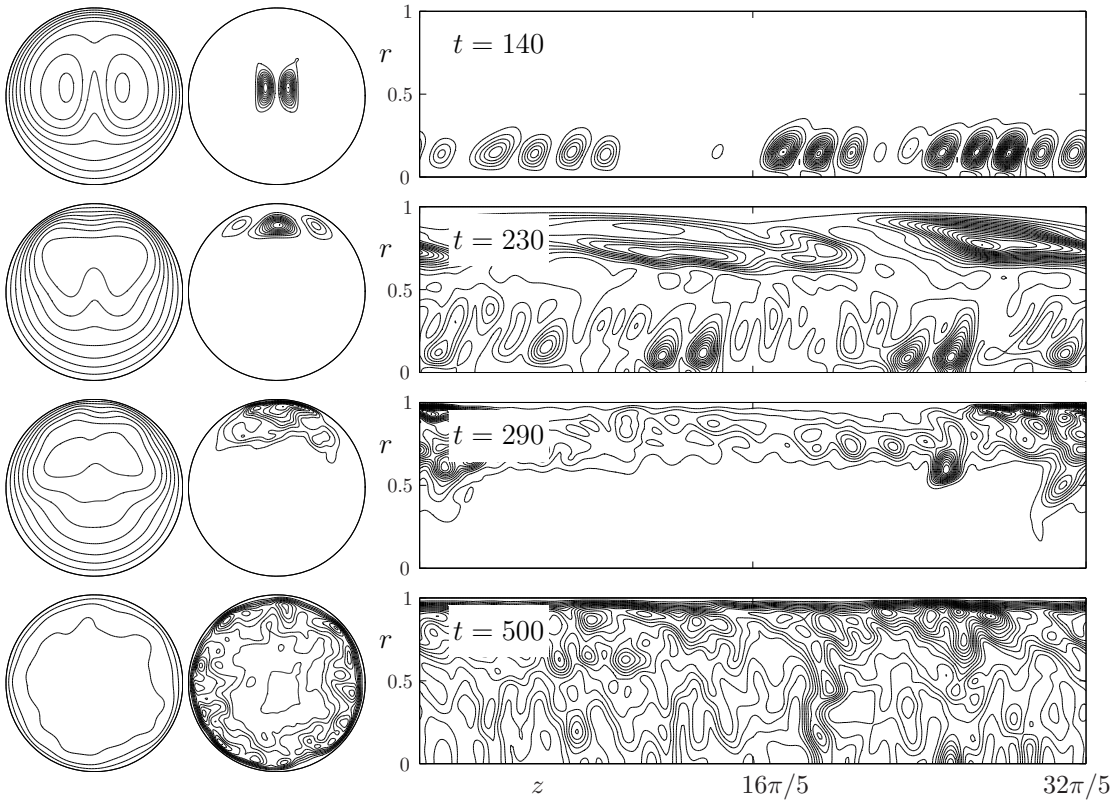

Figure 3.5: From left to right, contours of $\langle w \rangle_z$, $\langle \varepsilon^{3D} \rangle_z$ and $\langle \varepsilon^{3D} \rangle_\theta$, for the N_1 disturbance evolution with $\Lambda = 20.1$ and $Re = 5012$. Time elapses from top to bottom, with snaphots taken at the most relevant instants, marked with gray circles in Fig. 3.4a.

(ε^{2D}, solid line), together with that of the 3D component (ε^{3D}, dashed line). All three runs correspond to $Re = 5012$ and initial perturbations which are just supercritical ($A_1 = 2.75 \cdot 10^{-2}$, $A_2 = 8.13 \cdot 10^{-3}$ and $A_3 = 10^{-2}$, for the N_1, N_2 and N_3 cases, respectively). As expected, in all three cases the streaks develop and excite 3D modes that start growing exponentially until they acquire sufficient energy to nonlineary interact with the streaks and bring about transition. The N_1 case exhibits a slightly more complex behaviour as the different stages of the 3D perturbation energy growth evince.

In Figs. 3.5, 3.6 and 3.7, three series of snapshots at selected times, conveniently indicated with gray circles on the energy-evolution plots (Figs. 3.4a, 3.4b and 3.4c), help illustrate the streak breakdown process for each type of vortical disturbance. On the left of Figs. 3.5-3.7, z-averaged cross-sectional contours of the axial speed component of the flow $\mathbf{v} = (u, v, w)$ are represented within the range $0 \leq \langle w \rangle_z(r, \theta, t) \leq 1$ in order to visualise the streaks formation and destabilisation. The center and right vertical sequences

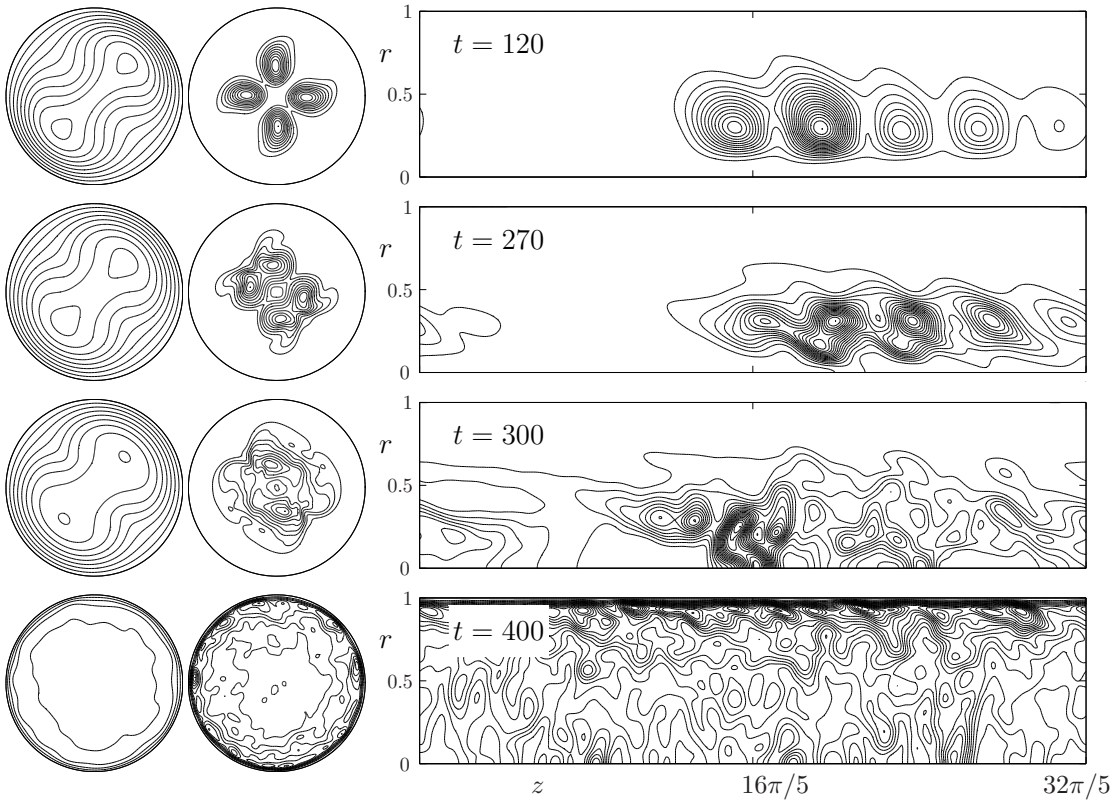

Figure 3.6: Same as Fig. 3.5, for the N_2 perturbation. Snapshots are taken at instants marked with gray circles in Fig. 3.4b.

of pictures correspond to energy density contours of the velocity component $\mathbf{u}_{3D}(r,\theta,z,t)$ appearing in (3.4). More specifically, the central array of figures contains z-averaged cross-sectional contours, while the right array shows θ-averaged contours on a transversal section $(r,z) \in [0,1] \times [0,\Lambda]$. The aforementioned energy density averages are given by

$$\langle \varepsilon^{3D} \rangle_z (r,\theta,t) = \frac{1}{2} \int_0^{\Lambda} \parallel \mathbf{u}_{3D}(r,\theta,z,t) \parallel^2 \ \mathrm{d}z, \tag{3.9}$$

and

$$\langle \varepsilon^{3D} \rangle_\theta (r,z,t) = \frac{1}{2} \int_0^{2\pi} \parallel \mathbf{u}_{3D}(r,\theta,z,t) \parallel^2 \ \mathrm{d}\theta, \tag{3.10}$$

and their contours are drawn in arbitrary units. In addition, the axial coordinate of the longitudinal sections has been conveniently scaled to aid representation. These series of contours reveal the modal structure of the 3D waves as well as their location and destabilisation effects over the streaks. A fixed number of contour lines is extrapolated between 0 and the maximum energy at each particular instant of time.

Because of their simplicity, it seems natural to start by discussing the N_2 and N_3 cases, shown in Figs. 3.6 and 3.7, respectively. The 3D perturbation organises itself and grows

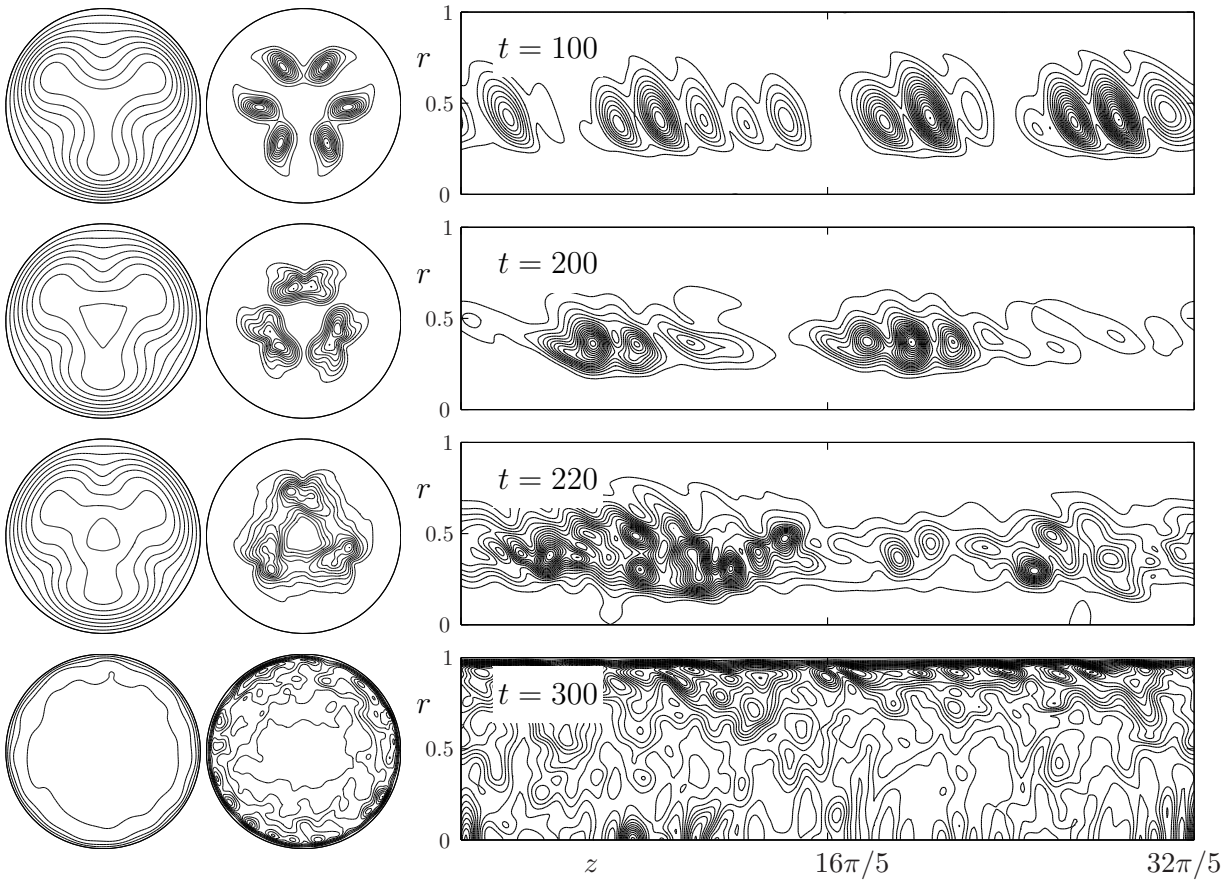

Figure 3.7: Same as Fig. 3.5, for the N_3 perturbation. Snapshots are taken at instants marked with gray circles in Fig. 3.4c.

exponentially in the vicinity of the saddle lines of the streaks-modulated axial velocity profiles, as can be seen in the snapshots at $t = 120$ for N_2 and $t = 100$ for N_3. Once the 3D perturbation has reached a sufficient energy level, nonlinear interaction with the streaks starts ($270 \leq t \leq 300$ for N_2 and $200 \leq t \leq 220$ for N_3), destabilising the laminar profile and leading to turbulence. It should be noted that the axial structure of the 3D waves is neither long nor stretching, which could be taken as an evidence that the transition scenario investigated does not contemplate the possibility of local transition or intermittency phenomena, plausibly rendering results fairly independent of the pipe length considered. It should also be noted that the structures shown in the longitudinal sections of Figs. 3.5-3.7 are being advected downstream and hence re-enter the domain from the left as soon as they leave it through the right-end due to the axial periodicity.

Conversely to what happens in the N_2 and N_3 cases, the N_1 case admits no easy interpretation, as several 3D modes seem to compete at different stages of the streaks formation

and development. In a first stage, the 3D perturbation seems to be transiently concentrated near the wall, where the axial velocity gradients are largest (not shown in Fig. 3.5), to be eventually absorved by a stronger perturbation that grows up closer to the pipe centreline, in the vicinity of the saddle lines of the axial velocity profile ($t = 140$ in Fig. 3.5). This centered perturbation grows rapidly until it saturates and is then overtaken again by near-wall components ($t = 230$) that eventually destabilise the streaks ($t = 290$) and trigger transition. The wavelength of the dominant perturbation at each stage of the process varies. Long wavelengths only become dominant in the last stages before transition.

3.3.3 Pipe length effects on transition

The streak breakdown mechanism is based on the development of a global inflectional profile affecting the whole pipe length. The mathematical explanation is provided when studying the streamwise invariance of the $\mathbf{u}^{2D}$ introduced initially. The structure of equation (2.11) preserves streamwise independence of $\mathbf{u}^{2D}(t)$ due to the fact that the disturbance has spanwise components only, whereas the basic flow is purely streamwise. Therefore, upon streaks generation, saddle points, or rather saddle streamwise lines, appear along the pipe, resulting in an inflectional instability of the $\mathbf{u}^{3D}(t)$ components destabilising the whole pipe length at once. The inflectional stability thus generated has been numerically shown to follow selection rules as to which axial wave-numbers can be destabilised by the streaks [40, 81]. The streak breakdown transition process happens to be clearly dominated by medium-short wavelengths of order $\mathcal{O}(\lambda) \sim \pi$. Hence, no substantial discrepancies can be expected when repeating the computations on a longer aspect-ratio pipe.

Intermittency is a commonly observed phenomenon in experimental pipe transition. Perturbations initially localised in space lead to small patches of turbulent motion called *slugs* that, while convected downstream, grow into the surrounding laminar regions to end up filling the whole pipe domain. To properly capture this behaviour numerically, long enough computational domains need to be set up for these long-scale turbulent structures to show up and grow freely. The aspect ratio we have used so far ($\Lambda = 6.4\pi \sim 20$) is clearly too short to allow for intermittency phenomena, whose characteristic length has been shown bigger [26, 67]. However, the transition mechanism studied here is *global*; hence, not depending on the formation of long structures, but of medium-short ones.

To assess the pipe-length effects on streak-breakdown transition, we have computed the critical threshold for N_1 disturbances, exciting only the optimal 3D waves, but this time on a much longer pipe of $\Lambda = 32\pi \sim 100$. To preserve a somewhat sufficient representation

Re	A_{cr}	
	short pipe	long pipe
4467	$4.6 \cdot 10^{-2}$	$4.7 \cdot 10^{-2}$
5012	$3.3 \cdot 10^{-2}$	$3.3 \cdot 10^{-2}$
6310	$1.8 \cdot 10^{-2}$	$1.8 \cdot 10^{-2}$
8913	$1.1 \cdot 10^{-2}$	$1.1 \cdot 10^{-2}$
12589	$6.4 \cdot 10^{-3}$	$6.4 \cdot 10^{-3}$

Table 3.1: Critical amplitude threshold as a function of Re for initial disturbances made up of a single pair of vortices and waves of selected axial periodicity derived from computations on a short ($\Lambda \sim 20$-radii) and a long ($\Lambda \sim 100$-radii) pipe.

of the small axial scales, the axial gridpoints count has been fourfolded to produce a mesh of $M_r \times N_\theta \times L_z = 33 \times 33 \times 129$. The triads $l_i = \{30, 35, 40\}$ for $|n| = 0, 1$ in (3.5) have been excited to activate the same 3D waves that were activated in the short pipe version, i.e. $\mathrm{k}_i = \{1.56, 1.88, 2.19\}$. Table 3.1 reports the critical amplitudes for the long and the short pipe.

It is reasonably clear from the compared results that no significant differences are introduced by a pipe elongation, at least for computational domains of up to 100-radii.

As a last verification that pipe-length effects are of little importance in the streak breakdown transition scenario, the evolution of N_1-type disturbances defined in (3.7) and shown in Fig. 3.4a and Fig. 3.5 has been computed on the longer computational domain. An exact evolution cannot be expected in any case, since the random 3D energy, now distributed among extra axial modes that were not present in the short pipe case, makes a perfect timing unachievable. Also the slight reduction of axial resolution, inevitable to compute on such a long domain, may have an effect on the results. Fig. 3.8 shows the energy-evolution plot for the N_1 disturbance on the long pipe, to be compared with that on the short pipe (Fig. 3.4a).

The streaks development is completely analogous. As to the 3D component of the perturbation, the agreement is reasonably good but for a couple of discrepancies that need comment. First, at the very initial stages of the streaks formation, the short pipe exhibits 3D energy oscillations that are not present in the long pipe. The reason is that the long pipe simulation takes into account modes with very low axial wave-number, not captured in the short pipe version. These modes are known to experience large algebraic transient growth that could be masking the organisation of the 3D waves that are to be destabilised later by the streaks. Second, in the latter stages before transition, the short pipe seems

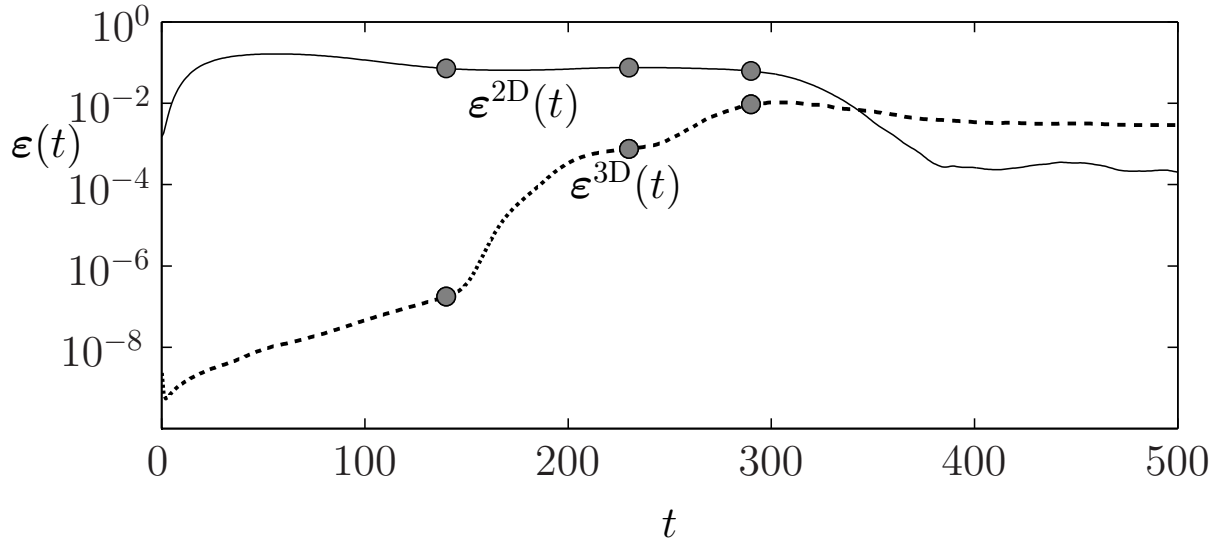

Figure 3.8: Same as Fig. 3.4a, but computed on the long pipe.

to hesitate a bit longer before bringing about streak breakdown. The slightly diminished axial resolution of the longer pipe, thus dissipating less energy in the small scales could be at the origin of the slightly faster transition. Another possible explanation for the faster transition on the long pipe when compared with the short one could be derived from the random properties of the 3D noise. If, as we hypothesise, the streak breakdown transition is global and only depends on short-medium wavelengths, the long pipe could be behaving as a mere concatenation of short pipes, each with its particular random 3D component. It would not be strange, then, that a particular section of the whole pipe receives a more effective initial random field and ends up triggering transition ahead of the rest of sections, which eventually achieve enough energy to also destabilise their region of influence, now probably competing with another mechanism, namely the growth of the already transitioned turbulent patches. For all this, the long pipe could be behaving as the most effective of 5 short pipes, each with a different random noise. This is just a simplification, since the different sections of the long pipe are not evolving independently, but gives an idea of what could be actually happening.

Figure 3.9 shows the same pics that were presented in Fig. 3.5 except those for the largest time at which developed turbulence is observed. The same caption times that were used for the short pipe have been retained, although the 3D perturbation is at slightly different stages of evolution. The fact is that streaks are evolving all throughout the process and, therefore, influencing the location and shape of the 3D perturbation independently of its magnitude, which depends on the pseudo-linear inflectional instability mechanism.

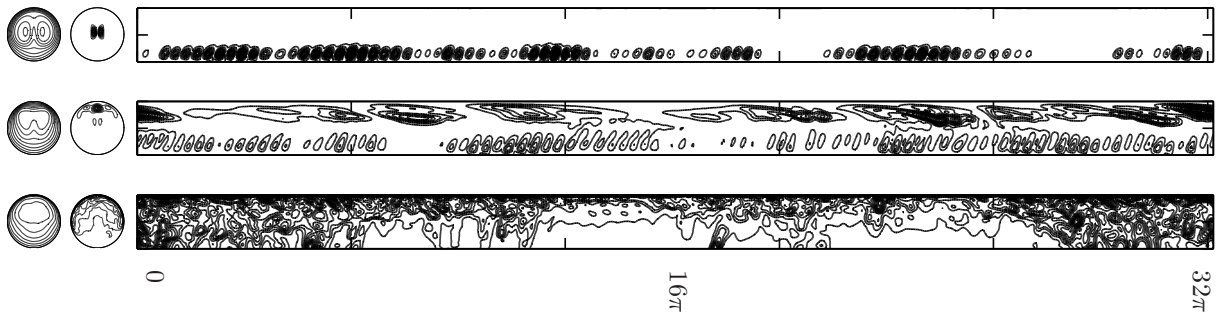

Figure 3.9: Same as Fig. 3.5, but on the long pipe with $\Lambda = 100.5$. Snapshots are taken at instants marked with gray circles in Fig. 3.8. From left to right, $t = 140$, $t = 230$ and $t = 290$.

The sequence shows a very good agreement between short and long pipe results. Only the smallest scales are slightly worse resolved in the long pipe, as some resolution has been sacrificed to produce a longer domain. It is interesting to see how the transition process is dominated by short-medium wavelengths that get destabilised at random locations along the pipe length, are advected with the mean flow and end up triggering transition. Transition can be considered both local and global in nature. Local because turbulence first appears at discrete axial positions. Global, because the spacing of these axial positions is considerably short and no intermittent structures such as slugs have time or space to appear and then stretch freely to end up polluting the whole domain.

3.4 Conclusions

The capability of vortical streamwise perturbations to trigger transition in pipe flow has been assessed and an upper bound for their critical amplitude provided by means of accurate numerical simulations based on a theoretical scenario of transition that has been proved to be universal in many other shear flows. The computations have been carried out using suitable time windows, making it possible to distinguish relaminarisation from long-lasting nonlinear chaotic dynamics. The criteria for transition within the specified time horizons is based on the comparison of relative amplitude of the two-dimensional and three-dimensional perturbation components.

The computed amplitude threshold seems to scale differently for vortical perturbations consisting of different numbers of pairs of rolls. Thus, our best estimates suggest that single-paired vortical disturbances follow an asymptotic scaling law $A_c \sim Re^{-1.5 \leq \gamma \leq -1.35}$, while double and triple-paired perturbations respond to scaling laws $A_c \sim Re^{-1.1}$ and

$A_c \sim Re^{-1.0}$, respectively, for the highest Reynolds numbers explored. Although the critical threshold shrinks faster for the single-paired vortical disturbances, two or three pairs of rolls are more effective in triggering transition within the explored Re-range, making it adventurous to proclaim which type of perturbations will dominate at higher Re numbers.

Results at the lower end of explored Re, where even very strong disturbances only lead to transient destabilisation, evidence the vertical region of what is often called the *double threshold*. Somewhere around $Re \sim 2000$, the critical threshold tends to a vertical asymptote and no sustained turbulence is ever achieved for lower Re.

The instability mechanisms based on the streak breakdown process presented in this work may be difficult to reproduce in the laboratory due to the fact that this scenario requires a streamwise initial perturbation, which is irrealisable in experiments by localised injections that necessarily trigger three-dimensional components of some streamwise structure. In addition, our numerical explorations do not exhibit any of the transitional structures frequently observed in experiments, characterised by the coexistence or intermittency between laminar and turbulent regimes. Further computations carried out for pipe aspect ratio $\Lambda \sim 100$ involving nearly 1.5×10^5 degrees of freedom confirm the global nature of the considered instability mechanism, where long wavelengths take the lead only towards the final stage before transition. Nevertheless, the length scale of these developing waves is not dramatically missrepresented in the short pipe computations.

Other internal mechanisms could also be at work in the transition process and also longer time horizons with $T > T_{\max}$ should be explored in order to check for eventual relaminarisation of cases considered turbulent in the present work, along with its implications in the value of the exponent, i.e., $\gamma = \gamma(T)$. All these issues will be addressed in future works but they are currently far beyond the scope of our study.

CHAPTER 4

TRANSITION FOLLOWING LOCALISED PERTURBATIONS

As we already did in chapter 3, we are here concerned with providing a characterisation of the *basin of attraction* of the basic laminar solution, but now focusing on localised perturbations as those usually inflicted in experimental studies. It has already been advanced that the basin of attraction *is not* a bounded set and that its *size* is a meaningless measure because it is actually infinite. Thinking of the *critical threshold* as the boundary of that basin of attraction that approaches a minimum norm A from the steady solution, the question is then what sort of dependence has this norm or amplitude with respect to the Reynolds number, $A = A(Re)$. As previously, we deem reasonable to assume that its asymptotic behaviour scales with Re according to

$$A \sim Re^{\gamma}, \tag{4.1}$$

with γ necessarily negative. In this context, A represents the minimum amplitude of a perturbation capable of destabilising the basic profile, thus leading to a turbulent regime.

Expression (4.1) implicitly involves many physical aspects that require an accurate description. First, a mathematical definition of the amplitude A appearing in (4.1) must be provided. Second, the geometrical features of the perturbation (azimuthal symmetry or streamwise dependence, for example) will necessarily conditionate the subspace over which we are measuring the amplitude appearing in (4.1). Third, depending on the perturbative methodology used, the dynamical system scenario of the problem may fall into two different categories. Either the perturbation may develop from an initial disturbance of the basic flow, the fluid system evolving in an *autonomous* fashion, or it may develop from a *time-dependent* source such as an external forcing or time-dependent boundary conditions. Fourth, when studying the time evolution of a perturbation in an open flow, advection is crucial, since potential turbulent transients flush down the drain, making it impossible to classify the dynamics for long times. Once an observational *time-horizon*, say T, is chosen, one must establish criteria to distinguish between laminar, relaminarised or turbulent states. As a result, the critical exponent appearing in (4.1) will implicitly depend on the time horizon chosen [5], i.e., $\gamma = \gamma(T)$. Fifth, expression (4.1) is only meaningful for high values of Re.

Theoretical exponents for plane channel flows have been obtained by means of asymptotic methods within the framework of some particular transition scenarios [8]. For pipe flow, recent renormalisations [71] have been suggested in order to cast different experimental results in terms of a single definition of the amplitude appearing in (4.1), providing

lower and upper bounds for the value of this critical exponent that presumably lies within the interval $\gamma \in [-9/5, -6/5]$.

Very recent experiments carried out by Hof, Juel & Mullin [27], henceforth referred as HJM, explored transition phenomena of pipe flow subjected to finite amplitude impulsive perturbations for a wide range of axial speeds of the flow. The experiments reported in HJM were carried out in a long aspect ratio pipe, with a piston that kept the mass-flux constant during every run and where the disturbances were generated by impulsively injecting fluid into the main flow through six slits azimuthally equispaced on a perimeter around the pipe located at a fixed axial position far downstream from the pipe inlet, so that the HPF flow was sufficiently developed. The experimental results of HJM clearly concluded that the minimum amplitude of a perturbation required to trigger transition scaled as the inverse of the Reynolds number, i.e., $A = \mathcal{O}(Re^{-1})$. The experimental procedure of perturbing the basic flow would correspond to the category of time-dependent (non-autonomous) perturbative methods.

By contrast, numerical simulations [40, 38] based on initial streamwise perturbations concluded that the minimum amplitude, defined as the square root of the kinetic energy, required to destabilise the flow, scaled as $A = \mathcal{O}(Re^{\gamma})$, with γ between -1 and $-3/2$, depending on the type of initial vortical perturbation chosen. The discrepancy with the experimental results might probably relate to the definition of the perturbation amplitude used in Meseguer [40], Mellibovsky & Meseguer [38], which is not applicable to the type of perturbations used in HJM. Nevertheless, transition in pipe flow strongly depends not only on the amplitude of the initial perturbation, but also on its symmetry features, being globally stable, for instance, with respect to axisymmetric perturbations [52]. The perturbation mechanism used in Meseguer [40], Mellibovsky & Meseguer [38] corresponds to the category of autonomous perturbative methods, since there is no time-dependent forcing of the Navier-Stokes problem. It is for consistency with these studies, that we chose to keep the same flow-driving mechanism used previously, namely a constant axial pressure gradient, instead of implementing a constant mass-flux pipe.

The main goal of this work is to gain some insight on the internal mechanisms responsible for transition by reproducing numerically the experiments of HJM with an accurate spectral method. The main difference between the present study and HJM experimental work concerns the principle driving the fluid along the pipe. As we pointed out earlier, the pressure drop (or streamwise forcing) is held constant throughout each of our computations, letting the massflow vary freely as perturbations develop within the flow. Conversely, the experiments force a prescribed massflow by means of a time-dependent forcing that,

inflicted upon the fluid by a constant-speed sucking piston, injects or substracts energy into or from the flow.

This chapter is structured as follows. The numerical modelling of the injected perturbation is presented in §4.1, where special attention is given to relating the numerical injection amplitude to its experimental counterpart. §4.2 deals with the injection-time dependency of the amplitude threshold, comparing it with experimental data. A typical transitional experiment is analised in §4.3 to demonstrate the effects of localised impulsive injections. In §4.4, an extensive exploration is undertaken to determine the critical amplitude threshold as a function of the Reynolds number. Finally, the main conclusions drawn from this study are summarised in §4.5.

4.1 Mathematical formulation and perturbation modeling

We follow the same formulation as the one discussed in section 2.1. The parameter governing the dynamics of the problem is the *nominal* Reynolds number Re, based on the basic laminar flow corresponding to a given axial pressure gradient,

$$Re = \frac{a\mathrm{U_{cl}}}{\nu} = \frac{-\Pi_0 a^3}{4\rho\nu^2}, \tag{4.2}$$

whereas the *actual* Reynolds number used in the experiments by HJM is defined as

$$Re_{\mathrm{a}} = \frac{d\,\overline{\mathrm{U}}}{\nu}, \tag{4.3}$$

where $d = 2a$ is the pipe diameter and

$$\overline{\mathrm{U}} = \frac{1}{\pi a^2}\int_0^{2\pi}\int_0^a w\; r\; \mathrm{d}r\; \mathrm{d}\theta \tag{4.4}$$

is the mean axial instantaneous speed of the flow. Accordingly, the actual Reynolds number Re_{a} will be an evolving quantity in the Navier-Stokes equations representing a pressure-driven pipe. Both Reynolds numbers coincide for the laminar Hagen-Poiseuille profile, regardless of the pressure-driven or constant mass-flux nature of the problem. In a constant mass-flux pipe, Re_{a} is forced to remain always constant through the action of a time-dependent adapting volume force, whereas in a pressure-driven pipe, it exhibits a considerable drop as turbulence sets in.

In our explorations, the pipe length has been fixed to $\Lambda = 12.8\pi \sim 40$ radii units and the spatial resolution used in the domain $\mathfrak{D}$ has been set to $M_r \times N_\theta \times L_z = 33 \times 65 \times 65$

(radial×azimuthal×axial) grid points, resulting in a dynamical system of nearly 1.4×10^5 degrees of freedom. The energy contents of the highest axial/azimuthal fourier modes has been monitored for every single run to ensure the adequacy of the spatial truncation. For subcritical runs, an energy decay of 6 to 7 orders of magnitude below that of the basic flow has been considered enough. Transitional runs are clearly under-resolved when turbulent motion begins. The computational costs of the resolution that would be required are unaffordable, but it must be bore in mind that it is not the aim of this study to simulate turbulence, but to bound the basin of attraction of the basic flow. Hence, the resolution is certainly not sufficient for runs exhibiting transition once turbulence sets in, but suffices to properly represent the laminar phases of the transition process. A few cases have been run at the high Re-range with doubled axial resolution ($L_z = 129$), producing no qualitative differences in the observed critical amplitude trends when compared with those obtained with the lower resolution. Thus, the lower resolution has been kept for the bulk of simulations, since every single high resolution run (a single perturbation amplitude at a given Re) takes nearly 15 days on a 3GHz P4. The numerical reliability of the method has been extensively tested for low and high resolution computations [43, 44, 40, 37].

4.1.1 Numerical model of the six-jet impulsive injection

Equations (2.11-2.16) describe the spatio-temporal evolution of an arbitrary perturbation, the source of disturbances being prescribed by the initial condition $\mathbf{u}_0$ in (2.16). As mentioned in the Introduction, different scenarios of transition have been studied [40, 37] based on specific initial perturbations. In the present work, no initial perturbation is to be prescribed, *i.e.*, $\mathbf{u}_0 = 0$, and the disturbances will be generated by the action of an external forcing.

Figure 4.1a is a schematic plot of the injection device used in HJM, where the six slits are equally distributed along the perimeter of the pipe so that the injected fluid jet penetrates into the basic flow with an angle $\varphi = \pi/3$ with respect to the radial coordinate, in a plane normal to the pipe axis. In addition, the injection is located at a particular streamwise coordinate for which the basic Hagen-Poiseuille flow profile can be considered as fully developed. Besides, the injection is activated following a step-like time-dependent function, active for a prescribed injection duration. We refer the reader to HJM [11, 27] for further details.

Numerical spectral modeling of the device shown in Fig. 4.1a is not a trivial task. To start with, fluid is injected from the wall, thus violating the homogenous boundary condition

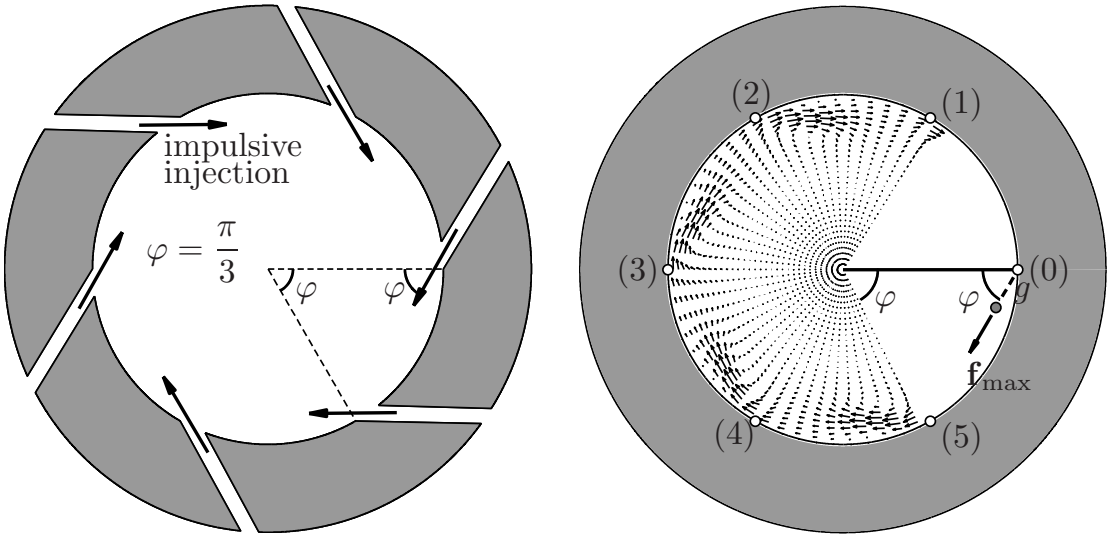

(a) (b)

Figure 4.1: (a) Six-jet injection device used in Hof, Juel & Mullin [27] experiments . Fluid is injected from six azimuthally equispaced slits around a perimeter of the pipe at a fixed streamwise location. (b) Acceleration field $\partial_t \mathbf{u}$ at $t = 0$ and $z = 0$, resulting from the forcing $\mathbf{f}$ in (4.6). See the Appendix for details.

(2.13). Second, we do not know a priori the nature of the injected flow regarding its spatial structure, i.e., laminar or turbulent profile and penetration capability. Third, the boundary condition at the wall is time-dependent, in contrast with (2.13). Moreover, since the fluid is injected impulsively, which requires a time lapse to do so, the initial condition (2.16) cannot represent by any means such mechanism.

The aforementioned difficulties can be mostly overcome by means of adding an impulsive volume force term $\mathbf{f}$ in equation (2.11), playing the role of the injection. This forcing acts locally in time and space as an accelerator of the fluid and can be chosen and suitably modified until the dynamics observed are in agreement with the experimental observations. In this work, we are going to study the perturbative effects generated by introducing in (2.11) an impulsive volume forcing term, $\mathbf{f}$, localised in time and space, i.e.,

$$\partial_t \mathbf{u} = -\nabla q + \mathbf{f} + \frac{1}{Re}\Delta \mathbf{u} - (\mathbf{v}_{\mathrm{B}} \cdot \nabla)\mathbf{u} - (\mathbf{u} \cdot \nabla)\mathbf{v}_{\mathrm{B}} - (\mathbf{u} \cdot \nabla)\mathbf{u}. \tag{4.5}$$

The length scale of the experimental injection holes is far too small to be captured in a feasible discretisation. As a result, the approach of modeling the effects of an injection, rather than the injection itself, seems a reasonable option. Thus, it is assumed that the only, or of outmost importance, effect of the injection is that of accelerating the fluid around

the jet. The forcing field $\mathbf{f}$ appearing in (4.5) is introduced so that the resulting local acceleration is qualitatively equivalent to the one generated by the injection experimental device. We can properly represent the number of injection points (six) and the angle at which the jets penetrate the pipe ($\pi/3$). The width of the jets in the cross-sectional plane can be more or less approximated, but not so much so in the streamwise direction where a smoother profile must be used due to the *coarse* axial discretisation of the domain. Finally, the penetration of the jet becomes the least guided decision to be taken, as no data on this is readily available.

In the present study, the forcing field has the following structure:

$$\mathbf{f}(r,\theta,z,t) = \mathrm{f_a}\,\mathrm{f}_t(t)\,\mathbf{f}_s(r,\theta,z), \tag{4.6}$$

where $\mathrm{f_a}$ is the amplitude factor. The injection time-dependence is introduced through a double-step function $\mathrm{f}_t(t)$, given by

$$\mathrm{f}_t(t) = \begin{cases} 1 & t \leq \Delta t_{\mathrm{inj}} \\ 0 & t > \Delta t_{\mathrm{inj}}, \end{cases} \tag{4.7}$$

acting as a switch that remains activated within the time interval $t \in [0, \Delta t_{\mathrm{inj}}]$. Finally, $\mathbf{f}_s$ provides the spatial structure of the six-jet injection and its explicit mathematical expression is presented in the next section. Figure 4.1b shows the acceleration field inflicted by the modelled forcing upon the stationary basic flow.

Values of the injection lapse within the range $\Delta t_{\mathrm{inj}} \in [2, 24]$ advective time units have been used throughout the present study. It would make no sense to report on the amplitude factor ($\mathrm{f_a}$) range explored, since it is only intended to scale/modulate the arbitrary original norm of the spatial structure $\mathbf{f}_s$ and therefore has a purely relative meaning.

4.1.2 Spatial structure of the 6-jet injection model

To construct the spatial structure $\mathbf{f}_s$ of the forcing field $\mathbf{f}$ introduced in (4.5), a draft skeleton for the acceleration field $\mathbf{a}$ must be generated, observing the main properties that are desired. The consistency of this field in terms of solenoidality and boundary conditions can be initially overlooked, as it will be resolved upon projection onto the Petrov-Galerkin projection basis functions inherited from the numerical method used in the spatial discretisation [40, 44].

The skeleton for the spatial structure of the forcing term $\mathbf{f}_{\mathrm{s}}$ appearing in (4.6) is written

as a superposition of as many fields as injection points,

$$\mathbf{a}(r,\theta,z) = \sum_{j=0}^{5} \mathbf{a}_j(r,\theta,z) = \sum_{j=0}^{5} \mathbf{a}_0(r,\theta-\frac{\pi}{3}j,z). \tag{4.8}$$

Due to the periodic azimuthal distribution of the holes, all of them at the same axial position, only the forcing field frame for the first slit, $\mathbf{a}_0$, needs to be engineered, the rest resulting from simple rotations.

The acceleration field $\mathbf{a}_0$ is set up as an homogeneous field of vectors pointing in the direction of the injection (at an angle φ_0 with respect to the radial direction), with their magnitude modulated with independent gaussian distributions in the three natural directions: jet-wise, jet-transverse and pipe-streamwise, represented in Fig. 4.2 by $\hat{\mathbf{x}}_0$, $\hat{\mathbf{y}}_0$ and their vector product $\hat{\mathbf{x}}_0 \wedge \hat{\mathbf{y}}_0$, respectively. Because the acceleration on the walls will have

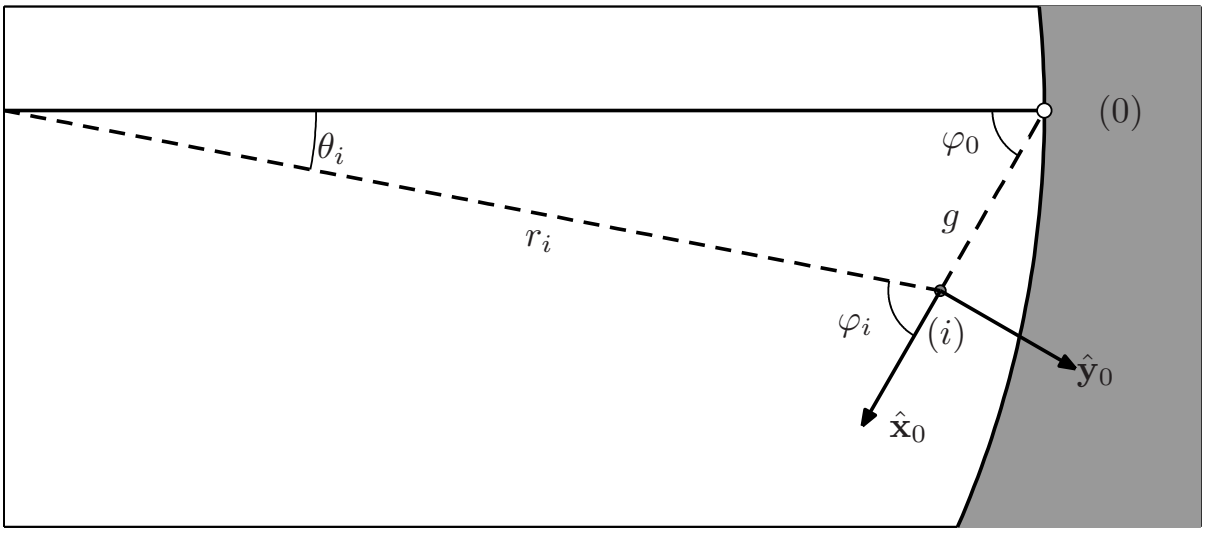

Figure 4.2: Cross-sectional cartesian coordinate system used in designing the jet corresponding to the first injection point.

to cancel out, the centre (i) for the gaussian distributions, where the acceleration is going to be at its maximum, is drifted along the jet axis a certain distance g within the fluid domain, so that the vector field to be projected does not severly violate the boundary conditions. This helps to avoid great distortion of the prescribed vector field upon obtention of the actual forcing to be used, since we are departing from a field which is closer to an acceptable solution.

This vector field is most easily written in the system of cross-sectional cartesian coordinates $(x,y) = x\,\hat{\mathbf{x}}_0 + y\,\hat{\mathbf{y}}_0$, with origin at (i), depicted in Fig. 4.2. In this coordinate system,

the vector field takes its simplest form:

$$\mathbf{a}_0(x,y,z) = (a_x, a_y) = \mathrm{e}^{-Ax^2-By^2-C\sin^2(\frac{2\pi}{\Lambda}z)}\ \hat{\mathbf{x}}_0, \tag{4.9}$$

where B and C govern the jet-transverse and pipe-streamwise widths of the jet, A its jet-wise penetration within the fluid domain and Λ is the pipe aspect ratio. Typical values used throughout the present work have been $A = 15$, $B = 150$, $C = 75$, $\Lambda = 12.8\pi$, $\varphi_0 = \pi/3$ and $g = 0.25$.

The local (x, y) coordinates are related to the polar system (r, θ) according to the change

$$\begin{cases} x = -(r\cos\theta - r_i\cos\theta_i)\cos(\varphi_i+\theta_i) - (r\sin\theta - r_i\sin\theta_i)\sin(\varphi_i+\theta_i) \\ y = (r\cos\theta - r_i\cos\theta_i)\sin(\varphi_i+\theta_i) - (r\sin\theta - r_i\sin\theta_i)\cos(\varphi_i+\theta_i), \end{cases} \tag{4.10}$$

where (r_i, θ_i) and φ_i are the polar coordinates of the origin of the cartesian coordinate system and its orientation, respectively. Note that in Fig. 4.2, θ_i is negative. These quantities follow directly from the injection parameters:

$$\begin{cases} r_i = \sqrt{1+g^2-2g\cos\varphi_0} \\ \theta_i = \varphi_0 - \varphi_i \\ r_i\,\sin\varphi_i = \sin\varphi_0. \end{cases} \tag{4.11}$$

The frame of the acceleration field is finally expressed in cylindrical coordinates:

$$\mathbf{a}_0 = (\mathbf{a}_0)_r\,\hat{\mathbf{r}} + (\mathbf{a}_0)_\theta\,\hat{\theta} + (\mathbf{a}_0)_w\,\hat{\mathbf{z}} = -a_x\,\cos(\varphi_i+\theta_i-\theta)\,\hat{\mathbf{r}} - a_x\,\sin(\varphi_i+\theta_i-\theta)\,\hat{\theta}. \tag{4.12}$$

The forcing field skeleton we have just constructed does neither respect the boundary conditions nor the solenoidality condition. A compatible forcing field, $\mathbf{f}_s$, fit to be used in (4.6), is obtained upon projection of $\mathbf{a}$ in (4.8) onto the dual basis of the solenoidal spectral scheme used in this work's spatial discretisation [40, 44].

4.1.3 Relating the numerical injection amplitude to its experimental counterpart

One of the main difficulties is the quantitative comparison of the effect produced by the numerical injection just formulated and the actual experimental one. Some insight may be obtained from the *axisymmetric jet-theory* [60]. Assuming the jet penetrates a resting fluid in a direction normal to the wall from which it emanates, and that it is locally axisymmetric around its propagation axis, which are rough idealisations, its *kinematic momentum* [60] is

$$\mathrm{K}' = 2\pi\int_0^\infty u(\varrho)^2\,\varrho\,\mathrm{d}\varrho, \tag{4.13}$$

where $u(\varrho)$ refers to the jet-wise component of the induced velocity field at a distance ϱ from its axis. The value of $u = u(0)$ on the jet axis, at a distance g from the slit is also provided by the theory [60],

$$u = \frac{3}{8\pi}\frac{\mathrm{K}'}{\nu g}. \tag{4.14}$$

The objective is to relate the velocity at a given point on the jet axis to the injected massflow, on which quantity rests the amplitude definition used in the experiments by HJM. In practice, the point where the forcing field $\mathbf{f}$ attains its maximum norm is chosen and the time evolution of the jetwise-projected flow velocity at this point, induced by sustained action of the forcing for all t, monitored. Under the assumption that the asymptotic laminar velocity to which the fluid flow tends corresponds to that of an idealised jet, the axisymmetric jet theory can be used to recover the amplitude of the injection that would potentially produce this asymptotic velocity at the particularly chosen point.

The kinematic momentum defined in (4.13), which must be conserved in the jet axial direction, can be expressed as a function of the injected massflow through one of the slits,

$$\mathrm{K}' = \beta\frac{\Phi_{\mathrm{inj}}^2}{\mathrm{S}_{\mathrm{inj}}}, \tag{4.15}$$

where $\mathrm{S}_{\mathrm{inj}}$ is the cross-sectional area of the slit and β is a parameter depending on the jet velocity profile considered ($\beta = 4/3$ or 1 for a laminar or a turbulent jet, respectively). It will be assumed that the penetrating jet will commonly be turbulent. By identifying our *finite-area* and *finite-velocity* jet with a *zero-area* and *infinite-velocity* ideal jet, both carrying the same kinematic momentum, the center-line velocity of the jet at a distance g from the slit, where our forcing is maximum, is

$$u = \frac{3}{8\pi\nu g}\frac{\Phi_{inj}^2}{\mathrm{S}_{\mathrm{inj}}}. \tag{4.16}$$

The *injection amplitude* $\mathcal{A}$ defined in HJM is given by the ratio between the total massflow injected through the N_{inj} slits and the pipe massflow upon injection,

$$\mathcal{A} = N_{\mathrm{inj}}\frac{\Phi_{\mathrm{inj}}}{\Phi_{\mathrm{pipe}}}. \tag{4.17}$$

The pipe massflow can be exactly derived from the actual Reynolds number, Re_a, in the experiments, or, equivalently, from the nominal Reynolds number before injection. In our computations, the pipe massflow evolves, but, provided that the injection duration is kept short, it can be considered that of the initially unperturbed Hagen-Poiseuille flow, so that it can be expressed in terms of the nominal Reynolds number, Re, as

$$\Phi_{\mathrm{pipe}} = \frac{\pi\nu a}{2}Re. \tag{4.18}$$

Using equations (4.16) and (4.18), the injection amplitude defined in (4.17) can be expressed in terms of the speed of the jet and the nominal Reynolds number,

$$\mathcal{A} = N_{\text{inj}} \left(\frac{32}{3} g^* \mathrm{S}^*_{\text{inj}} \right)^{1/2} \left(\frac{u^*}{Re} \right)^{1/2}, \tag{4.19}$$

where $g^* = g/a$, $\mathrm{S}^*_{\text{inj}} = \mathrm{S}_{\text{inj}}/\pi a^2$ and $u^* = u/\mathrm{U}_{\text{cl}}$ are dimensionless quantities measuring the distance from the slit, its cross-sectional area and the jet speed, respectively. It should be reminded that u^* appearing in (4.19) *is not* the velocity of the flow at the chosen point projected on the jet axis direction (which we shall call u_g), but the velocity at that point of the jet itself, the effects of which we are trying to model using a forcing field. While we have access to the former, we infer the latter by assuming that they become the same as the effects of the forcing saturate and the velocity at this point approaches an asymptotic value.

Different jet-penetration scenarios have been suggested [71] recently in order to adjust upper and lower bounds for the threshold exponent γ appearing in (4.1). To the authors' knowledge, equation (4.19) provides a first quantitative approximation to a law relating an injection property that is mensurable in under-resolved (to be affordable) computations and the experimental amplitude. There are other factors appearing in (4.19) that are associated with geometrical features of the slit. As mentioned before, current computational power limitations makes accurate representation of the slits not feasible. As a result, the *coarse* discretisation used in this study may lead to discrepancies due to geometrical differences between the numerically modelled and the actual experimental injections. Nevertheless, we expect to qualitatively mimic the experimental behaviour of the injection save for a scaling factor to do with geometrical discrepancies and non-ideality of the jets.

4.2 Effects on transition of injection duration

The effect of the injection lapse on transition has been extensively tested experimentally in HJM and it has been found that, although increasing the duration of the injection at a given Reynolds number reduces the critical amplitude, this reduction eventually stagnates. As a result, the critical amplitude does not depend on the injection duration, provided that it becomes sufficiently long-lasting. Experimentally, it has been observed that the critical amplitude is not altered for injection durations of $\Delta t_{\text{inj}} \gtrsim \Delta t_0 = 24$ advective time units, where Δt_0 will be considered later as a reference time interval for amplitude renormalisation purposes. This behaviour should also be reproduced numerically for the simulations to be considered reliable.

Following HJM, we proceed to validate the computational model of the injection and the scaling law provided in (4.19) by simulating different injection amplitudes and injection lapses at $Re = 4000$. For a given injection lapse, Δt_{inj}, the amplitude factor f_a is increased until transition is obtained. A computational run is considered turbulent when chaotic dynamics have taken over the full domain and persist after 600 advective time units. Laminar runs, instead, are characterised by the eventual viscous decay of the injected perturbation after an initial transient growth.

A single run has been performed for each value of the amplitude factor. No probabilistic behaviour was observed or expected near criticality, even at the low Re-range. The fact that the same exact perturbation (forcing) was scaled up and down, with no random component added on top, may be responsible for the deterministic behaviour observed in the vicinity of the critical threshold. We would have expected probabilistic transition, had we randomly modified the forcing shape or imposed a random initial condition, so that the amplitude was no longer the only difference from run to run. Furthermore, the critical threshold has *o*nly been resolved within a 2.5% accuracy, which is far beyond what is needed to determine the critical amplitude threshold trends, and the probabilistic behaviour may well be confined within this error, especially as Re is increased.

Once the critical forcing amplitude is known, we proceed to compute the asymptotic value u^* of the jet by re-starting the same critical run but with the forcing permanently on so that the flow jetwise speed at the chosen location on the jet axis, $u_g(t)$, has enough time to stagnate to its asymptotic value, which we identify as u^*. This recomputation is mandatory for example in the case of very short injections, where the forcing stops before the monitored flow speed has achieved an asymptotic value.

Figure 4.3a shows the flow speed $u_g(t)$ measured at the point of maximum forcing norm for different critical runs carried out for $\Delta t_{\text{inj}} = 2, 3, 4, 5, 8$ and 16 time units. On each of these curves the forcing was stopped at the indicated instants of time (gray circles), critically leading to transition for longer times (not shown). Figure 4.3a also shows the behaviour of the flow speed for the same runs, but with permanent forcing (dashed curves). It can be observed that there is a clear stagnation of u_g to a constant value u^* in some cases. The curve for $\Delta t_{\text{inj}} = 2$ exhibits some irregularities due to the fact that very large amplitudes are needed to lead to transition for short injections and therefore turbulence sets in before the asymptotic value of the jet speed is reached. However it is easy to obtain a sharp asymptotic value u^* for most of the injections, so that this value can be used afterwards in relation (4.19) to identify its corresponding amplitude $\mathcal{A}$.

In order to make a consistent comparison between numerics and experiments, we define

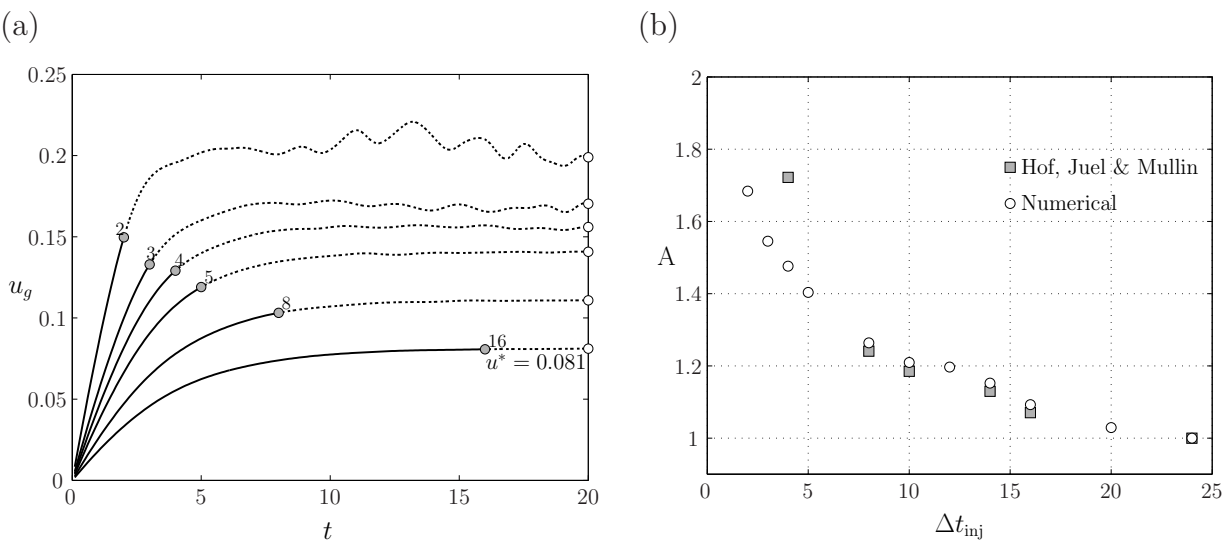

Figure 4.3: (a) Jet speed, u_g, measured at the point of maximum forcing norm as a function of time for different injection lapses $\Delta t_{\text{inj}} = 2, 3, 4, 5, 8$ and 16 (solid curve ended with gray circles) with $Re = 4000$. The re-run for the same critical amplitude but with permanent forcing are represented to show the asymptotic behaviour of u_g (dashed curves) and their saturation values u^*. (b) Normalised threshold amplitudes from Hof, Juel & Mullin [27] experiments (gray squares) and current computations (white circles) with $Re = 4000$.

the *normalised amplitude* of a Δt_{inj}-lapse perturbation as

$$\mathrm{A}(\Delta t_{\text{inj}}) = \frac{\mathcal{A}(\Delta t_{\text{inj}})}{\mathcal{A}(\Delta t_0)}. \tag{4.20}$$

Therefore, the experimental and numerical threshold amplitudes are normalised *independently* with respect to their corresponding reference saturation values for $\Delta t_0 = 24$ advective time units. With this renormalisation, the critical amplitudes become independent of the injection geometrical features appearing in (4.19) and comparison is rendered possible. Table 4.1 summarises the saturation values u^* obtained from the computations and their corresponding amplitudes according to (4.19) and (4.20), $\mathcal{A}_{\text{num}}$ and A_{num}, respectively. Table 4.1 also contains the experimental data, $\mathcal{A}_{\text{exp}}$, originally extracted from Figure 3 of HJM [27] and normalised, A_{exp}, according to (4.20). Figure 4.3b shows the normalised threshold amplitudes A_{exp} and A_{num} for different injection lapses. The agreement is very good, particularly for $\Delta t_{\text{inj}} > 8$. Nevertheless, there is some discrepancy for short injections, $\Delta t_{\text{inj}} = 2$. As explained before, short injections require a larger forcing, thus triggering transition before an asymptotic value of u^* is identified (see Fig. 4.3a) to be used in the

Δt_{inj}	u^*	$\mathcal{A}_{\text{num}} \times 10^3$	$\mathcal{A}_{\text{exp}} \times 10^3$	A_{num}	A_{exp}
4.0	0.157	1.495	6.167	1.48	1.72
8.0	0.112	1.280	4.443	1.26	1.24
10.0	0.100	1.225	4.244	1.21	1.19
14.0	0.090	1.167	4.045	1.15	1.13
16.0	0.081	1.106	3.834	1.09	1.07
24.0	0.068	1.013	3.581	1.00	1.00

Table 4.1: Computed threshold amplitudes $\mathcal{A}_{\text{num}}$, based on numerical measurement of u^*, for comparison with those corresponding to the experiments by Hof, Juel & Mullin [27], $\mathcal{A}_{\text{exp}}$. The quantities appearing in the last two rows are the normalised amplitudes according to equation (4.20).

renormalisation. Furthermore, the forcing field has not been tuned to accomodate the large penetration expected from the large amplitude injections required to trigger transition for low Δt_{inj}. Also the fact that the experimental injection effective time is somewhat shorter than the prescribed perturbation time (more significantly, the shorter the injection is), due to the finite rise and decay times of the experimental boxcar signal, may account for the discrepancy.

The same sort of analysis was carried out in HJM for $Re = 2170$, obtaining equivalent results regarding the stagnation of $\mathcal{A}_{\text{exp}}$ for long injection lapses. The experiment at this lower Re could not be reproduced numerically as it was found very difficult to obtain sustained transition below $Re = 2800$. Sustained turbulence appeared extremely sensitive to environmental noise at the low Re-range, in agreement with what was already pointed out by Reynolds [58] in the past. This was ascertained by increasing the numerical noise at random for different runs, which eased transition but still thwarted any possibility of repeating the injection-lapse analysis at low Re. The incapability of the numerical model to reproduce sustained turbulent motion at $Re \lesssim 2800$ can be ascribed to the pressure-driven nature of the problem, an issue that will be addressed later on, as well as to the significance of the perturbation exact shape [24].

4.3 Transition due to a localised impulsive injection

The transition process triggered by a localised impulsive injection will be exemplified with a thorough analysis of a single critical run at $Re = 4000$. A very structured and regular disturbance is locally enforced during an injection lapse of $\Delta t_{\text{inj}} = 20$ advective time units.

The perturbed portion of fluid at injection withdrawal will nevertheless be much shorter than Δt_{inj}-radii, and, tipically, even shorter than $\Lambda/4$. Even though the injection lasts long, only the near-wall region is affected by a forcing representing very oblique jets. In this region, the streamwise advection due to the basic flow is slow and, therefore, the perturbed length remains short. This is clearly shown in Fig. 4.4a, where the azimuthal vorticity of the disturbance velocity, $(\nabla \times \mathbf{u})_\theta$, is plotted precisely at the end of the injection lapse $t = \Delta t_{\text{inj}} = 20$. Also plotted is a 3D view of a couple of axial vorticity iso-surfaces at $(\nabla \times \mathbf{u})_z = \pm 0.3$, which give a clearer view of the size of the perturbed patch as well as of its laminar or turbulent nature.

Once the injection has ceased, the perturbed patch of flow stretches and deforms as it is advected downstream. The patch follows a cyclic evolution by which it grows and then splits in three sections: front, central and rear. The front and rear sections of the perturbed region travel faster and slower than the central section, respectively, as they die away. Meanwhile, the central region starts stretching again and the whole cycle is repeated. As a result, the length of the perturbed region can be considered to oscillate around a fairly constant value, albeit only transiently while laminarity is preserved. Figure 4.4b shows the perturbation immediately after it first breaks into three smaller patches. In Fig. 4.4c, the front and rear sections of the patch can be seen fading out as they depart from the central section position. What brings this cyclic behavior to an end is the appearance of turbulent motion within the perturbed region. The patch starts losing its laminarity and breaks into turbulent bursts. At first, the turbulent bursts relaminarise at the front and back of the perturbed structure, but soon the core of the perturbed region becomes turbulent and starts growing monotonically. Figure 4.4d, shows the perturbation once it has become fully turbulent and is growing fast. From this point on, the trailing edge starts to abruptly decelerate while the leading edge accelerates, rapidly polluting the whole computational domain through axial periodicity reinfection. In experiments, the whole pipe would have transitioned downstream from the axial location where the trailing edge finally settles.

The local growth of the trailing and leading interfaces of the turbulent patch have been monitored during the last stages of the transition, before the turbulent structure pollutes the whole computational domain due to the artificially imposed axial periodic boundary conditions. The root-mean-square (r.m.s.) of the fluctuation of the axial velocity disturbance, $\langle u_z \rangle_{\text{rms}}$, has been computed by taking an average over the azimuthal coordinate, and then further averaged along the radius to produce a quantity representative of the turbulence level and only depending on the axial coordinate. In Fig. 4.5, the axial positions with $\langle u_z \rangle^2_{\text{rms}} \geq 0.5\%(\text{U}_{\text{cl}}/2)^2$ have been represented with black dots for $t \in [175, 205]$, evidencing the turbulent patch length evolution as a function of time. Linear regression analyses have

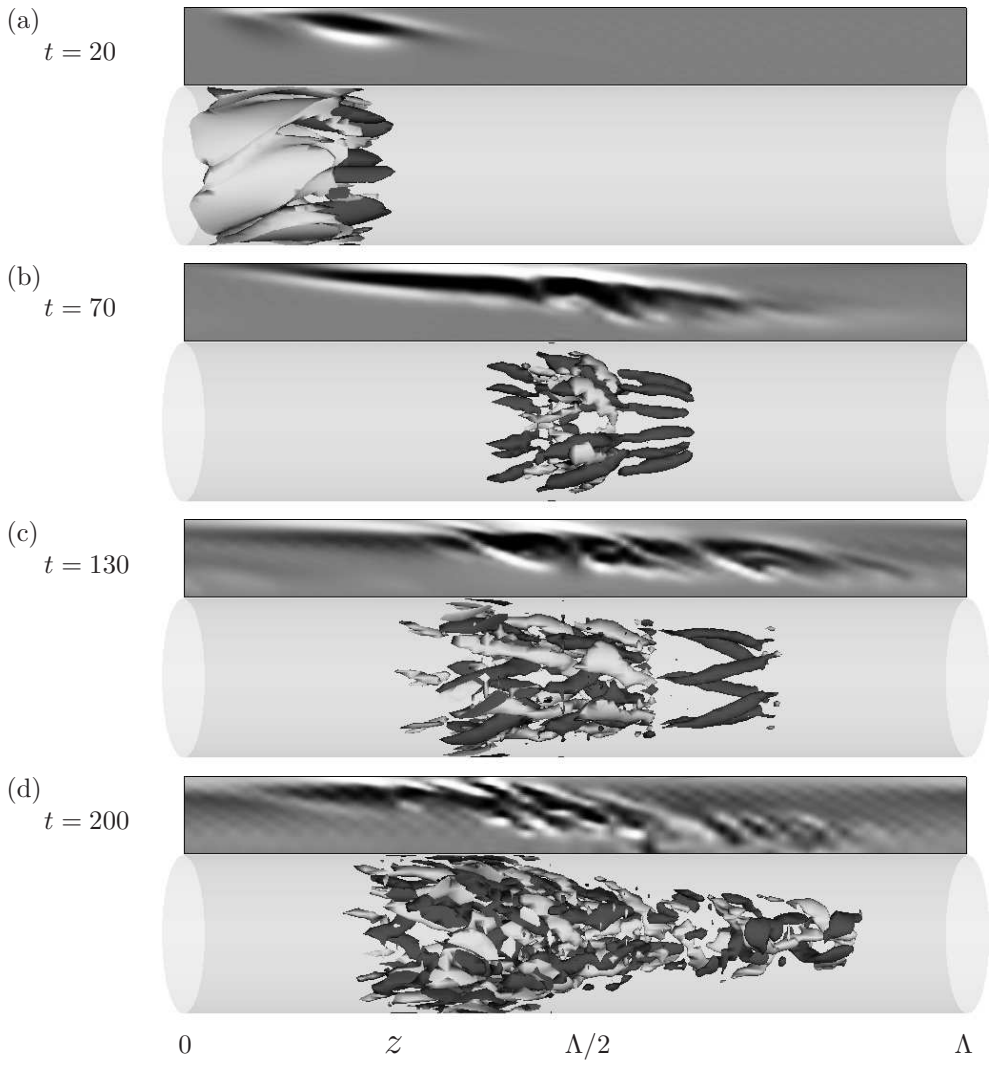

Figure 4.4: Critical run at $Re = 4000$, with $\Delta t_{\text{inj}} = 20$. Each snapshot depicts azimuthal vorticity contours, $(\nabla \times \mathbf{u})_\theta$, of the perturbation field (basic flow removed) on top of a 3D view of a couple of axial vorticity iso-surfaces at $(\nabla \times \mathbf{u})_z = \pm 0.3$. The pictures correspond to $t = 20, 70, 130$ and 200, and have been taken from a viewpoint travelling downstream at the same speed as the perturbation.

been performed with the first and last point defining the leading (LE) and trailing (TE) edges of the perturbation, respectively. The results have been plotted in Fig. 4.5 as dashed lines. The slope of these lines represents the propagation velocity of the leading and trailing edges, which happen to be $c_{\text{LE}} = 0.754 U_{\text{cl}}$ and $c_{\text{TE}} = 0.325 U_{\text{cl}}$, respectively. Taking into account that $Re_a \simeq 3850$ during the period we measure these speeds we can express them in terms of the mean flow velocity as $c_{\text{LE}} = 1.567 \bar{U}$ and $c_{\text{TE}} = 0.675 \bar{U}$, which is in

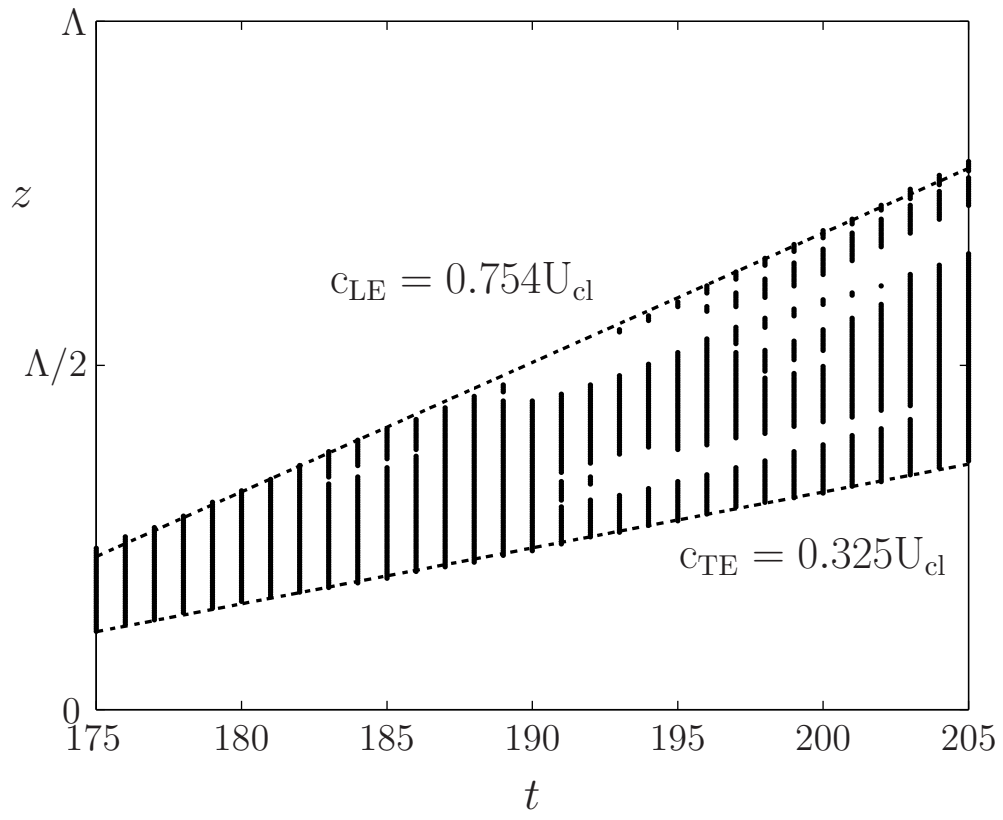

Figure 4.5: Growth of the turbulent patch as it is advected downstream. Black dots represent points fulfilling the criterion that $\langle u_z \rangle^2_{\mathrm{rms}} \geq 0.5\%(U_{cl}/2)^2$. Dashed lines show the position of the trailing and leading edges as a function of time.

reasonable agreement with experimental results for turbulent slugs [80]. We can therefore conclude that the numerically observed turbulent structure closely resembles a *slug*. Beyond the times plotted, the leading edge velocity sharply increases, but this is probably due to the fact that the actual size of the perturbed region is comparable to the size of the pipe and the leading and trailing interfaces artificially interact due to the periodic boundary conditions, the infinite pipe no longer being properly represented.

Overall, the transition process which takes the flow from the laminar to the turbulent state is clearly catastrophic, in agreement with what is generally observed in the experiments [11]. Therefore, it is not a trivial task to identify a simple instability mechanism from the numerical computations, in contrast with former numerical studies [38] based on particular streamwise transition scenarios.

4.4 Critical amplitude threshold for injected perturbations

It has been experimentally shown [27] and computationally verified in §4.2 that the critical amplitude of an injection triggering transition does not depend on the injection duration for $\Delta t_{\text{inj}} \geq 24$ advective time units. Nonetheless, it can be considered to have reasonably settled down for $\Delta t_{\text{inj}} \geq 20$. It is therefore convenient to explore the critical amplitude threshold using this lower $\Delta t_{\text{inj}} = 20$, so that the perturbed length is as much shorter than the pipe length as possible to avoid reinfection due to axial periodicity, at least within the injection lifetime.

The critical amplitude threshold has been systematically tracked for Reynolds numbers in the range $Re \in [2512, 14125]$ and the injection duration held fixed to $\Delta t_{\text{inj}} = 20$ in all the explorations. The amplitude calculation is completely analogous to the one described in §4.2 and the same criteria used to distinguish laminar from turbulent runs are retained. The geometrical discrepancies between experiments and the actually modelled injection, along with the extreme idealisation of the jets, demand a normalisation of the experimental and numerical thresholds so that they become comparable. In what follows, we normalise the amplitudes according to

$$\mathrm{A}(Re) = \frac{\mathcal{A}(Re)}{\mathcal{A}(Re_0)}. \tag{4.21}$$

where Re is the Reynolds number (actual and nominal confounded) of the basic flow before being perturbed and $Re_0 = 14000$.

The critical amplitude threshold results are shown in Fig. 4.6. The amplitude A, normalised according to (4.21), has been plotted as a function of Re for both experiments (gray squares) and computations (white circles), along with a dashed line indicating a slope of $\gamma = -1$. It is remarkable how experiments and computations exhibit very similar behaviour at high Re, which seems to evidence that the numerical model properly captures the transition mechanisms observed in the laboratory. The doubled axial-resolution check-runs at high Re have also been plotted (black dots), with no significant change in the critical threshold slope, which reassures us that the resolution chosen for the bulk of the computations is sufficient. At the low Re-range, however, while experiments exhibit the same characteristic asymptotic behaviour from Re values as low as 2000, the computations fail to do so. In fact, the numerical simulations seem to find a vertical stability threshold for $Re \sim 2500$, at least for the type of perturbations used. This discrepancy can be ascribed to several apparent differences between experiments and computations.

A first difference has to do with the topological modelisation of the injection. As Re is reduced, the critical amplitude of the forcing required to trigger transition increases. For

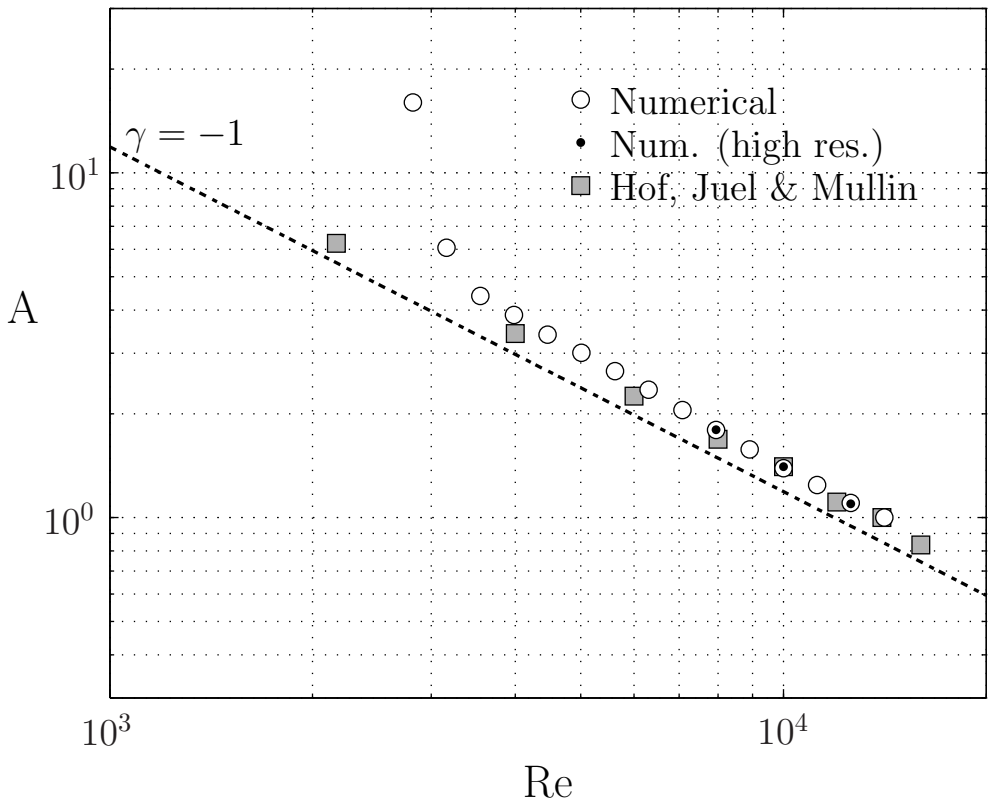

Figure 4.6: Experimental (gray squares) and computational (white circles) critical amplitude thresholds. The high resolution (doubled count of axial mesh-points) critical threshold check-runs at high Re have also been represented (black dots). All sets of values have been normalised independently with respect to their extrapolated critical amplitudes at $Re = 14000$.

consistency, the computational forcing field modeling the injection has been held fixed and merely scaled up until transition is obtained. However, in the laboratory, increasing the injection amplitude not only scales up the induced acceleration field, but it also may modify the topological features of the resulting jet, such as its penetration or effective width. The forcing field chosen seems to be as effective as the experimental one for moderate and large Re, but not so much so for low Re. However, we believe this could explain a slight deviation, but not the spectacular discrepancy observed at very low Re.

The main difference, however, concerns the constant-massflow and pressure-driven different nature of the experimental and the computational pipes, respectively. As the perturbation grows and reorganises the flow, the actual Reynolds Re_a has a tendency to drop. Especially in short pipes, where intermittency phenomena may fill a high portion of the pipe length. In the constant-massflow experiments of HJM, some energy may be restituted

into the flow through the action of a constant-speed piston, so that Re_a is held constant. In the extreme case of transition, the piston is forced to pull harder in order to restitute the enormous amount of energy dissipated due to turbulence and keep the massflow constant. By contrast, the numerical simulation lets Re_a evolve freely. As a consequence, by the time the perturbation has grown and transition becomes probable, Re_a may be much lower than originally, rendering the experimentally calculated critical amplitude threshold not generally applicable to our simulations, since it is not immediately apparent which value of Re_a (initial, transitional or averaged) should be used for a consistent comparison. This difficulty in choosing when to measure Re_a is in fact disclosing a more profound hindrance, namely that the discrepancy stems from the fact that the problems being solved are indeed different. Fortunately, this effect, which is dominant at low Re for the pipe length considered, becomes less decisive as Re is increased, which indicates that both problems tend to become equivalent. This is clearly evidenced in Fig. 4.7, where the transient drop of Re_a relative to its initial value, the nominal Re, is followed in time for injection amplitudes that are just subcritical. It is clear that Re_a suffers a transient remarkable drop for low-Re runs

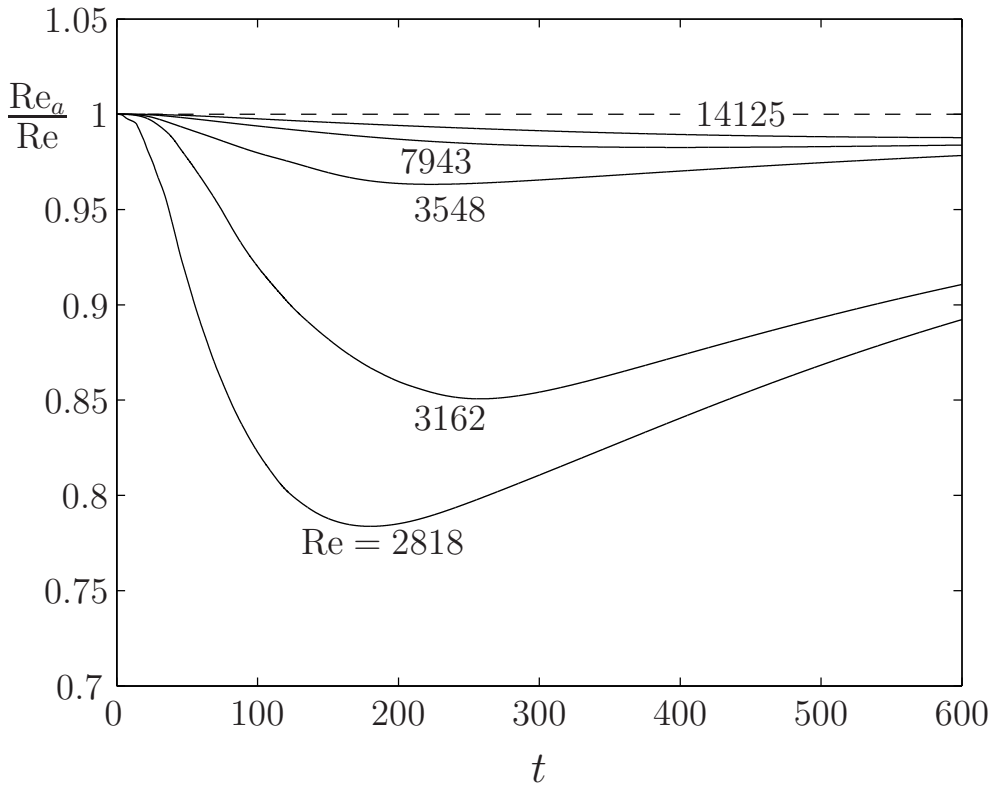

Figure 4.7: Relative transient drop of Re_a for slightly subcritical injections (less than 2.5% under criticality) at different values of nominal Re, indicated next to each of the corresponding curves.

(over a 20% at $Re = 2818$), while at high Re it remains much more stable (less than 2% drop at $Re = 14125$). The significant drop makes it futile to reproduce the critical amplitude threshold behaviour at low Re, while comparison with experiments becomes reasonable as Re is increased. To further support this view, and thus validate the obtained asymptotic exponent for the critical threshold, this latter has been recomputed for $Re >= 7943$ with a constant mass-flux version of the code. The pressure-driven results are mimicked with pinpoint accuracy, at least within the 2.5% resolution with which the threshold has been computed. Transition at very low Re in pressure-driven pipes causes a considerable drop in Re_a when the full domain becomes turbulent (down to as low as $Re_a \sim 1800$ from an initial $Re = 2500$, for instance). Turbulence has a very short lifetime at this very low Re_a and relaminarisation naturally occurs well before our time-horizon is attained [20, 28].

4.5 Conclusions

The effects of the impulsive perturbative system recurrently used in pipe flow experiments have been succesfully modelled via a time-dependent volume forcing in numerical computations. The axisymmetric jet theory has been used to define a perturbation amplitude equivalent to the one used in the aforementioned experiments.

An extensive study of the critical amplitude of the impulsive injections that are capable of triggering transition as a function of their time-duration has been carried out at $Re = 4000$ and very good agreement with experimental results has been obtained. As in the experiments, the critical amplitude has been shown to decrease with the injection duration to end up stagnating at a constant value for $\Delta t_{\text{inj}} \geq 24$ advective time units.

The evolution of injected perturbations has been monitored with detail in order to capture the main features of a turbulent patch for $Re = 4000$. Numerical computations reproduce quite well the generation of laminar-turbulent intermittency dynamics observed in former experimental studies. This is evidenced by monitoring the speed of the trailing and leading interfaces of the generated turbulent slug, which are found to be roughly the same as the ones measured in the laboratory. However, the length of the computational pipe domain and the assumption of periodic boundary conditions makes it impossible to study the evolution of the slug for longer times, due to the numerical interaction between the trailing and leading interfaces.

The critical amplitude threshold has been systematically tracked for Reynolds numbers within the range $Re \in [2512, 14125]$. The explorations have been carried out always taking

$\Delta t_{\text{inj}} = 20$, for which the critical amplitude can be considered to have almost settled down to its asymptotic value. Very good agreement with experiments has been obtained at the high-end of Reynolds numbers, where the exponential scaling $A \sim Re^{-1}$ has been clearly evidenced. By contrast, the apparent discrepancy at low Reynolds numbers is ascribed to the different behaviour of pressure-driven and constant-massflow pipes of finite length and also to the nature of the injection numerical model, whose topological structure has been held fixed in all simulations. In addition, the massflow transient drop as the perturbation develops within the flow at low Re may explain why the computational pressure-driven pipe seems more robust to perturbations and does not exhibit transition for $Re \lesssim 2800$. However, this transient drop is shown to lose transcendency as the Reynolds number is increased, thus favoring a better asymptotic agreement between our moderate-length pressure-driven computational pipe and the long constant-massflow experimental pipe. Some computations at high Re with a constant-massflow version of the code substantiate this good agreement.

CHAPTER 5

GENERAL SEARCH OF TRAVELLING WAVES

A very recent approach to cast light on both subcritical transition and turbulent dynamics in shear flows, has aimed at a direct exploration of the phase space of the dynamical system representing the problem. Stationary and travelling-wave solutions have been identified in wall-bounded shear flows such as plane Couette [47, 74, 76, 77] and plane Poiseuille flow [75, 76]. Their involvement in turbulent dynamics or even in transition seems to be of foremost importance [77]. Until very recently, the Hagen-Poiseuille basic flow was the only known simple solution to pipe flow. In the past few years, however, a number of travelling wave solutions have been identified [19, 78, 55], and their presence in turbulent flow positively ascertained [26]. Traces of coherence (periodicity), presumably ascribed to these travelling waves, have also been observed in decaying turbulence [53]. These solutions are unstable and disconnected from the basic flow, which renders the task of computing them utterly complex and in no way accessible by mere time integration.

This chapter is structured as follows. Section §5.1 is devoted to the mathematical formulation of the problem of searching for travelling wave solutions. The design of the initial guess to converge onto these types of solutions is addressed in section §5.2. Section §5.3 yields the main results of the search, showing the main features of the solutions found. An outline of a method for finding relative periodic orbits as a next step in complexity is sketched in section §5.4. Finally, the main conclusions are gathered and presented in section §5.5.

5.1 Travelling waves search method

Since the flow through a pipe has, due to the pressure gradient boundary conditions between inlet and outlet, a broken fore-aft symmetry, it does not admit streamwise-dependent steady solutions of any type. The simplest solutions compatible with the Navier-Stokes equations in a pipe geometry with this type of boundary conditions take therefore the form of travelling waves, which become stationary solutions if we place ourselves in a comoving reference frame. A general method to find such solutions would be the search of fixed points of the Poincaré map [17, 30, 72]. This approach would allow to compute periodic solutions of any sort and, in particular, travelling wave solutions, but at the cost of requiring a complete integration over a period every time a crossing of the Poincaré section was needed, namely at every Newton step performed on the Poincaré application, with the computing effort

involved.

A much more sensible approach, and the one chosen in the present work, consists of looking for stationary solutions in a comoving reference frame travelling at the speed of the travelling wave [16, 19, 78].

A general solution to the Navier-Stokes equations must satisfy the ODE system described in chapter 2:

$$\mathbb{A}\,\dot{a} = \mathbb{B}\,a - b(a,a) + fF, \tag{5.1}$$

where F is a volume forcing and f a scaling factor, the use of which will be described later.

Here we are looking for solutions that are stationary in an adequate reference frame, moving downstream at the travelling wave phase speed. These solutions satisfy, in phisical space,

$$\mathbf{u}(r,\theta,z+c\,t,t) = \mathbf{u}(r,\theta,z,0), \tag{5.2}$$

where c is the a priori unknown travelling wave phase speed. The Fourier-Chebyshev coefficients resulting from the Galerkin projection must satisfy:

$$a^{(s)}_{lnm}(t) = a_{tw}\,\mathrm{e}^{-\mathrm{i}klct}, \tag{5.3}$$

where a_{tw} is nothing but the spacial structure of the travelling wave. Substituting the expression (5.3) in the equation (5.1) and simplifying the exponential terms that appear throughout, we end up with an implicit system of equations that the spatial structure must satisfy:

$$-\mathrm{i}klc\,\mathbb{A}\,a_{tw} = \mathbb{B}\,a_{tw} - b(a_{tw},a_{tw}) + fF, \tag{5.4}$$

where the volume forcing term F is taken as streamwise independent or, in the worst of cases, assumed to travel downstream with the travelling wave phase speed. The scalar coefficient f appearing in (5.4) is a forcing factor to allow for a continuation process aimed at removing the forcing, whenever an homotopy transformation of the problem has been used to track the travelling wave solutions. The resulting system of equations is then preconditioned with the inverse of the matrix $\mathbb{B}$ (usually called Stokes preconditioning), which is approximately the inverse of the diffusion operator, and has been proven a good preconditioner of the Navier-Stokes equations [36]. We end up designing a Newton solver looking for zeroes of the vector function

$$\mathrm{F}(a,c) = a + \mathbb{B}^{-1}(\mathrm{i}klc\mathbb{A}\,a - b(a,a) + fF). \tag{5.5}$$

In order to allow for the extra unknown represented by the phase speed c, an additional equation is needed. The natural choice is an equation fixing the phase of any streamwise

dependent coefficient, so the axial degeneracy of the solution (a continuum of solutions related by an arbitrary axial shift exist) is accounted for.

Equation (5.5) will lead to travelling wave solutions preserving the same axial pressure gradient as the initial guess. Travelling waves are nothing but rigid structures characterised by constant speed downstream advection, with no axial pressure gradient or massflux variations in time. They admit two equivalent representations, one within the pressure-driven pipe frame, another subject to the constant massflux pipe description. The method just described lies within the pressure-driven pipe frame. In some cases, however, it may be useful to look for travelling wave solutions preserving the initial guess massflux. This is the case of Re continuations aimed at unfolding a whole branch of solutions or direct search of travelling waves underlying a constant-massflux time evolution. In such cases, equations (5.4) and (5.5) can be easily adapted to preserve massflux. An additional forcing term $\mathrm{C}f_{cm}$, representing the bulk axial pressure gradient required to preserve the basic flow massflux, must be added. To account for the new unknown f_{cm}, a new equation enforcing that the perturbation a has no contribution to the total massflux, must be added: $Q(a) = 0$. Distinction will be made throughout between two different Reynolds numbers, Re and Re_a, the first one associated to the pressure-driven description, the second one to the constant massflux description, as was already addressed in chapter 4. Associated to the two different descriptions, two different definitions of the travelling wave phase speed arise. Whereas c appearing in 5.3 is related to the pressure-driven description, a travelling wave phase speed based on the constant massflux description, c_a, nondimensionalised with the mean axial velocity, can also be defined, the relationship between the two being $c_a = 2c\ (Re/Re_a)$.

Two versions of the Newton solver were implemented. First, a direct Newton solver, with very good convergency properties as long as the initial guess is close to the solution sought, i.e. within the Newton solver convergency basin. The linear system produced at each Newton step is solved using iterative *Krylov*-subspace methods such as GMRES. In applications for which the initial guess could not be ensured to be close to the solution, an enhanced convergency region was required. For these cases a *damped* Newton method was implemented.

5.2 Generation of an initial guess

The basic flow constitutes the most simple travelling wave and, as such, is a solution of equation (5.4). This trivial solution has therefore its own basin of attraction for the Newton solver and would capture most of the initial guesses used whenever they do not fall within

the basin of attraction of other travelling wave solutions. Consequently, choosing right initial guesses is not a trivial task. We have followed to independent approaches to the task of producing good initial guesses, one based on an homotopy transformation of the problem using a carefully chosen volume forcing term, the other lying on wandering $v$isits to the vicinity of travelling wave solutions along fully $3d$ time evolutions.

5.2.1 Homotopy transformation using a volume forcing term

A first approach to generate appropriate initial guesses is to assume a certain topology compatible with the existence of a travelling wave solution. This is precisely the way in which the first families of exact coherent travelling states were found in pipe flow [19, 78, 55] and the one we chose to, at the same time, test the method and find the already found states.

The philosophy behind the method consists in assuming the self-sustained process initially devised to explain turbulence [3, 73] as the underlying mechanism behind the travelling wave subsistence. The mechanism assumes a strong vortical structure that induces streaks to which 3D waves are unstable that nonlinearly interact feeding back the original vortices. The approach to produce a good guess from where to converge onto the travelling wave consists in enforcing a vortical structure using the forcing term F in equation (5.4). Within a certain range of Re and forcing amplitude f, a stable forced travelling wave solution, disconnected from the basic flow, is born from a saddle node bifurcation. Because it is stable, it can be easily computed by simple time evolution. The forced travelling wave obtained can be converged as much as desired with the Newton solver and then a continuation process to remove the forcing occasionally ends up producing the sought travelling wave.

The travelling wave selected very much depends on the forcing topology. The forcings employed to find the first identified families of travelling waves were based on solutions of the Stokes operator in a circular domain corresponding to different numbers of pairs of rolls. Volume forcings linearly enforcing 2, 3, 4, 5 and 6 pairs of rolls produced travelling wave solutions with 2, 3, 4, 5 and 6-fold azimuthal periodicity, respectively.

To recompute the already pinpointed travelling waves [19, 78], streamwise-independent vortical structures with the azimuthal topology of the travelling waves sought were designed.

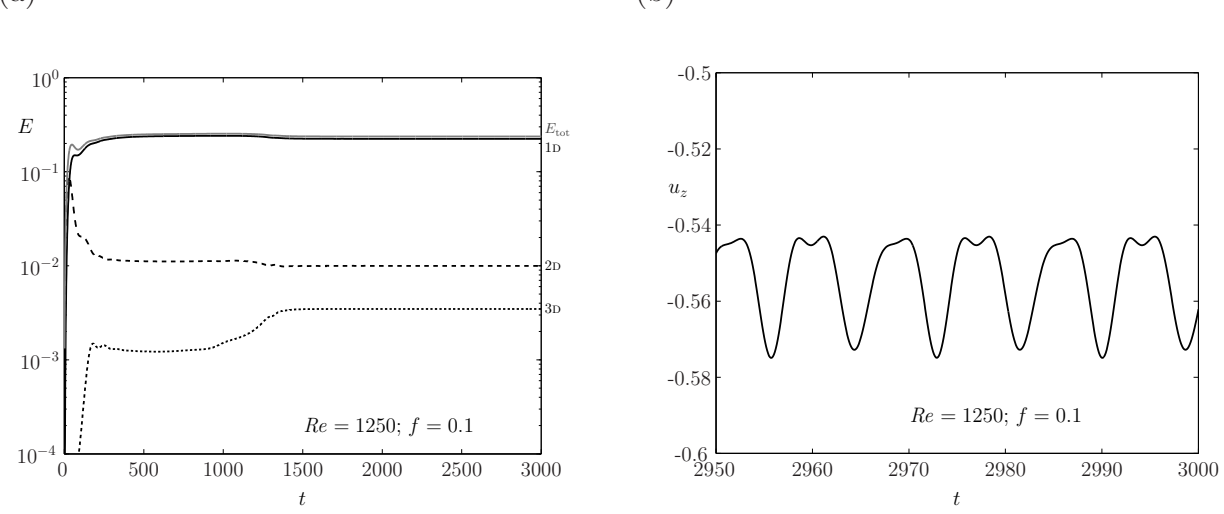

Figure 5.1: $C2$ forced travelling wave converged through time evolution at $Re = 1250$ with $f = 0.1$. a) 1D, 2D, 3D and total energy signals. b) u_z at a point of the pipe axis corresponding to a pretty much converged travelling wave.

We chose the simplest vortical structures compatible with our pipe representation:

$$a_{n_0} = a^{(s)}_{lnm} = \begin{cases} 1 & (l, n, m; s) = (0, \pm n_0, 0; 1) \\ 0 & \text{elsewhere} \end{cases} , \tag{5.6}$$

with n_0 the number of pairs of rolls. The forcing is then chosen so that it linearly enforces this solution:

$$F = -\mathbb{B}\, a_{n_0}. \tag{5.7}$$

By construction, a streamwise-independent stationary solution will exist as a simple homotopic transformation of the basic flow due to the presence of the forcing term. However, within a certain range of Re and f, this solution becomes unstable and a stable streamwise-dependent forced travelling wave bifurcates locally, from the new forced streamwise-independent steady solution. This state we find through time evolution. Figure 5.1 shows an example of a forced travelling wave with 2-fold azimuthal symmetry ($n_0 = 2$, what we dub as a $C2$ travelling wave). The convergence towards a constant energy solution, as can be seen in Fig. 5.1a, seems to indicate that a stationary solution or a travelling wave is being approached asymptotically. The fact that the solution approached is nothing but a travelling wave is clearly confirmed by Fig. 5.1b, where the periodic behaviour of u_z at a given point in the pipe axis removes all doubt.

This forced travelling wave we then converge to the desired precision using the Newton solver.

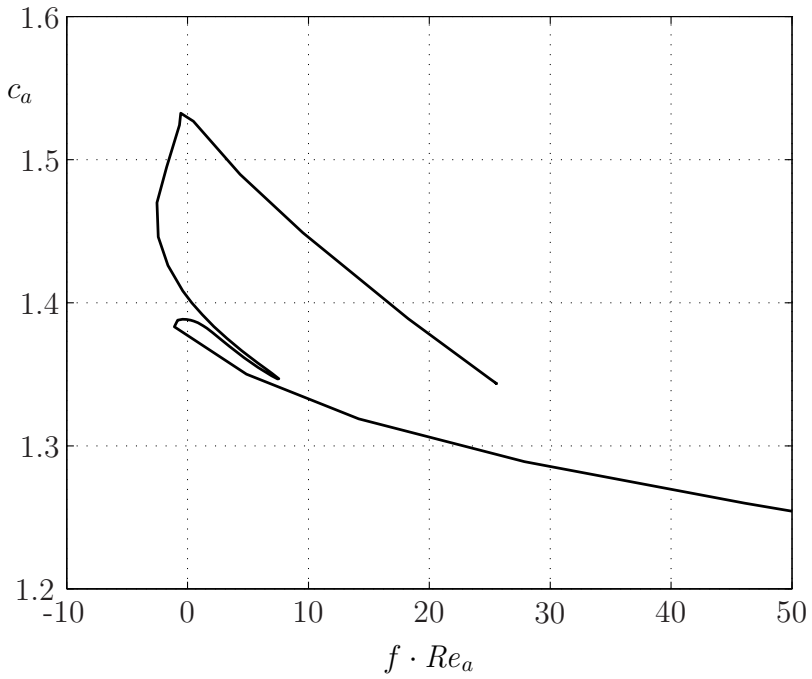

Figure 5.2: Forcing removal continuation process for a $C2$ forced travelling wave. Plotted is the travelling wave phase speed c against $f \cdot Re_a$. The portion of the process shown corresponds to variations of f at $Re = 2200$, where the intersections with the $(f \cdot Re_a = 0)$-axis correspond to unforced travelling wave solutions.

The last step to converge unto a travelling wave which is a solution of the unforced Navier-Stokes equations is to follow a continuation process in order to remove the forcing. This continuation process is not trivial and the forcing removal is not monotonical. A combined f and Re continuation is required since the solution sought may not necessarily exist within the same exact Re-range as its forced counterpart. In this continuation process, whenever the forcing factor crosses the $f = 0$ axis, an unforced travelling wave has been found that can be later continued in Re to unfold a full family of solutions with the prescribed topology. As an example, a detail of such continuation process has been plotted in Fig. 5.2.

5.2.2 Initial guesses from time evolution

A second approach to produce good initial guesses for the Newton solver consists in monitoring the Newton residual along time evolving runs. Whenever a significant drop of the residual is observed, there exists the possibility that the trajectory might have approached

a travelling wave solution. If there is a neighbouring travelling wave, the Newton solver may be able to converge it.

This method could be used in a fully turbulent run to try and identify visits to travelling wave solutions underlying the turbulent dynamics. This we haven't attempted to do due to the extremely high resolution necessary to properly simulate turbulent runs. Other trajectories that are good candidates to experience visits to all sorts of simple states, among which travelling waves, are the edge or critical trajectories. Because of their particular interest in transisition understanding, we will focus on these trajectories later in chapter 6.

5.3 Azimuthal discrete symmetric travelling waves

Following the method decribed in section 5.2.1, the $C2$, $C3$, $C4$ and $C5$ travelling wave solutions already found in Faisst & Eckhardt [19], Wedin & Kerswell [78] have been computed with sufficient resolution ($(L, N, M) = (10, 10 \cdot n_0, 50)$) imposing for each the axial wave-number k_0 that bifurcated at a minimal Re. All these solutions possess a shift & reflect symmetry ($S\&R$) with respect to a longitudinal plane:

$$S\&R: \quad (u_r, u_\theta, u_z)(r, \theta, z) \rightarrow (u_r, -u_\theta, u_z)(r, 2\,\theta_{SR} - \theta, z + \pi/\mathrm{k}_0), \tag{5.8}$$

where θ_{SR} is the azimuthal inclination of the reflection plane, that adds to the imposed discrete rotational symmetry (R_n):

$$R_n: \quad (u_r, u_\theta, u_z)\,(r, \theta, z) \rightarrow (u_r, u_\theta, u_z)(r, \theta + 2\pi/n, z). \tag{5.9}$$

The solutions have been continued in Re to unfold the $C2$, $C3$, $C4$ and $C5$ families of rotationally symmetric travelling waves. Figure 5.3 shows the Re-continuation curves of the computed families of travelling waves. It can be seen from Fig. 5.3a that all found travelling waves travel downstream faster than the flow mean axial velocity, and that the lower the azimuthal wave number, the higher the phase speed. The $C3$ family is the first one to bifurcate at $Re \simeq 1250$. Depicted in Fig. 5.3b are the friction factors (λ) associated with the given travelling waves. The nondimensional friction factor λ is the ratio between the driving pressure gradient and the flow kinetic energy [60], computed as

$$\lambda = \frac{-\Pi_0 D}{\frac{1}{2}\rho \bar{U}^2} = 64 \frac{Re}{{Re_a}^2}. \tag{5.10}$$

All the travelling waves found originate at local saddle-node bifurcations. Interestingly enough, the lower branch travelling waves exhibit friction factors that scale with Re in the

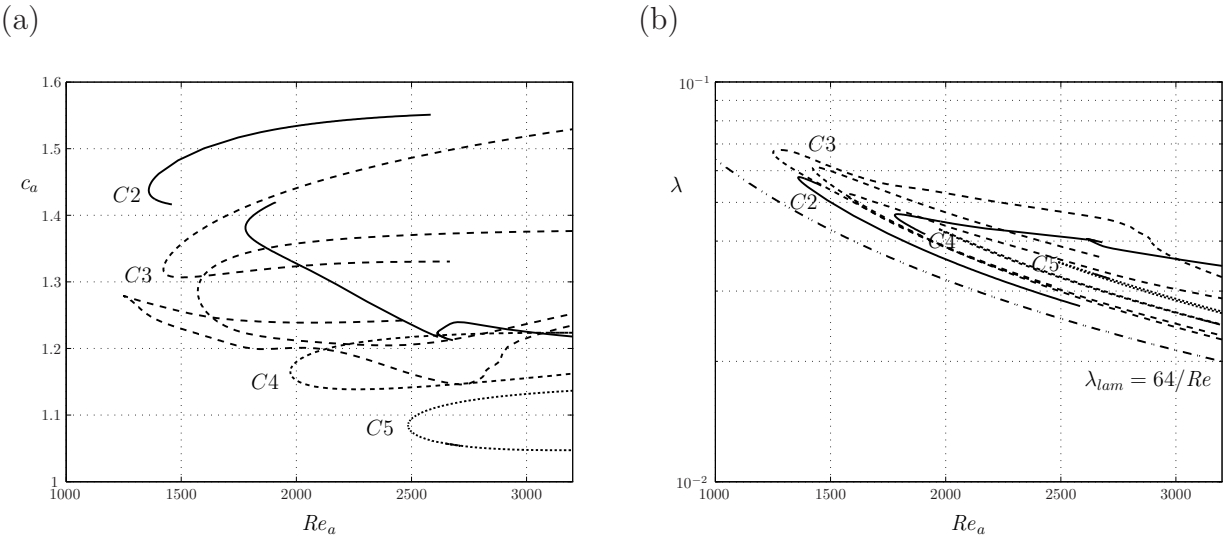

Figure 5.3: Re-continuation curves of the $C2$ (bold), $C3$ (long-dashed), $C4$ (short-dashed) and $C5$ (dotted) familes of travelling waves at their optimal axial wavenumbers (k_0 that bifurcated at the lowest Re_a). a) Phase speed c. b) Friction factor λ; the dash-dotted line represents the basic flow frictrion factor $\lambda_{lam} = 64/Re$

same way the laminar basic flow friction factor does, as can be ascertained in Fig. 5.3b where the basic flow friction factor is shown as a dash-dotted curve. At the same time, the upper branch travelling waves possess friction factors which are compatible with turbulent flow values.

In table 5.1 we summarise the main properties of the travelling waves found.

	$C2$	$C3$	$C4$	$C5$
k opt	1.55	2.44	3.23	4.11
Re_a bif.	1358.9	1250.8	1973.9	2485.2
Re	1664.2	1628.9	2604.1	3426.6
c_a bif.	1.44	1.28	1.17	1.08
c	0.59	0.49	0.44	0.39

Table 5.1: Some properties of the travelling wave families computed. Tabulated are the optimal axial wavenumber k, the actual Reynolds number Re_a at bifurcation, the corresponding nominal Reynolds number Re, the actual phase speed c_a at the bifurcation point, and the nominal phase speed c.

The actual appearance of the travelling waves at their bifurcation points is shown in Fig. 5.4. The strong streaky structure of the travelling waves, along with the slight 3D

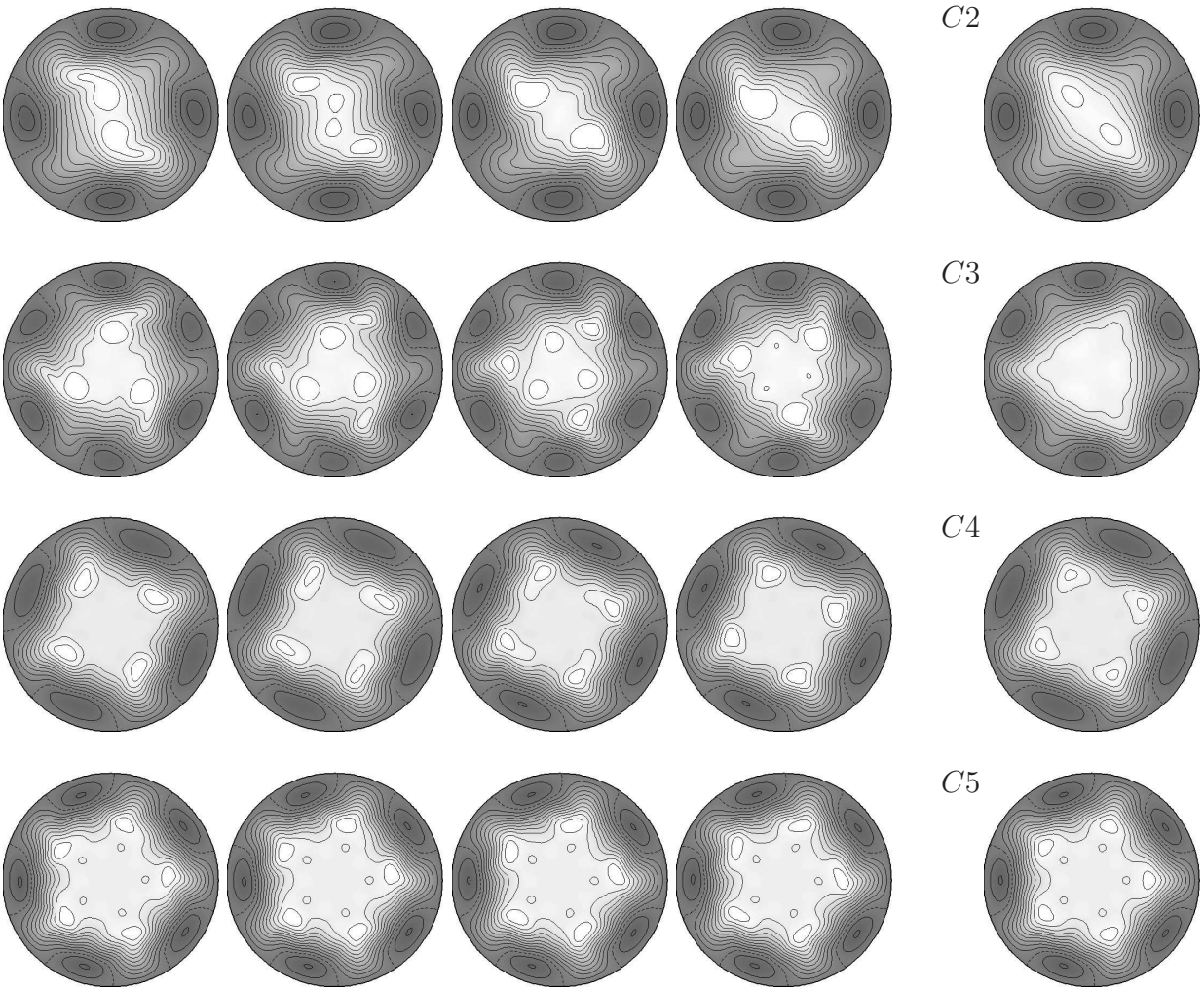

Figure 5.4: Aligned in rows, the $C2$, $C3$, $C4$ and $C5$ travelling waves at their bifurcation points. From left to right, four snapshots at $z = 0, \Lambda/8, \Lambda/4, 3\Lambda/8$ showing axial velocity contours of the perturbed field in the range $\pm 0.33 \cdot U_{\mathrm{CL}}$, and, fifth, axially averaged contours. Dark contours represent speeds higher than the underlying parabolic profile, light corresponds to regions with lower velocity.

wobbling structure is made clear in the snapshots across the pipe length. Only half of the pipe has been represented, benefiting from the shift & reflect symmetry. All travelling waves are characterised by low speed streaks in the central region of the pipe and high speed streaks in the outer region close to the walls.

Continuation in k and stability analysis, both within the azimuthal subspace to which they belong and in full space, have been performed for some of the solutions. They are not reported here as they do not add anything new to the picture presented in former work by other authors [19, 78].

For further details and a deeper analysis of the structure of these unstable travelling waves, please refer to the works where they were first reported [18, 19, 78]. Their relevance in developed turbulence has been investigated both experimentally [26] and numerically [31].

An attempt has been made to compute double-layered travelling waves, based on volume forcings imposing two radial layers of rolls. The forcings were designed to linearly enforce double-layered solutions of the Poisson equation in a circular domain. Whereas both forced travelling waves and forced relative periodic orbits were found, no success was achieved when removing the forcing and the solution always ended up falling back to the laminar flow.

5.4 Relative periodic orbits

The next simplest solution admitted by pipe flow is the relative periodic orbit. It can be seen as a pulsating or time-modulated travelling wave. The easiest way to track this type of solutions, which we have not implemented in the present work, would be to look for a static point in a Poincaré section of the equations written in a reference frame travelling downstream at the bulk speed of the travelling wave *c*arrying the solution. Recent work has been able to identify relative periodic orbits emanating in a Hopf bifurcation from a travelling wave [priv. comm. with Y. Duguet]. The solution found is, however, highly unstable, and seems to play but a marginal role, in the best of cases, in pipe flow transition.

5.5 Conclusions

Families of unstable travelling waves with $C2$, $C3$, $C4$ and $C5$- discrete azimuthal symmetry have been computed by means of a Newton solver. The initial guesses have been designed based on the self-sustained process applied to imposed azimuthal topological restrictions on the number of streamwise rolls involved. The painstaking process includes the design of a forcing of the right topology followed by a sweep in k, Re and forcing factor f aimed at finding forced stable travelling waves that bifurcate in the presence of the forcing. Removal of the forcing via continuation has led, in some cases, to the travelling waves already reported in the literature. Further continuation in k and Re has unfolded the full families of azimuthally symmetric travelling waves.

Their friction factors suggest that while the upper branch solutions (those closer in energy and friction factor to turbulent flow) may play a role in the turbulent dynamics, as has been proven in recent experimental work [27], the lower branch solutions could be relevant to turbulent transition. Nonetheless, recent work seems to indicate that other travelling waves with no azimuthal symmetry may outweigh these solutions in importance when it comes to transition understanding.

It is interesting to observe how all these z-periodic solutions are short in comparison with the length scale of the turbulent structures that appear in long pipes. The relationship between the solutions and these long structures (puffs and slugs) is still not clear, although experiments have reavealed that they seem to appear in certain locations of the turbulent structures.

Extension to double-layered vortical topologies has been attempted to no avail. Analysis with different number of pairs of rolls in the two layers is pending.

CHAPTER 6

EDGE TRAJECTORIES & UNDERLYING TRAVELLING WAVES

Transition to turbulence must be governed by states located in phase space between the basic flow and the turbulent chaotic attractor. This region is what we call the critical threshold. To try and identify these states we need to start by thoroughly examining trajectories wandering about criticality, namely trajectories that never decay to the basic laminar state nor experience transition to turbulence. It is well known from experience that such trajectories are unstable, since no initial condition has been found, numerically or experimentally, that triggers dynamics that live for an arbitrarily long period without ending up decaying or transitioning. There exist however a number of numerical techniques to compute trajectories living within a bounded region of phase space for as long as desired. One of such techniques, aimed at finding trajectories on chaotic saddles is the *PIM (Propper interior Maximum) triple procedure* [48].

It is fairly common in dynamical systems to find values of the parameters for which two or more attractors coexist. This is clearly the case of fluid mechanics and, in particular, of pipe flow, for which the basic flow coexists as a local stable solution with the turbulent attractor for Re beyond a certain critical value. In such cases, the basin boundary is nonempty, and the aforementioned technique can be easily adapted to find trajectories on the boundary between basins of attraction [49]. The method, though, is only applicable to chaotic saddles with a unique unstable dimension, which is very restrictive in high dimensional systems, where the number of unstable dimensions tends to be higher. An alternative general method called *Stagger-and-Step* exists, that can deal with chaotic saddles with several unstable directions [69].

In cases with two attractors that are easily identifiable, further simplification of these techniques leads to arbitrarily long computations on the boundary between basins of attraction. We have developed a very simple technique, based on those used in literature to compute such trajectories in a simplified model of a parallel shear flow [68] as well as in pipe flow [66].

This chapter is structured as follows. Section §6.1 is devoted to a thorough description of the method used to compute trajectories wandering about criticality simply using a time-stepping code. The way in which the several trajectories investigated in this work is set up, is explained in section §6.2. Section §6.3 presents the results corresponding to streak-breakdown-based critical trajectories on a short pipe, and the underlying coherent states are analysed in section §6.4. A long pipe critical trajectory is then presented in

section §6.5. Finally, the main conclusions are gathered in section §6.6.

6.1 A method to compute critical trajectories

We start a critical trajectory computation with an adequate choice of an initial condition that, when sufficiently scaled up in energy, is capable of triggering transition. The subcritical nature of pipe flow transition ensures that scaling down this initial condition we have access to a topologically identical initial condition that, after a more or less long laminar transient, ends up decaying back to the laminar flow. We can then hypothesise that, inbetween, there must exist an initial condition that will wander about criticallity, neither triggering transition nor decaying, for an infinite lapse of time. This is precisely what we want to compute and have therefore designed a *bisect-and-shoot* method to track these trajectories for arbitrarily long times. The method consists in parallely running from the same initial condition (a_o), properly scaled up and down such that one of the computations eventually leads to turbulence (turbulent run, $a^T(t)$, starting from $a_o^T = k_T\ a_o$) and the other ends up decaying to the basic flow (laminar run, $a^L(t)$, starting from $a_o^L = k_L\ a_o$). Whenever the distance between the two trajectories grows beyond a given tolerance ($|a^T(t_b) - a^L(t_b)| \geq \epsilon$) at time t_b, a bisection between the two trajectories is performed and the bisecting case run ($a^b(t)$ for $t \geq t_b$, starting from $a_o^b = (a^T(t_b) + a^L(t_b))/2$), for long enough as to discriminate whether it triggers transition or decays. The parallel computation of a laminar and a turbulent run bounding the critical trajectory is then resumed at time t_b, replacing the previous laminar (turbulent) case with the bisecting case if it happened to decay (transition). This method, composed of a sequence of shootings and bisections, leads to a trajectory wandering about criticality, never decaying nor transitioning to turbulent flow.

The criteria to decide whether a computational run must be considered as laminar or turbulent have to be chosen carefully. They must clearly detect when *irreversible* transition occurs (in a transient sense, since some experimental studies seem to point at a transient nature of turbulence, retaining always some probability that the flow may relaminarise [28]), or secular decay towards the laminar flow takes place, but at the same time must be wide enough to allow for considerable energy fluctuation within the critical boundary. We alternatively use perturbation energy, E_{tot}, or enforced axial pressure gradient, $(\nabla p)_z$, to establish criteria, and fix their cut-off values depending on experience gained from the prelimiary shooting computations run to initially bound the critical trajectory.

The method is very simple and overlooks the existence of folds in the critical surface or even its possible fractality in certain regions of the parameter space. In this case, simple

bisection leads to jumps that would be avoided by shooting many intermediate cases and sticking to, for example, the bounding cases with smallest amplitude. However, despite the jumps, the chaotic saddle living within the critical boundary is regularly visited and its dynamics evidenced.

6.2 Critical trajectories setup

All critical trajectories computed in the present work were performed in constant massflux pipes. Time integrations were thus performed with the time evolution code described in chapter 2, but adapted with an extra pressure gradient term that was adapted every time step in order to preserve the prescribed massflux. In this respect, every reference to the Reynolds number in this chapter must be understood as meaning the actual Reynolds number (Re_a).

Taking different types of initial condition, all capable of triggering transition when scaled up above a certain critical value of their amplitude, we have computed trajectories on the critical threshold. We chose three different transition scenarios to check for unicity of the saddle embedded in the critical threshold. Thus, *streak breakdown* based on 1, 2 and 3 pairs of vortices was first established as the transition scenario on a short pipe of $\Lambda = 10$, the different azimuthal symmetries introduced to select, if they exist, critical trajectories with different features. The streak breakdown initial conditions were the same investigated in chapter 3:

$$\mathbf{u}_0 = \mathrm{C}\,(\overbrace{\mathrm{e}^{\mathrm{i}n\theta}\mathbf{v}_n(r)}^{\mathbf{u}_0^{\mathrm{2D}}} + \overbrace{\mathbf{u}_{\mathrm{rand}}(r,\theta,z)}^{\mathbf{u}_0^{\mathrm{3D}}} + \mathrm{c.c.}), \tag{6.1}$$

where c.c. stands for complex conjugated terms, C is a factor to scale the initial condition to the desired overall energy and the radial structure takes the simplest polynomial form compatible with solenoidality and non-slip boundary conditions:

$$\mathbf{v}_n(r) = -\mathrm{i}\; n\; r^{\sigma-1}(1-r^2)^2\;\hat{\mathbf{r}} + \mathrm{D}[r^{\sigma}(1-r^2)^2]\;\hat{\boldsymbol{\theta}}, \tag{6.2}$$

where $\sigma = 1$ (2) for n odd (even), D denotes the radial derivative, and with $\mathbf{u}_{\mathrm{rand}}$ a random perturbation velocity field of the desired amplitude, containing much lower energy than the streamwise component. $n = 1$, 2, 3 for 1, 2 and 3 pairs of rolls, respectively.

All cases were run at $Re = 2875$ for the sake of comparison with the first reported critical trajectories, dubbed *edge of chaos* [66]. A moderate resolution of $(L, N, M) = (16, 16, 24)$ was considered as sufficient to cast light on the salient features of these trajectories, without

being too demanding in terms of computational cost. $\Delta t = 5 \cdot 10^{-3}$ was taken as the time step.

Finally, the task of producing critical trajectories on a long pipe of $\Lambda = 100$ was undertaken. The transition scenario chosen was the generation of *puffs* at $Re = 2000$, with the main goal of producing localised *puff*-like states on the very edge of criticality. In this case, we contented ourselves of studying the bulk dynamics of such a trajectory within an under-resolved pipe with $(L, N, M) = (64, 8, 16)$ and $\Delta t = 10^{-2}$. The initial condition used to produce local transition to puffs was taken as a single pair of the simplest streamwise rolls, axially compressed by means of a gaussian-type dependency:

$$\mathbf{u}_0 = \mathrm{C}\ (\mathrm{e}^{\mathrm{i}\,\theta}\mathbf{v}_1(r) + \mathbf{u}_{\mathrm{rand}}(r,\theta,z) + \mathrm{c.c.})\ \mathrm{e}^{-100\ \sin^2(\frac{\mathrm{k}}{2}\,z)}. \tag{6.3}$$

6.3 Short pipe critical trajectories

The three streak breakdown initial conditions lead, after different transient non-normal growths that naturally preserved the azimuthal symmetry, to very similar chaotic long-term behaviours, indicating that all three trajectories were eventually captured by the same chaotic saddle within the critical boundary. This can be readily derived from the outstandingly similar behaviour of $(\nabla p)_z$, plotted in Fig. 6.1. Each of the initial perturbations exhibits a different transient growth, characterised by different pressure gradient maxima (not shown in Fig. 6.1) at time around 15-30, during which the azimuthal symmetry is preserved. After the surge, the pressure gradient drops back and starts fluctuating randomly within 5-35% above the basic flow value. By the time the chaotic behaviour begins, the original spatial structure has been dismantled, the critical trajectories keep no remembrance of the initial condition topology and their evolution becomes indistinguishable from one another. It can be advanced from the behaviour of $(\nabla p)_z$, that some sort of low frictional state or states are regularly visited by the critical trajectories, evidenced by significant long drops down to within 5% of the basic flow pressure gradient.

These remarks are clearly backed by the evolution of the 1D (axisymmetric, streamwise-independent component), 2D (non-axisymmetric, streamwise-independent components) and 3D (non-axisymmetric, streamwise-dependent components) energies, defined in chapter 3. They are plotted along with the total perturbation energy in Figs. 6.2a-c. The energy levels, and their fluctuation amplitude and frequency, are very similar in all cases. Also the approaches to some sort of slowly evolving states is evidenced by consistent long drops of the energy levels, even though the approaches are not sustained and are eventually followed

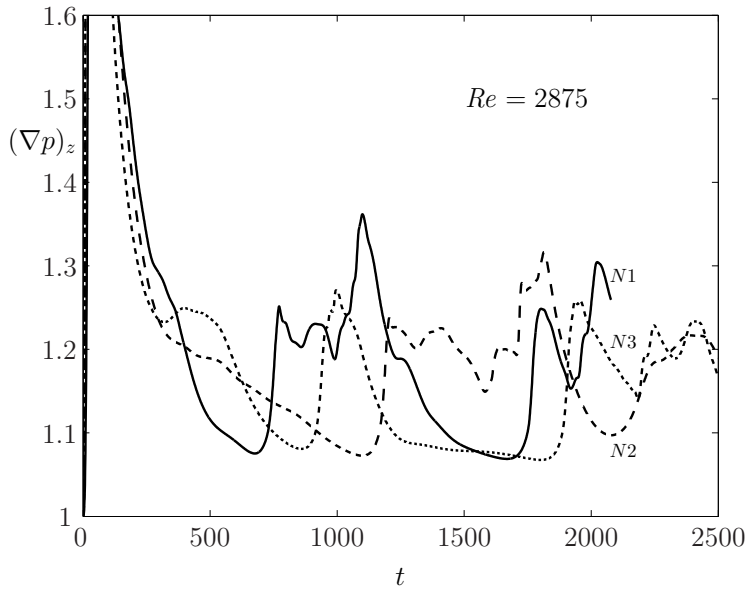

Figure 6.1: Driving axial pressure gradient $(\nabla p)_z$ evolution of the $N1$, $N2$ and $N3$ critical trajectories.

by a flow breakdown, exhibiting a more chaotic behaviour.

6.4 Short pipe underlying coherent structures

The short pipe critical trajectories approach what is known as an *edge state* [68, 66], which in the case of pipe flow turns out to be a chaotic saddle, the unstable direction pointing outside of the critical boundary, and therefore artificially stabilised by the bisection method used. Restricting the computation to certain invariant subspaces of given azimuthal periodicity, the edge state happens to coincide with previously found travelling wave solutions [Priv. Comm. with B. Eckhardt and T. Schneider]. This is the case in the $C2$ subspace [17], due to the fact that the travelling wave has only one unstable direction within the $C2$ subspace that points in a direction transverse to the critical boundary and, therefore, the travelling wave becomes an attractor within this $C2$ critical boundary. Other travelling waves, with more unstable directions, some laying on the critical boundary, and possibly relative periodic orbits or more complex solutions, together with their heteroclinic and homoclinic connexions, could then be responsible for the chaotic saddle identified in full space.

All these solutions underlying the chaotic saddle are unstable, and cannot, by any

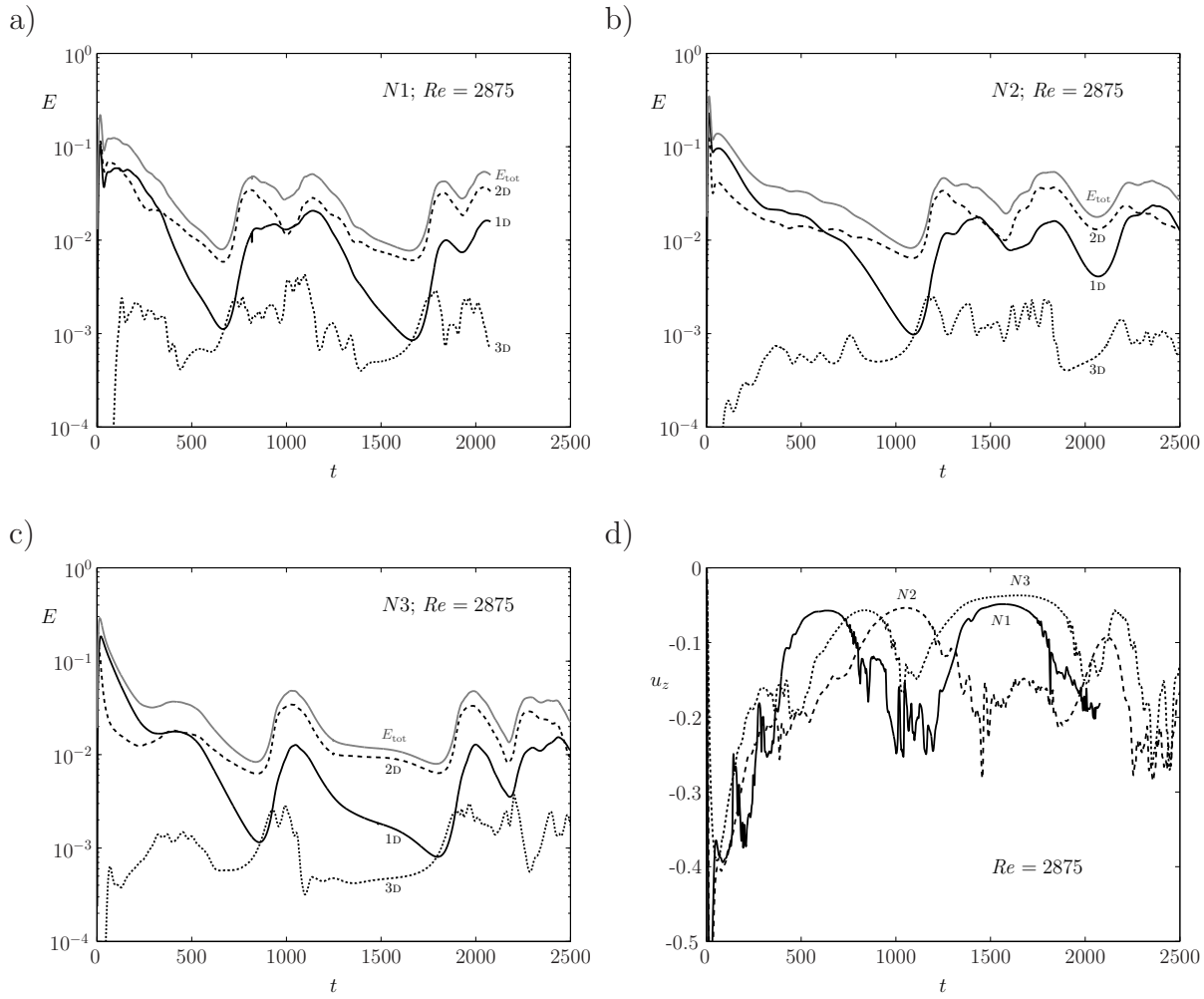

Figure 6.2: 1D, 2D, 3D, and total perturbation energy evolution corresponding to a) $N1$, b) $N2$ and c) $N3$ critical trajectories. d) Axial velocity u_z at a point on the pipe axis fixed in the comoving reference frame.

means, be computed through direct time evolution. We have, however, access to unstable travelling wave type solutions via an adapted Newton method, and can therefore try and identify these sort of solutions within the chaotic saddle.

Following a critical trajectory, it is possible to define a function in order to assess how far the trajectory is at each time instant from being an exact travelling wave solution. It suffices to evaluate the residual going into the adapted Newton method presented in chapter 5:

$$r_{tw}(t) = \| \mathrm{F}(a(t), c(t)) \| = \| \mathbb{I}\, a(t) + \mathbb{B}^{-1}(i\mathrm{k}lc(t)\, \mathbb{A}\, a(t) - b(a(t), a(t))) \|, \qquad (6.4)$$

where the travelling wave phase speed $c(t)$ is estimated from the instantaneous speed with

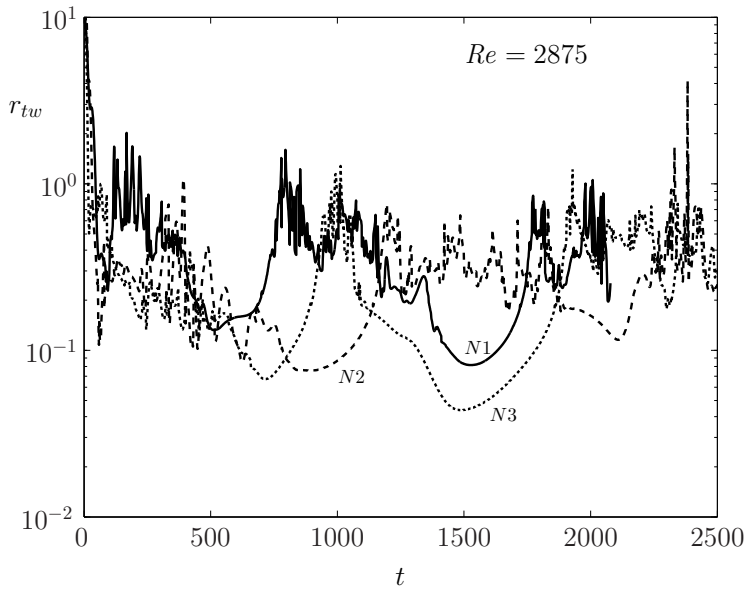

Figure 6.3: Travelling wave residual r_{tw} as a function of time along the streak breakdown critical trajectories.

which the structure is advected downstream, namely the speed of the comoving reference frame in which the perturbation flow would seem to be spatially stopped, although not necessarily stationary.

The residual just defined becomes, by construction, a clear indicator of whether the trajectory is approaching something resembling a travelling wave solution. The instants with a minimum of this residual are then selected as good candidates for a travelling wave hunt, and directly fed to the adapted Newton method, with its convergence region enhanced via *damping* techniques.

Figure 6.3 depicts the time evolution of the residual along the three critical trajectories. All critical trajectories are characterised by a fairly large rapidly fluctuating residual that experiences recurrent drops, that can be identified as possible approaches to something resembling a travelling wave solution.

These residual drops are good candidates to be plugged as initial conditions into the Newton solver. They naturally correspond to a slow evolution of the energy signals shown in Figs. 6.2a-c. Close inspection of the axial velocity at a point on the pipe axis fixed in the comoving reference frame, represented in Fig. 6.2d, clearly shows evidence of some sort of underlying coherent structure, the actual nature of which remaining still unknown. The residual minima coincide with the slow saturation of the axial velocity at the particular

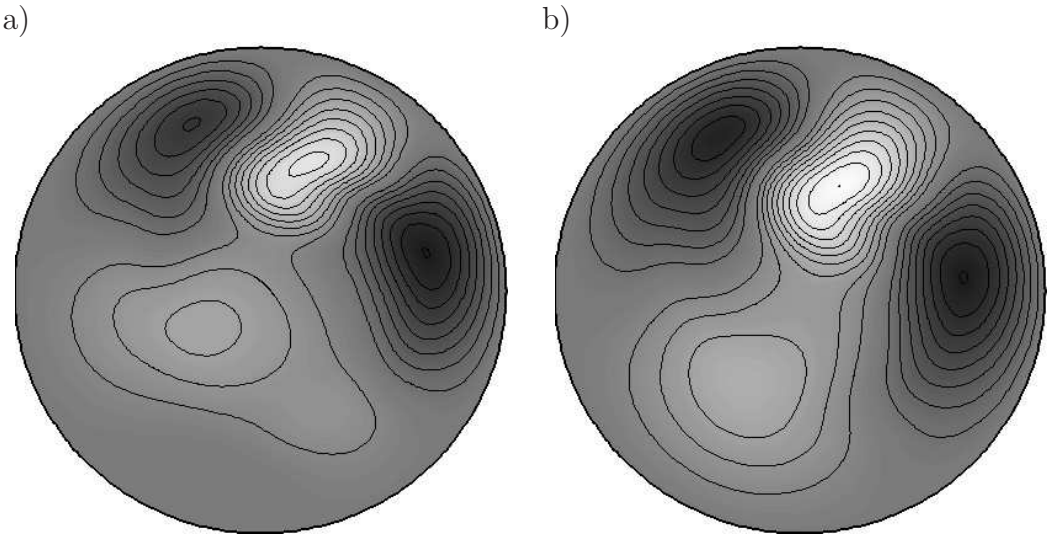

Figure 6.4: Axial velocity contours ($\pm 0.44\bar{U}$) of the perturbation field at a given cross-section for a) the $N1$ critical trajectory at time $t = 1530$, and b) the converged travelling wave. White corresponds to negative and black to positive values.

point chosen. Constant velocity in the comoving reference frame for all points would mean a travelling wave solution has been found. The saturation, although only temporary, could be a trace of an underlying travelling wave solution.

Feeding these instantaneous velocity fields, corresponding to residual minima, into the Newton solver, consistently produced convergency onto the same travelling wave solution, save for its azimuthal orientation. As an example, axial velocity contours on a cross-section at a given axial coordinate for both the $N1$ critical trajectory at $t = 1530$ and the converged travelling wave are shown in Fig. 6.4. The dynamics are clearly dominated by a wobbling excentric low speed streak, sandwiched between a pair of high speed streaks.

This travelling wave, computed at $Re = 2875$ and characterised by a phase speed $c_a = 1.555\bar{U}$, is the one recently found by volume forcing homotopy in Pringle & Kerswell [55]. Re continuation of the converged solution leads to a full branch of solutions, originating, at a lower Re, from a pitchfork bifurcation of a symmetric travelling wave. Apart from the $S\&R$ symmetry, this latter travelling wave posseses a simple reflection symmetry (RS) with respect to a diameter:

$$RS: \quad (u_r, u_\theta, u_z)(r, \theta, z) \rightarrow (u_r, -u_\theta, u_z)(r, 2\,\theta_{RS} - \theta, z), \tag{6.5}$$

where θ_{RS} is the azimuthal inclination of the reflection plane. When both symmetries are combined, as is the case, the corresponding reflection planes necessarily cut each oder at

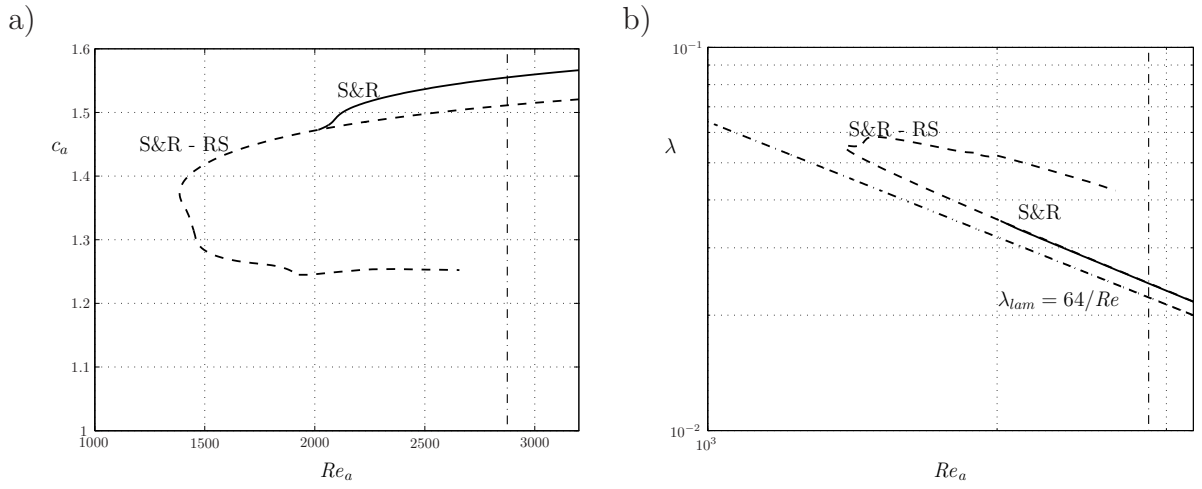

Figure 6.5: Bifurcation diagrams of the travelling wave underlying the critical trajectory ($\Lambda = 10$). The bold line corresponds to the Shift & Reflect (S&R) travelling wave, while the Reflection-Symmetric (S&R - RS) travelling wave is represented with the dashed line. $Re = 2875$ to which the critical trajectories correspond, is indicated with a dash-dotted line. a) Actual phase speed c_a as a function of Re_a. b) Friction factor λ.

a right angle ($\theta_{RS} - \theta_{RS} = \pm\pi/2$). The resulting symmetry group is a shift & rotate symmetry ($S\&R - RS$):

$$S\&R - RS: \quad (u_r, u_\theta, u_z)(r, \theta, z) \rightarrow (u_r, u_\theta, u_z)(r, \theta + \pi, z + \pi/\mathrm{k}_0). \tag{6.6}$$

The bifurcation diagram is shown in Fig. 6.5.

The lower-branch symmetric travelling wave, shown in Fig. 6.6, undergoes a symmetry breaking pitchfork bifurcation at $Re \simeq 2010$, generating two branches of mutually symmetric travelling waves (superimposed in Fig. 6.5) corresponding to the one directly converged from the edge trajectory. This symmetric travelling wave can be continued down in Re to a lowest value of $Re \approx 1386$, where it emerges at a saddle-node bifurcation of orbits. k continuation to unfold the full family of travelling waves reveals that for a different axial wavenumber the symmetric travelling wave can be continued to much lower Re (the lowest of all known solutions) [55], which we do not include here, since these solutions have no representation in the studied critical trajectory. This travelling wave holds a striking topological resemblance with some of the $C2$ rotationally symmetric travelling waves, although no connection has been found so far.

The Newton solver as described is restricted to the search of travelling waves with

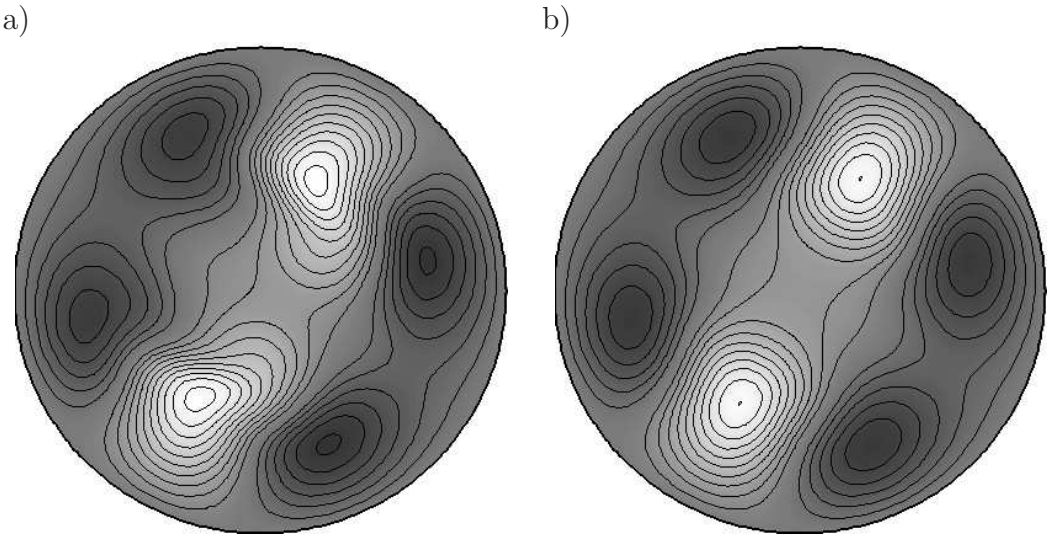

Figure 6.6: a) A snapshot and b) z-averaged axial velocity contours ($\pm 0.386\bar{U}$) of the symmetric travelling wave perturbation field at $Re = 2875$. Negative velocities are coded in white and positive in black.

no rotation. The chaotic saddle embedded in the critical trajectories, however, may be constituted by a number of simple solutions among which the travelling wave found is just one. There might also be relative periodic orbits or even rotating travelling waves, as the one found in Duguet *et al.* [17]. To allow for the convergence onto rotating travelling waves, the Newton solver has been adapted to take into account the possibility of a rotational speed. This has been done by considering solutions, based on expression 5.3, of the form:

$$a_{lnm}^{(s)}(t) = a_{tw}\ \mathrm{e}^{-\mathrm{i}(\mathrm{k}lc+nc_t)t}, \tag{6.7}$$

where c_t is the rotating rate given in units of U_{CL}/a rad, that is in revolutions per time unit. Modifying the functional given in 5.5 accordingly, and particularising to the constant massflux scenario, we end up looking for zeroes of

$$\mathrm{F}(a,c) = a + \mathbb{B}^{-1}(\mathrm{i}(\mathrm{k}lc + nc_t)\mathbb{A}\ a - b(a,a) + \mathrm{C}f_{cm}). \tag{6.8}$$

Feeding the same initial guesses from the critical trajectories to the Newton solver produced, in most of the cases, the same shift & reflect travelling wave already described and shown in Fig. 6.4b. In at least one case ($N2$ critical trajectory, $t = 890$), though, convergence was obtained onto a rotating travelling wave that bore very close resemblance to the non-rotating one in all respects (topology, energy contents and axial phase speed $c_a = 1.517\bar{U}$), but for the shift & reflect symmetry breaking, with a very slight rotation rate

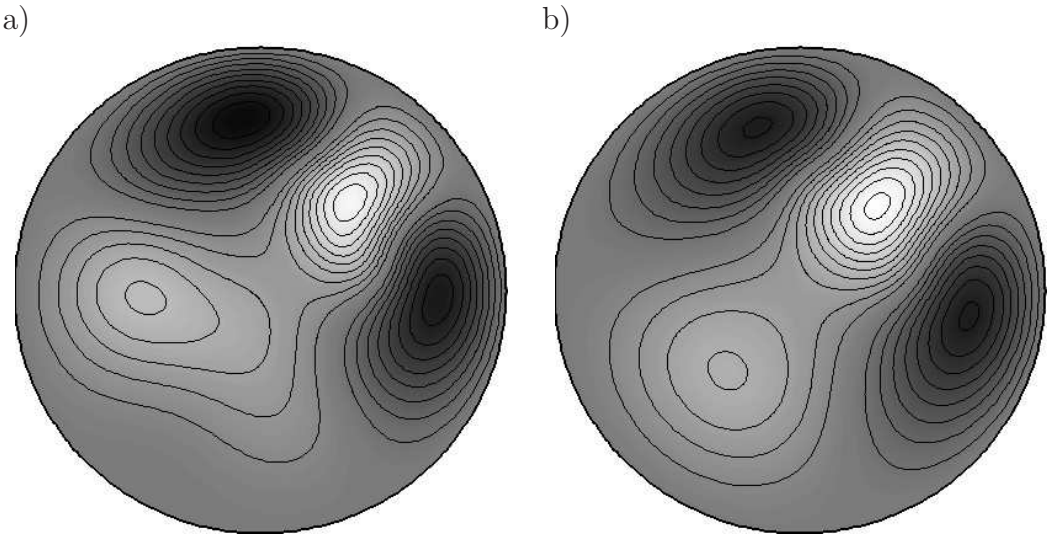

Figure 6.7: z-averaged axial velocity contours ($\pm 0.42\bar{U}$) for a) the non-rotating, and b) the rotating travelling waves.

of $c_t = -4.67 \cdot 10^{-4}\bar{U}/a$ rad. z-averaged axial velocity contours of the non-rotating and the rotating travelling waves are shown in Figs. 6.7a and 6.7b, respectively. The non-rotating travelling wave appears symmetric upon z-averaging due to its shift & reflect symmetry, while the rotating travelling wave is clearly non-symmetric. Their topological resemblance becomes evident when inspecting the velocity fields.

6.5 Long pipe critical trajectories

The localised rolls initial condition in the long pipe produced a localised *puff*-like critical trajectory, with very fast and short wavelength dynamics in the vicinity of the trailing edge and very slowly evolving long wavelength dynamics in the extended leading edge. The pressure gradient time trace, plotted in Fig. 6.8, is much closer to that of the laminar parabolic profile value (within 5%), due to the fact that the perturbation is localised in space and that the basic flow remains predominantly unaltered in a big portion pf the pipe length. Its fluctuation, however, is much wider, in relative terms, and chaotic, when compared with the short pipe critical trajectories. Furthermore, no clear traces of regular visits to any low frictional state can be spotted, except for some sharp drops of very short duration every now and then.

This very chaotic behaviour also affects the energy time signals, shown in Fig. 6.9.

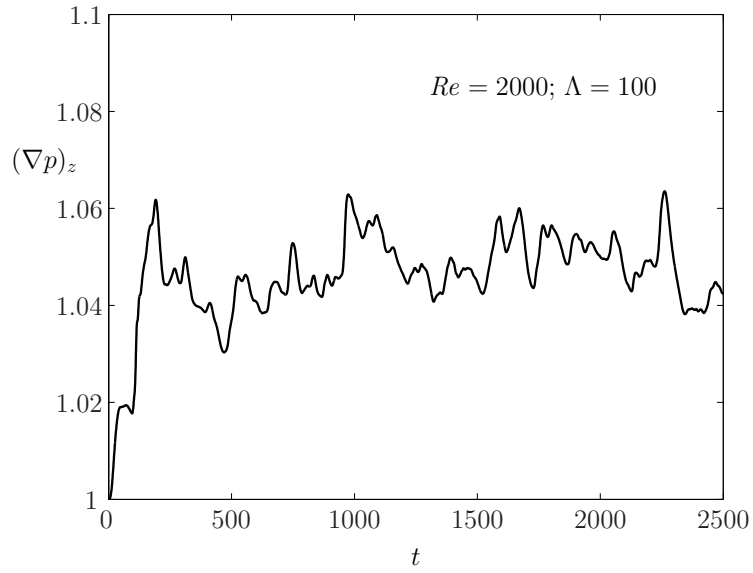

Figure 6.8: Driving axial pressure gradient $(\nabla p)_z$ evolution of the *puff*-like critical trajectory.

From the energy plot it is clear that most of the energy is carried by 3D modes, the flow being strongly 3-dimensional throughout the trajectory. Visits to slowly evolving states are much less clear than for the short pipe streak-breakdown critical trajectories. The time signal is consistently more chaotic, as already pointed out, but at the same time extremly homogeneous in the sense that nothing resembling a coherent solution is clearly approached at any time.

As already stated, and in spite of the moderate resolution, especially in the axial coordinate, the main features of the puff structure are clearly mimicked by the critical trajectory, except for the overall energy level, which is lower. This comes as no surprise since the critical trajectory dwells in the boundary between the basins of attraction of the puff itself and the basic flow. The aforementioned features are a more or less sharp and well defined trailing edge and an extended leading edge, the overall structure occupying approximately $25D$, that is 50% of the pipe length. This is illustrated in Fig. 6.10, where θ-averaged contours of u_z are plotted with the contour lines taking $\pm 5\%\ \bar{U}$ as the cutoff value.

Despite the fact that the time traces of all plotted quantities, including velocities in several points of the domain, showed no clear evidence of approaching simple coherent structures, the residual time trace helped identify a number of relatively acceptable initial guesses for the Newton solver. The residual is plotted against time in Fig. 6.11. Although the residual evolution is strongly fluctuating, there are clear drops at some particular time

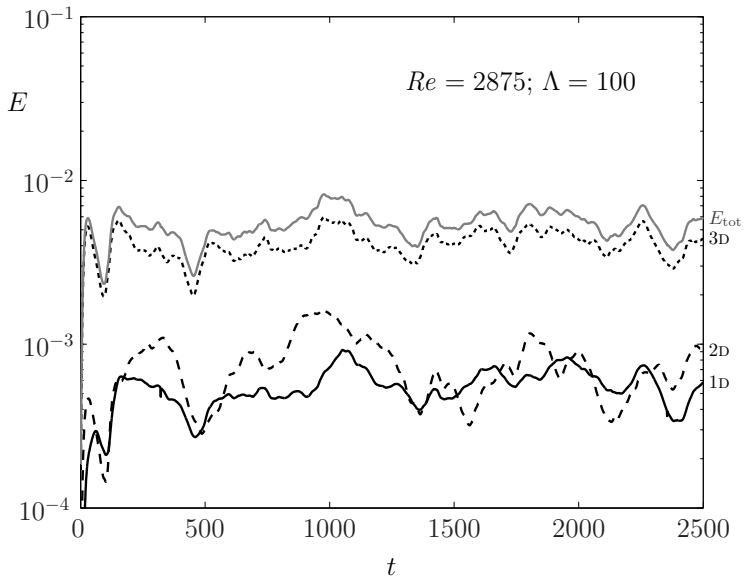

Figure 6.9: 1D, 2D, 3D, and total perturbation energy evolution corresponding to the *puff*-like critical trajectory.

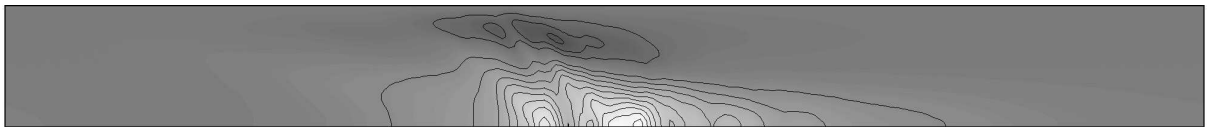

Figure 6.10: Long pipe critical trajectory θ-averaged u_z contours at $t = 860$ ($\pm 0.37\bar{U}$, lowest contour lines at $\pm 0.05\bar{U}$). Negative values are shown in white, while positive are represented in black.

instants along the trajectory. Some of the drops immediately bounce back to high residuals, while others seem to dwell at low values for some time before surging back.

All the flow fields corresponding to residual minima have been used as initial guesses for the Newton solver, but to no avail. The computations indefectively converged onto the basic flow as a particular case of travelling wave. In some of the cases corresponding to relatively long lasting low residuals, however, the Newton method stagnated at a fairly low residual, although not low enough as to consider the solution a fully converged travelling wave. In these cases, the Newton method strikingly tended to symmetrise the flow field, conserving the streamwise length of the structure virtually unaltered. Figure 6.12, depicts θ-averaged axial velocity contours of the pseudo-converged state. It preserves the main features of the critical trajectory from which it originates, such as its characteristic length. Time-stepping shows that this state evolves very slowly in the beginning, although not for

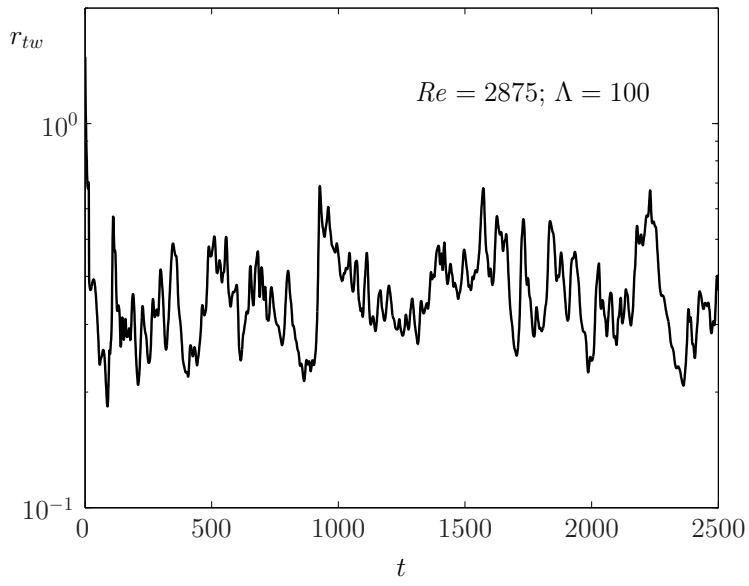

Figure 6.11: Travelling wave residual r_{tw} as a function of time along the *puff*-like critical trajectory.

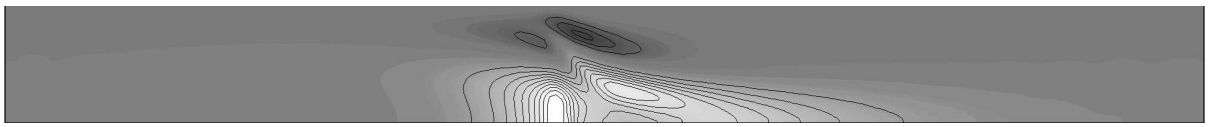

Figure 6.12: Long pipe pseudo-converged state. Depicted are θ-averaged u_z contours ($\pm 0.15\bar{U}$, lowest contour lines at $\pm 0.05\bar{U}$). Negative values are shown in white, while positive are represented in black.

very long time, and then soon breaks up. These minima of the residual could be nothing but local minima, but there exists the possibility that they hide some sort of simple structure involving other frequencies apart from the one related to the travelling wave downstream advection. A relative periodic orbit or something more complex could be veiled behind these local minima. Nevertheless, it cannot be discarded that truncation may also be playing a role if the underlying structures require higher resolution to be properly represented.

6.6 Conclusions

A very simple method to compute trajectories that never trigger transition nor decay to the laminar basic flow has been devised. Examples of these critical trajectories have

been computed on both short ($\Lambda = 10$) and long pipes ($\Lambda = 100$) to try and clarify the phenomenon of transition.

Different initial conditions produced equivalent long time behaviours in the case of short pipe. The trajectories were in every case captured by the same chaotic saddle lying within the critical threshold. In their erratic evolution, the trajectories recurrently approached low frictional states, corresponding to very low residuals from the point of view of their resemblance to a travelling wave. Use of an adapted Newton solver helped identify at least two travelling wave states, one with azimuthal rotation, underlying the chaotic saddle. *Re*-continuation of the non-rotating state, showed that it emerged at a Pitchfork bifurcation of a symmetric state that could be traced back to very low *Re*, where it originates at a saddle-node bifurcation. The symmetric travelling wave, although existent at $Re = 2875$, for which the critical trajectories were computed, does not seem to be directly approached at any time. None of the lower branch travelling waves discovered so far, which are known to live on the critical threshold, was approached at any time, either. Thus, these new travelling waves seem to bear all responsibility for transition as yet. At least in the short pipe frame.

The same procedure on a long pipe, where turbulence is characterised by intermittency phenomena, produced critical trajectories that were localised in space and of the characteristic length of a puff. The critical trajectory, however, exhibits a strongly chaotic behaviour and no clear visits to low frictional states can be identified. No underlying travelling waves have been found behind the residual minima, although their existence cannot be completely ruled out, as cannot be discarded the presence of more complex solutions such as pulsating travelling waves.

CHAPTER 7
CONCLUSIONS & FUTURE PERSPECTIVES

The very recent discovery of finite amplitude solutions other than the basic flow [19, 78] has brought renewed momentum to the long trailing problem of subcritical transition in pipe flow. For the first time in many decades, an answer seems within reach of the scientific community. Nonetheless, these states alone do not seem to explain transition nor developed turbulence in full.

Two different approaches have been undertaken in the present work in order to try and shed some light on this yet unsolved problem of subcritical turbulence in shear flows as a chief interest of the aeronautical community. The viscous flow driven by a pressure gradient through a cylindrical pipe (Hagen-Poiseuille flow) was chosen as the object of study and numerical simulation as the research method.

To this end, an efficient and robust Petrov-Galerkin spectral scheme, presented and tested in chapter 2, has been developed. It has been the essential tool upon which the whole of the work here presented lies. The scheme has proven very reliable in reproducing the stability analysis of the basic flow, in its linear version, and very fast and robust for the computation of fully nonlinear time evolution.

A first approach consisted in an attempt to characterise the basin of attraction of the stable basic flow through the estimation of the asymptotic exponential scaling law governing the shrinking of the basin with increasing Reynolds number. The critical amplitude, as was already known, has been shown to depend on the perturbation shape. Different types of perturbations produced different scaling laws. In chapter 3, the focus was set on global preferently-streamwise-independent vortical perturbations consisting of different numbers of pairs of rolls with very small 3-d noise on top, that were capable of triggering transition via streak-breakdown. It has been shown that different numbers of pairs of rolls produce different dependencies of the critical amplitude threshold with Re. The scaling laws found are compatible with experimental studies that aimed precisely at estimating the asymptotic behaviour of the critical threshold [11], even though the perturbations studied are not reproducible in the lab. It cannot be claimed that streak breakdown is the most efficient way of inducing transition, and thus responsible for the critical threshold understood as the minimal amplitude of perturbations triggering transition, but it has been shown a very effective and global scenario, fairly independent of the pipe length considered as long as certain critical wavelengths are allowed to grow freely. It has also been shown that at the low Re-range turbulence is a transient phenomenon, and that relaminarisation is often

observed. It reamins an open debate whether turbulence becomes permanent beyond a certain *critical* Re number [79] or stays a transient phenomenon [28]. In this latter case, which seems to be supported by both experimental and numerical studies, an exponential increase of turbulence lifetime with Re would explain why relaminarisation is never observed experimentally even for moderate Re. This we cannot ascertain from the results of our work.

The same sort of study was then repeated for perturbations of the type most commonly used in experimental settings. Thus, in chapter 4, the attention was turned to local injected perturbations. An equivalence, in terms of the effects produced, has been proven between an injection and a volume forcing inducing the right acceleration field on the flow. A longer pipe had to be considered to allow for localised perturbations growth such as puffs and slugs. The overall features of these structures have been reliably reproduced. The scaling law obtained for this type of perturbations is in very good agreement with experimental results [27], giving credibility to the streak breakdown mechanism as a more effective way of inducing transition. The exponential decrease obtained for global vortical perturbations constitutes therefore the lowest bound found so far for the critical threshold and a best estimate of the shrinking of the basin of attraction of the basic parabolic flow as Re is increased.

Characterisation of the critical threshold is, however, not enough to comprehend the very nature of transition. Another approach that has very recently landed in pipe flow research is the direct exploration of phase space. No solutions other than the laminar parabolic profile had been found until the break of this century. The recent discovery of travelling wave solutions has allowed to apply classical dynamical systems theory to the pipe problem anew.

Benefiting from the solenoidal spectral Petrov-Galerkin description and its very simple algebraic representation, an adapted Newton solver to track travelling wave type solutions was implemented, and a volume forcing homotopy method devised to recompute these recently discovered states [19, 78]. These states, that have been shown in literature to play a role in developed turbulence, we have computed and continued in chapter 5. Several studies are currently ongoing to try and understand what their implications in transition might be, but their relevance remains bewildering, especially in the light of the recent discovery of a chaotic state lying in the very edge of criticality [66]. The lower branch travelling waves have been shown to rest on the critical threshold, but they are strong repellors within the critical manifold and only become attractors or weak repellors organising a chaotic critical state when computations are restricted to the azimuthal symmetry subspace to which they belong.

Critical trajectories have been investigated in chapter 6. The unicity of the chaotic saddle within the critical threshold for short pipe has been tested by basing the computations on three different initial conditions capable of bringing about transition through streak breakdown. All three initial conditions, consisting of 1, 2 and 3 pairs of rolls, lead to the same chaotic state, even though the azimuthal symmetry of the $N2$ and $N3$ perturbations tried to ease convergence onto states governed by the $C2$ and $C3$ travelling waves described in chapter 5. The state, which is chaotic, periodically visits some sort of low friction state. These transients were fed into the Newton solver, and a travelling wave with no azimuthal symmetry recently discovered through volume forcing homotopy [55], has been identified. Also another travelling wave with very slow rotational speed has been found within the critical trajectory. Because of their direct convergence from a critical trajectory, their relevance in transition is believed to be of the utmost importance. Nevertheless, they only exist in relatively short pipes and their connection with localised turbulent structures such as puffs or slugs is beyond what can be hitherto ascertained.

To understand transition in experimental pipes, much longer numerical pipes need to be studied as well, if only to find out what the relationship between short and long pipes transition is. This we have also attempted in chapter 6, where critical trajectory computations on a poorly resolved long pipe are presented. The critical state remains chaotic but localised. Its global structure is like that of the puff, but whith lower energy contents and much higher spatial coherence. No travelling wave solution has been found underlying this critical state, but the Newton solver stagnated at a fairly low residual, producing a very slowly evolving state with reflection symmetry that may have the basic ingredients of the chaotic saddle embedded in the critical threshold. It cannot be discarded that a number of travelling wave solutions and their heteroclinic conections conform the state, but it seems more probable that more complex solutions like relative periodic orbits or toruses may be involved.

Some of the questions that still need an answer concern the permanent or transient nature of turbulence and the actual underlying structure of puffs and slugs. Localised simple states, if they exist, should be the target of future investigation, as they could hold the key to understanding intermittency phenomena, which are typical of shear flows turbulence. How the already found periodic states fit in the nonperiodic frame of localised structures, as experimental studies seems to point out [26], is also a matter of wonder that needs thorough scrutiny.

All things considered, the main ingredients of transition and turbulence seem to be now on the table. Putting the puzzle together is what now lies ahead.

BIBLIOGRAPHY

[1] Barkley, D. & Tuckerman, L. S. 2005 Computational study of turbulent laminar patterns in Couette flow. *Phys. Rev. Lett.* **94**, 014502–.

[2] Batchelor, G. K. 1967 *An Introduction to Fluid Dynamics*. Cambridge: Cambridge University Press.

[3] Boberg, L. & Brosa, U. 1988 Onset of turbulence in a pipe. *Z. Naturforsch.* **43a**, 697–726.

[4] Boyd, J. P. 2001 *Chebyshev and Fourier Spectral Methods*. Dover.

[5] Brosa, U. 1989 Turbulence without strange attractor. *J. Stat. Phys.* **55**, 1303–1312.

[6] Brosa, U. & Grossmann, S. 1999 Minimum description of the onset of pipe turbulence. *EPJB* **9**, 343–354.

[7] Canuto, C., Hussaini, M. Y., Quarteroni, A. & Zang, T. A. 1988 *Spectral Methods in Fluid Dynamics*. Berlin: Springer-Verlag.

[8] Chapman, S. J. 2002 Subcritical transition in channel flows. *J. Fluid Mech.* **451**, 35–97.

[9] Cherhabili, A. & Ehrenstein, U. 1997 Finite-amplitude equilibrium states in plane Couette flow. *J. Fluid Mech.* **342**, 159.

[10] Cox, S. M. & Matthews, P. C. 2002 Exponential time differencing for stiff systems. *J. Comput. Phys.* **176**, 430–455.

[11] Darbyshire, A. & Mullin, T. 1995 Transition to turbulence in constant-mass-flux pipe flow. *J. Fluid Mech.* **289**, 83–114.

[12] Dauchot, O. & Daviaud, F. 1995 Finite amplitude perturbation and spots growth mechanism in plane Couette flow. *Phys. Fluids* **7**, 335–343.

[13] Draad, A. A., Kuiken, G. D. C. & Nieuwstadt, F. T. M. 1998 Laminar-turbulent transition in pipe flow for newtonian and non-newtonian fluids. *J. Fluid Mech.* **377**, 267–312.

[14] Drazin, P. G. 2002 *Introduction to Hydrodynamic Stability*. Cambridge: Cambridge Univ. Press.

[15] Drazin, P. G. & Reid, W. H. 1981 *Hydrodynamic Stability*. Cambridge: Cambridge Univ. Press.

[16] Drissi, A., Net, M. & Mercader, I. 1999 Subharmonic instabilities of tollmien-schlichting waves in two-dimensional poiseuille flow. *Phys. Rev. E* **60(2)**, 1781–1791.

[17] Duguet, Y., Willis, A. P. & Kerswell, R. R. 2008 Transition in pipe flow: the saddle structure on the boundary of turbulence. *under consideration for publication in J. Fluid Mech.* .

[18] Faisst, H. 2003 Turbulence transition in pipe flow. PhD thesis, Philipps-Universitt Marburg.

[19] Faisst, H. & Eckhardt, B. 2003 Travelling waves in pipe flow. *Phys. Rev. Lett.* **91(22)**, 224502.

[20] Faisst, H. & Eckhardt, B. 2004 Sensitive dependence on initial conditions in transition to turbulence in pipe flow. *J. Fluid Mech.* **504**, 343–352.

[21] Fornberg, B. 1996 *A Practical Guide for Pseudospectral Methods*. Cambridge: Cambridge University Press.

[22] Gavarini, M. I., Bottaro, A. & Nieuwstadt, F. T. M. 2004 The initial stage of transition in pipe flow: role of optimal base-flow distortions. *J. Fluid Mech.* **517**, 131–165.

[23] Hairer, E. & Wanner, G. 1991 *Solving Ordinary Differential Equations II: Stiff and Differential-Algebraic Problems*. Berlin: Springer-Verlag.

[24] Hof, B. 2005 Transition to turbulence in pipe flow. In *Proc. IUTAM Symp. on Laminar-Turbulent Transition and Finite Amplitude Solutions.* (ed. T. Mullin & R. R. Kerswell), pp. 221–231. Springer.

[25] Hof, B., van Doorne, C. W. H., Westerweel, J. & Nieuwstadt, F. T. M. 2005 Turbulence regeneration in pipe flow at moderate Reynolds numbers. *Phys. Rev. Lett.* **95(21)**, 214502–4.

[26] Hof, B., van Doorne, C. W. H., Westerweel, J., Nieuwstadt, F. T. M., Faisst, H., Eckhardt, B., Wedin, H., Kerswell, R. R. & Waleffe, F. 2004 Experimental observation of nonlinear travelling waves in turbulent pipe flow. *Science* **305**, 1594.

[27] Hof, B., Juel, A. & Mullin, T. 2003 Scaling of the turbulence transition threshold in a pipe. *Phys. Rev. Lett.* **91(24)**, 244502.

[28] Hof, B., Schneider, T. M., Westerweel, J. & Eckhardt, B. 2006 Finite lifetime of turbulence in shear flows. *NATURE* **443(7107)**, 59–62.

[29] Iserles, A. 1996 *A First Course in the Numerical Analysis of Differential Equations*. Cambridge: Cambridge University Press.

[30] Kawahara, G. & Kida, S. 2001 Periodic motion embedded in plane Couette turbulence: regeneration cycle and burst. *J. Fluid Mech.* **449**, 291–300.

[31] Kerswell, R. R. & Tutty, O. R. 2007 Recurrence of travelling waves in transitional pipe flow. *J. Fluid Mech.* **584**, 69–102.

[32] Komminaho, J. 2000 Direct numerical simulation of turbulent flow in plane and cylindrical geometries. PhD thesis, Royal Institute of Technology, Stockholm.

[33] Landahl, M. T. 1980 A note on an algebraic instability of inviscid parallel shear flows. *J. Fluid Mech.* **98**, 243–251.

[34] Leonard, A. & Reynolds, W. 1988 *Turbulent Research by Numerical Simulation, in: D. Coles (Ed.), Perspectives in Fluid Mechanics*. New York: Springer-Verlag.

[35] Leonard, A. & Wray, A. 1982 A new numerical method for the simulation of three–dimensional flow in a pipe. pp. 113–142. Springer-Verlag.

[36] Mamun, C. K. & Tuckerman, L. S. 1995 Asymmetry and Hopf bifurcation in spherical Couette flow. *Phys. Fluids* **7(1)**, 80–91.

[37] Mellibovsky, F. & Meseguer, A. 2005 Global finite amplitude perturbations in medium aspect ratio pipe flow. *J. Phys. Conf. Ser.* **14**, 192–205.

[38] Mellibovsky, F. & Meseguer, A. 2006 The role of streamwise perturbations in pipe flow transition. *Phys. Fluids* **18(7)**, 074104.

[39] Mellibovsky, F. & Meseguer, A. 2007 Pipe flow transition threshold following localized impulsive perturbations. *Phys. Fluids* **19(4)**, 044102.

[40] Meseguer, A. 2003 Streak breakdown instability in pipe Poiseuille flow. *Phys. Fluids* **15(5)**, 1203–1213.

[41] Meseguer, A., Avila, M., Mellibovsky, F. & Marques, P. 2007 Solenoidal spectral formulations for the computation of secondary flows in cylindrical and annular geometries. *Eur. Phys. J. Special Topics* **146**, 249–259.

[42] Meseguer, A. & Mellibovsky, F. 2007 On a solenoidal Fourier-Chebyshev spectral method for stability analysis of the Hagen-Poiseuille flow. *Appl. Num. Math.* **57**, 920–938.

[43] Meseguer, A. & Trefethen, L. N. 2000 A spectral Petrov-Galerkin formulation for pipe flow i: linear stability and transient growth. *Tech. Rep.* 00/18. Oxford University Comp. Lab.

[44] Meseguer, A. & Trefethen, L. N. 2001 A spectral Petrov-Galerkin formulation for pipe flow ii: nonlinear transitional stages. *Tech. Rep.* 01/19. Oxford University Comp. Lab.

[45] Meseguer, A. & Trefethen, L. N. 2003 Linearized pipe flow to Reynolds number 10^7. *J. Comput. Phys.* **186**, 178–197.

[46] Mhuiris, N. M. G. 1986 Calculations of the stability of some axisymmetric flows proposed as a model of vortex breakdown. *Appl. Num. Math.* **2**, 273–290.

[47] Nagata, M. 1990 Three-dimensional finite-amplitude solutions in plane Couette flow: bifurcation from infinity. *J. Fluid Mech.* **217**, 519–527.

[48] Nusse, H. E. & Yorke, J. A. 1989 A procedure for finding numerical trajectories on chaotic saddles. *Phys. D* **36**, 137–156.

[49] Nusse, H. E. & Yorke, J. A. 1996 Wada basin boundaries and basin cells. *Phys. D* **90**, 242–261.

[50] O'Sullivan, P. L. & Breuer, K. S. 1994 Transient growth in circular pipe flow. i. linear disturbances. *Phys. Fluids* **6(11)**, 3643–3651.

[51] O'Sullivan, P. L. & Breuer, K. S. 1994 Transient growth in circular pipe flow. ii. nonlinear development. *Phys. Fluids* **6(11)**, 3652–3664.

[52] Patera, A. T. & Orszag, S. A. 1981 Finite amplitude stability of axysimmetric pipe flow. *J. Fluid Mech.* **112**, 467–474.

[53] Peixinho, J. & Mullin, T. 2006 Decay of turbulence in pipe flow. *Phys. Rev. Lett.* **96(9)**, 094501.

[54] Pfenniger, W. 1961 *Boundary Layer and Flow Control*, chap. Transition in the inlet length of tubes at high Reynolds numbers, pp. 970–980. Pergamon.

[55] Pringle, C. C. T. & Kerswell, R. R. 2007 Asymmetric, helical, and mirror-symmetric traveling waves in pipe flow. *Phys. Rev. Lett.* **99(7)**, 074502.

[56] Priymak, V. & Miyazaki, T. 1998 Accurate navier-stokes investigation of transitional and turbulent flows in a circular pipe. *J. Comput. Phys.* **142**, 370–411.

[57] Reddy, S. C., Schmid, P. J., Bagget, J. S. & Henningson, D. S. 1998 On stability of streamwise streaks and transition thresholds in plane channel flows. *J. Fluid Mech.* **365**, 269–303.

[58] Reynolds, O. 1883 An experimental investigation of the circumstances which determine whether the motion of water shall be direct or sinuous, and of the law of resistance in parallel channels. *Phil. Trans. Roy. Soc. Lond. A* **174**, 935–982.

[59] Romanov, V. A. 1973 Stability of plane-parallel Couette flow. *Funct. Anal. Appl.* **7**, 137–146.

[60] Schlichting, H. 1968 *Boundary-Layer Theory*. New York: McGraw-Hill.

[61] Schmid, P. J. & Henningson, D. S. 1994 On the role of linear mechanisms in transition to turbulence. *Phys. Fluids* **6**, 1396–1398.

[62] Schmid, P. J. & Henningson, D. S. 1994 Optimal energy growth in Hagen-Poiseuille flow. *J. Fluid Mech.* **277**, 197–225.

[63] Schmid, P. J. & Henningson, D. S. 2001 *Stability and Transition in Shear Flows*. New York: Springer-Verlag.

[64] Schmiegel, A. 1999 Transition to turbulence in linearly stable shear flows. PhD thesis, Philipps-Universitt Marburg.

[65] Schmiegel, A. & Eckhardt, B. 1997 Fractal stability border in plane Couette flow. *Phys. Rev. Lett.* **79**, 5250–5253.

[66] Schneider, T. M., Eckhardt, B. & Yorke, J. A. 2007 Turbulence transition and edge of chaos in pipe flow. *Phys. Rev. Lett.* **99(3)**, 034502.

[67] Shan, H., Ma, B., Zhang, Z. & Nieuwstadt, F. T. M. 1999 On the spatial evolution of a wall-imposed periodic disturbance in pipe poiseuille flow ar re = 3000. part 1. subcritical disturbance. *J. Fluid Mech.* **398**, 181–224.

[68] Skufca, J. D., Yorke, J. A. & Eckhardt, B. 2006 Edge of chaos in a parallel shear flow. *Phys. Rev. Lett.* **96(17)**, 174101.

[69] Sweet, D., Nusse, H. E. & Yorke, J. A. 2000 Stagger-and-step method: detecting and computing chaotic saddles in higher dimensions. *Phys. Rev. Lett.* **86(11)**, 2261–2264.

[70] Trefethen, L. N. 2000 *Spectral Methods in Matlab*. SIAM.

[71] Trefethen, L. N., Chapman, S. J., Henningson, D. S., Meseguer, A., Mullin, T. & Nieuwstadt, F. T. M. 2000 Threshold amplitudes for transition to turbulence in a pipe. *Tech. Rep.* 00/17. Oxford University Comp. Lab.

[72] Viswanath, D. 2007 Recurrent motions within plane Couette turbulence. *J. Fluid Mech.* **580**, 339–358.

[73] Waleffe, F. 1997 On a self-sustaining process in shear flows. *Phys. Fluids* **9(04)**, 883–900.

[74] Waleffe, F. 1998 Three-dimensional coherent states in plane shear flows. *Phys. Rev. Lett.* **81(19)**, 4140–4143.

[75] Waleffe, F. 2001 Exact coherent structures in channel flow. *J. Fluid Mech.* **435**, 93–102.

[76] Waleffe, F. 2003 Homotopy of exact coherent structures in plane shear flows. *Phys. Fluids* **15(06)**, 1517–1526.

[77] Wang, J., Gibson, J. & Waleffe, F. 2007 Lower branch coherent states in shear flows: transition and control. *Phys. Rev. Lett.* **98(20)**, 204501.

[78] Wedin, H. & Kerswell, R. R. 2004 Exact coherent structures in pipe flow: travelling wave solutions. *J. Fluid Mech.* **508**, 333–371.

[79] Willis, A. P. & Kerswell, R. R. 2007 Critical behavior in the relaminarization of localized turbulence in pipe flow. *Phys. Rev. Lett.* **98(1)**, 014501.

[80] Wygnanski, I. J. & Champagne, F. H. 1973 On transition in a pipe. part 1. the origin of puffs and slugs and the flow in a turbulent slug. *J. Fluid Mech.* **59**, 281–335.

[81] Zikanov, O. Y. 1996 On the instability of pipe Poiseuille flow. *Phys. Fluids* **8(11)**, 2923–2932.